Title
Study of Nano-scale Non-equilibrium Thermal Transport Using Far-field and Near-field Ultrafast Optical Microscopy

Author
Su, Zhengliang

Publication Date
2021

Peer reviewed|Thesis/dissertation

Study of Nano-scale Non-equilibrium Thermal Transport Using Far-field and Near-field Ultrafast Optical Microscopy

By

Zhengliang Su

A dissertation submitted in partial satisfaction of the

requirements for the degree of

Doctor of Philosophy

in

Engineering - Mechanical Engineering

in the

Graduate Division

of the

University of California, Berkeley

Committee in charge:

Professor Costas P. Grigoropoulos, Chair
Professor Liwei Lin
Professor Junqiao Wu

Fall 2021

Study of Nano-scale Non-equilibrium Thermal Transport
Using Far-field and Near-field Ultrafast Optical Microscopy

Abstract

Study of Nano-scale Non-equilibrium Thermal Transport
Using Far-field and Near-field Optical Microscopy

by

Zhengliang Su

Doctor of Philosophy in Mechanical Engineering

University of California, Berkeley

Professor Costas P. Grigoropoulos, Chair

As modern technology advances keep pushing the size limit of electronic devices down to nanoscale, the densities of elementary units on integrated circuits (ICs) are drastically increased. One of the major deleterious effects is the huge density of heat generated that may lead to device malfunction or break-down. Therefore, nanoscale thermal management has become an important research topic, which requires progress in both fundamental understanding of nanoscale thermal physics on the material level and novel engineering strategies on the device end. On the other hand, recent advances in material synthesis, processing, and nanofabrication have made available rich families of new materials with unprecedented properties that elevate them to potential candidates for next-generation electronic devices. Characterizing such materials with structure that varies on the length scale of a few nanometers, such as nanowires, 2D materials and Van de Waals heterostructures, necessitates new methodologies and experimental strategies that can unveil unexplored thermal physics mechanisms.

In this thesis, we describe our recent work on developing a novel and comprehensive optical diagnostic platform with ultra-high sensitivity to conduct thermal measurements for a wild range of nanomaterials and nanostructures. Specifically, femto-second laser based optical pump-probe scheme is utilized to enable ultra-high temporal resolution (~300 fs), which offers access to investigating ultrafast dynamic processes that fundamental thermal carriers undergo in extreme non-equilibrium circumstances. Based on the ultra-fast optical pump-probe microscopy technique, we have extended the time-domain thermo-reflectance (TDTR) technique to frequency domain and constructed the time-resolved frequency domain thermo-reflectance (Tr-FDTR) measurement to characterize the transient material thermal properties across different time scales, from 100 fs to 10 ns upon ultrafast thermal excitation. Unlike TDTR, this newly developed methodology takes full advantage of the ultra-high time resolution embedded in ultra-fast pump-probe technique, for measuring dynamic thermal transport processes. Next, we have integrated the developed ultra-fast optical pump-probe microscopy technique with an atomic force microscopy (AFM) instrument in the configuration of scattering near-field scanning optical microscopy (s-

NSOM). The combination of ultra-high temporal resolution and ultra-high spatial resolution (~10 nm) makes this comprehensive optical diagnostics platform an unprecedented tool for studying nanoscale transient heat transfer and energy transport processes. With this powerful tool, we have successfully demonstrated the ability to capture the two-dimensional 'snapshots' of the ultra-fast photoexcitation process in silicon nanowires, and the ability to extract the near-field signals for studying material dynamics at a level that is not achievable with any of the current far-field techniques.

The developed instrumentation has the potential to contribute a new technology for investigating ultra-fast nanoscale thermal transport phenomena in both equilibrium and non-equilibrium regimes, which are currently completely unattainable with conventional thermal measurement techniques. The first major contribution will be the ability to directly investigate the ultrafast non-equilibrium thermal transport processes that various material systems undergo in response to an abrupt release of thermal energy. Key to the success of this effort is to utilize the femto-second time resolution to characterize the different behaviors of thermal energy carriers (electrons and phonons) and their interactions across all the stages (from sub-picosecond to nanosecond time range). This technique will enable us to experimentally verify new thermal transport mechanisms that emerge in unconventional material systems. The second major contribution is that the developed ultrafast thermal measurement technique can be extended down to nanoscale, thus offering the opportunity to interrogate fundamental nanoscale heat transfer problems. Therefore, we anticipate with confidence that this work will not only push the boundaries of our understandings of the nanoscale heat transfer and energy transport, but also shed light on unconventional mechanisms of thermal transport in newly discovered material systems that may be potential candidates for the next-generation electronics, and suggest new strategies for engineering nanomaterials for nanoscale thermal management in the next-generation electronics.

To my family.

Acknowledgments

I am deeply indebted to many people without whom I would never have finished this journey. First of all, I would like to express my sincere gratitude to my research advisor, Professor Costas P. Grigoropoulos in the Department of Mechanical Engineering at UC Berkeley, for his helpful guidance, insightful advice, and unconditional support. This 5.5-year-long journey is not a smooth sailing for me, and I sincerely thank him for his trust, patience, and encouragement during all the hard times of my stay in the Laser Thermal Laboratory. He has given me significant freedom in exploring the research topics that I am interested and willing to devote myself in, despite lots of trials and errors, and he has always kept an open mind for new ideas and topics which may be more or less out of his domain knowledge. He has also provided full support for me to achieve my research goals, both intellectually and financially. His enthusiasm for research challenges was, is and will be a treasure that I will cherish and learn from for the rest of my life. I also would like to express my gratitude to Professor Junqiao Wu in the Department of Materials Science and Engineering at UC Berkeley, Professor Liwei Lin and Professor Chris Dames in the Department of Mechanical Engineering at UC Berkeley for valuable advice on my research and being my qualifying exam committee in their busy schedule. I would also like to thank Professor Adam Moule in the Department of Chemical Engineering at UC Davis and Professor Alberto Salleo in the Department of Materials Science and Engineering at Stanford University.

Along my journey, I have had the honor to work with many extraordinary colleagues. I would like to acknowledge the help of my teammates in the Laser Thermal Lab. Dr. Yoonsoo Rho, who joined the PhD program at the same time as me, has accompanied me all the way here and offered lots of help and support for me. We have collaborated in several projects, and especially in the project that constitutes this entire thesis. Without his help, I could not have made this happen. Dr. Letian Wang, who was from the same college as me, has provided me significant support in both research work and daily life and given me helpful advice in every aspect. Dr. Meng Shi, who was my onboard buddy, has encouraged and supported me during my initial hard time here and continued to care about my mental health. I would also extend my gratitude to my other collaborators and lab-mates, Dr. Dongfeng Qi and Dr. Jiangyou Long from the Laser Thermal Lab, Dr. Zaira Bedolla and Dr. Goktug Gonel from Prefessor Moule's group, Dr. Camila Centra from Professor Salleo's group, Dr. Lei Jin, Dr. Yang Gao, Dr. Penghong Ci, and Dr. Sarah Warkanda from Professor Wu's group.

My family has always been supportive for me. I am extremely grateful to my parents for their love. I would like to sincerely thank my friend, Jau-Yuan Eric Chen, who has always been with me through all the ups and downs in life. I also want to express my gratitude to my friends, Chloe Leung, Jamie Lo, and Cindy Wang. Lastly, I want to give special thanks to my dog Ponzu, who has also been a good companion and brought so much joy to my life. Thank you all again!

Table of contents

List of Figures

List of tables

List of Equations

This page is left black intentionally.

1 Introduction

In this research work, we present our recent progress on developing a comprehensive and innovative experimental platform with both ultra-high temporal and ultra-high spatial resolution to study ultra-fast thermal physics and transport phenomena in nanoscale material systems. In this chapter, we will start with the background and motivation behind this study, and examine some relevant recent advances in both theoretical and experimental areas. In the end, we provide an overview of the structure of this thesis.

1.1 Research Background

The electronics industry has experienced a burgeoning development over the last several decades. Riding dazzling technological advances and driven by ever-growing market demands, the empirical trend of the continuously increasing density of transistors on the integrated circuits, indicated by Moore's Law, which states that the individual device components get smaller every year, is still pushing the size limit of a transistor down to several nanometers (Figure 1.1A). Device engineers have been astonishingly clever at maintaining Moore's Law. As of 2019, the '5 nm' semiconductor manufacturing process, as the newest MOSFET technology node, has already been put into mass production, and the '3 nm' process has also been used in commercial production. Accordingly, the number of transistor units on one single integrated circuit chip is approaching 50 billion. A semiconductor industry review organization, IMEC, aggressively predicts that the '2nm' process, based on various new field-effect transistor (FET) architecture designs and fabrication technologies, will be fully realized in the near future (Figure 1.1B).[1,2]

As an unavoidable consequence, one of the major overarching problems of electronics industry today is the nanoscale thermal management of densely packed devices that must release very high heat fluxes. Failure to control the thermal transport in the nanoscale can lead to permanent material damage, high-power electronics breakdown, and malfunction in opto-electronics as well as energy conversion and storage systems, including solar cells and batteries. In particular, effective thermal management often plays a determining role in the performance and reliability of high-power electronic and optoelectronic devices. However, traditional thermal engineering methodologies often fail to provide effective solutions to address these detrimental issues, since as the material system shrinks in size all the way to the nanoscale regime, the material thermal properties may be drastically altered and therefore they do not follow the same behavior patterns in macroscopic heat transfer. The relentless decrease in the size of devices and structures, the increase in their operating speeds and frequencies (gigahertz to terahertz) of the integrated circuits (ICs), and the ever more aggressive thermal conditions imposed upon them, have brought up an urgent need for sophisticated understanding and control of thermal transport at the nanoscale.[5 – 7]

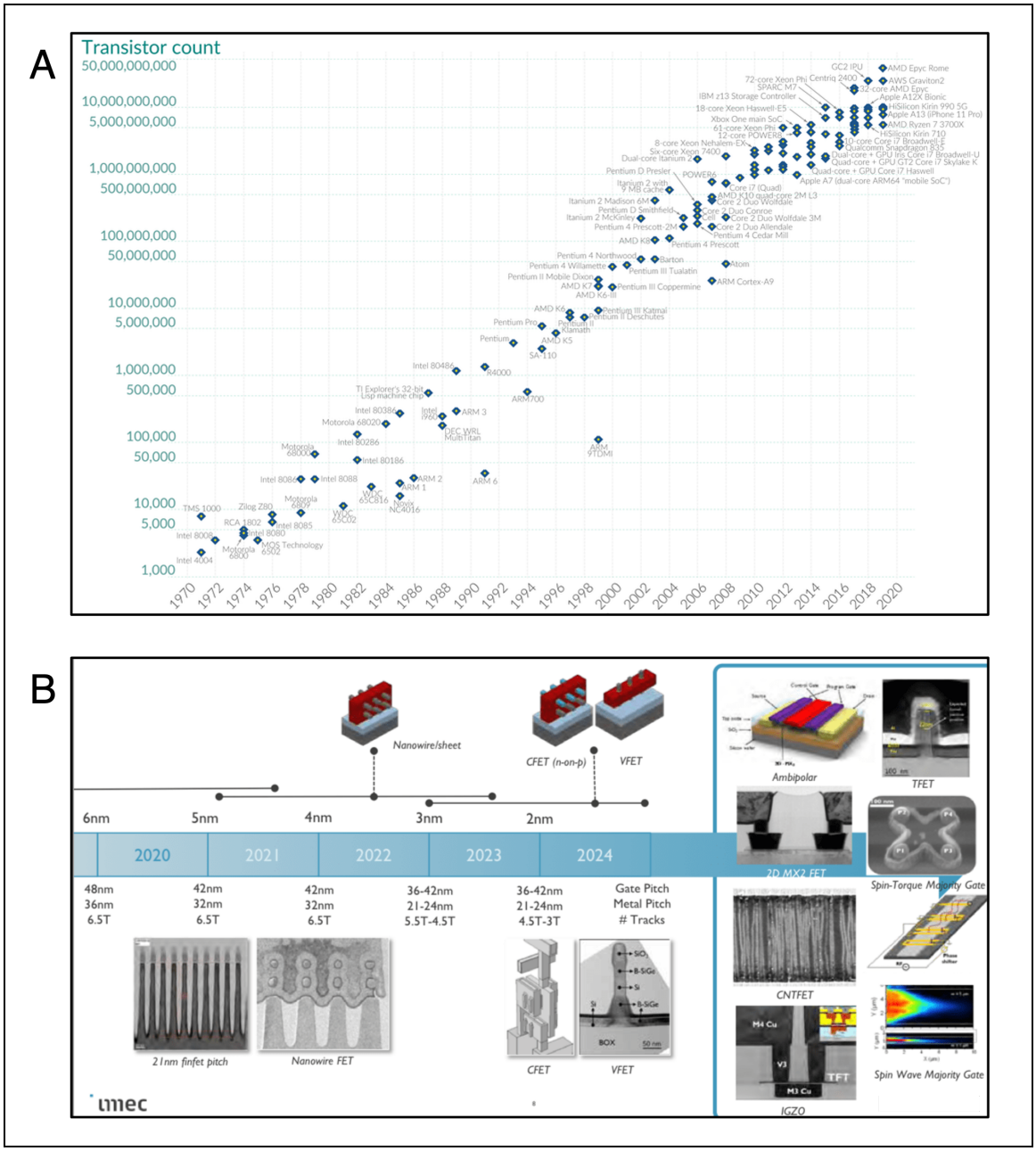

Figure 1.1 (A) Moore's Law describe the empirical regularity that the number of transistors on microchips doubles approximately every two years.[3] (B) IMEC view of the roadmap for transistor predicts that the 2 nm process will be realized in the near future.[4]

Meanwhile, because of recent rapid advances in nanoscience and nanotechnology, the last two decades have witnessed an era of discovery of various new materials that present novel properties and unprecedented opportunities for ground-breaking science and technology achievements, for example, high-temperature superconductors (twisted bi-layer graphene, cuprates), and high-electron-conductivity semiconductors (monolayer Molybdenum disulfide). Advanced experimental technologies in synthesis, processing, and

microanalysis are enabling the routine production of well-characterized materials with structure that varies on the length scale of several nanometers. Examples are semiconductor quantum dots and superlattices, polymer nanocomposites, multilayer coatings, microelectronic and optoelectronic devices, and micro-electromechanical sensors (MEMS), as shown in Figure 1.2.[3] While these new nano-materials and nano-structures provide an ideal platform to investigate unexplored nanoscale thermal transport physics, the development in this area has been significantly hindered since measurement of physical properties of systems with a characteristic size on the order of nanometers is challenging and often requires new or improved experimental techniques. As the dimensions of a system shrink, fundamental energy carriers, including electrons, holes (in semiconductors), phonons, excitons, etc., encounter new restrictions and boundary conditions, and therefore demonstrate different behavior patterns dictated by their new dispersion relations. Besides, other factors that are neglectable in macroscopic systems tend to play more important roles. For example, the surface-to-volume ratio increases in inverse proportion with the characteristic length scale, and the role of material interfaces becomes increasingly important. As a result, the mechanical, electrical, and thermal characteristics of the nanoscale systems may all deviate from their bulk counterparts, requiring new theoretical models and frameworks to describe their behavior. Evaluating and using these models requires measurement of physical properties at the nanoscale, and in many cases properties as we understand them in bulk may not even be properly defined.[12] Therefore, in addition to the urgent need for guidance in nanoscale thermal management from the device industry described above, fundamental scientific research communities are also eagerly exploring new technologies and advanced experimental techniques that are able to characterize properties of various materials and structures, investigate novel physics and thus exploit nanoscale materials properties and system behaviors at the nanoscale.

Nanoscale material thermal properties and system thermal behaviors in particular play an important role in a wide variety of important technologies and engineering systems. In most current and envisioned applications of nanostructures, thermal management has been one of the major challenges during product development processes. Scientific research driven by these applications have diverged into two main directions.

One direction is to address the need to efficiently transport the gigantic amount of heat generated during operations of a large number of densely packed electronic units in some devices, such as central/graphic processing units (CPU/GPU) or semiconductor lasers. A common component in a thermal management system is a high thermal conductivity material that can effectively conduct heat from a small high-power device to a larger heat exchanger that then dissipates heat to a working fluid. As for this aspect, one intuitive strategy is targeting at searching for new materials with high thermal conductivity. Engineering materials with high thermal conductivity is hard because it is essential to avoid defects and impurities during synthesis, which otherwise would significantly degrade materials thermal conductivity and impede heat flow. Recently scientists have made plausible milestone achievements regarding this effort. In 2018, three different research groups, Kang et al.[13], Li et al.[14], and Tian et al.[15], have successfully demonstrated synthesis of high-quality boron arsenide (BA, as shown in Figure 1.3A) with a thermal conductivity around 1100 W/m·K, which is half that of diamond but remarkably more than double that

of conventional metals, which goes against long-time phenomenological predictions[18] and earlier theoretical calculation[19], and supports recently developed theoretical calculation[20, 21], as shown in Figure 1.3B. In 2019, Cai et al. reported that high-quality one-atom-thin hexagonal boron nitride (BN, as shown in Figure 1.3C) has a thermal conductivity (κ) of 751 W/m·K at room temperature, the second largest κ per unit weight among all semiconductors and insulators. The κ of atomically thin BN decreases with increased thickness.[22] In 2020, Chen et al. found that isotopically pure cubic boron nitride (cBN, as shown in Figure 1.3D) has an ultrahigh thermal conductivity around 1600 W/m·K, 75% that of diamond. Using only boron-11 or boron-10 allows the crystal vibrations that carry heat to move more efficiently through the material.[23] The ultrahigh thermal conductivity makes such materials promising candidates for the microelectronics thermal management, high-power electronics, and optoelectronics applications. Another strategy from a more engineering-style perspective is to enhance the thermal conductance of the interface between two distinct materials, by means of mechanically and/or chemically assisted surface modification, although these efforts have so far proved elusive regarding obtaining significant improvement of the interface thermal conductance.

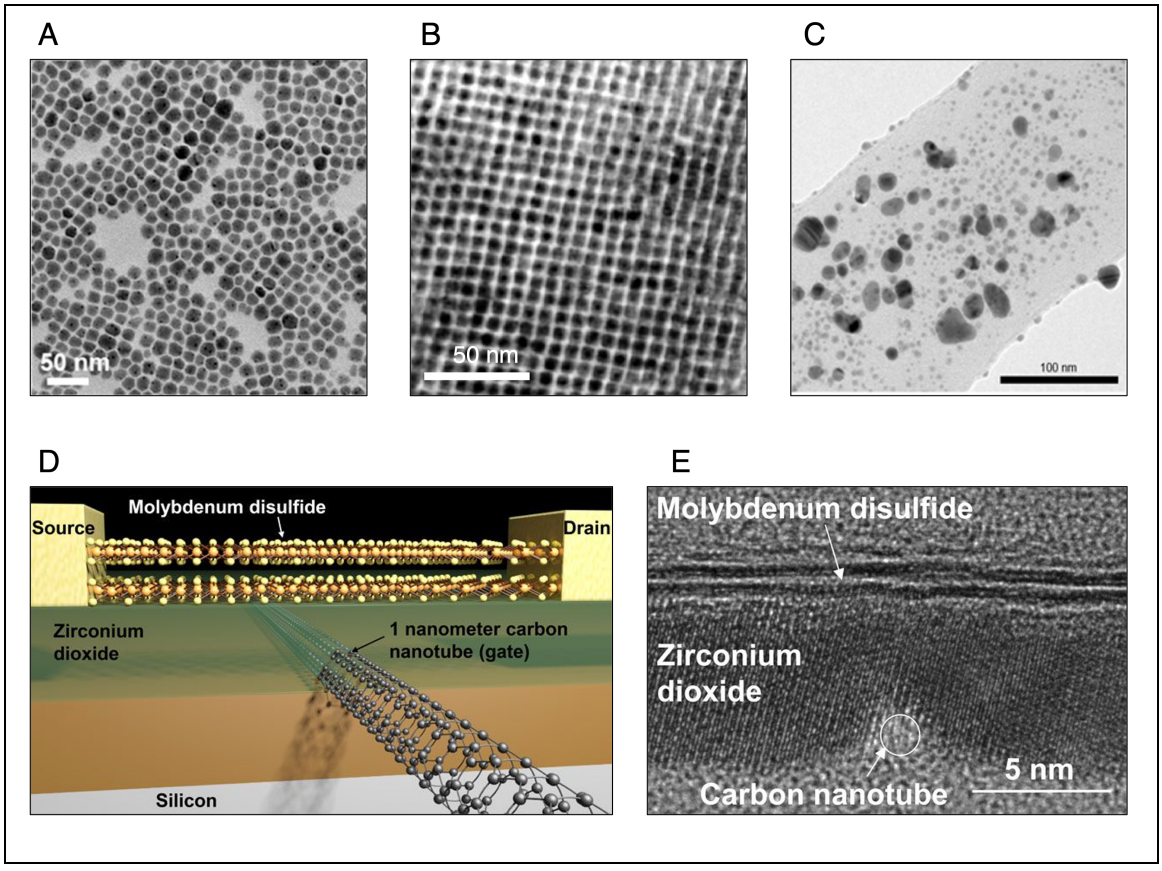

Figure 1.2 (A) TEM image of $CsPbI_3$ perovskite quantum dot.[8] (B) TEM micrograph of a 3D Iron nano-cube superlattice embedded in an epoxy resin.[9] (C) TEM image of silver-polymer nanocomposites.[10] (D) Schematics and (E) TEM image of a transistor using a two-dimensional material MoS_2 as channel material and 1-nm carbon nanotube as the gate.[11]

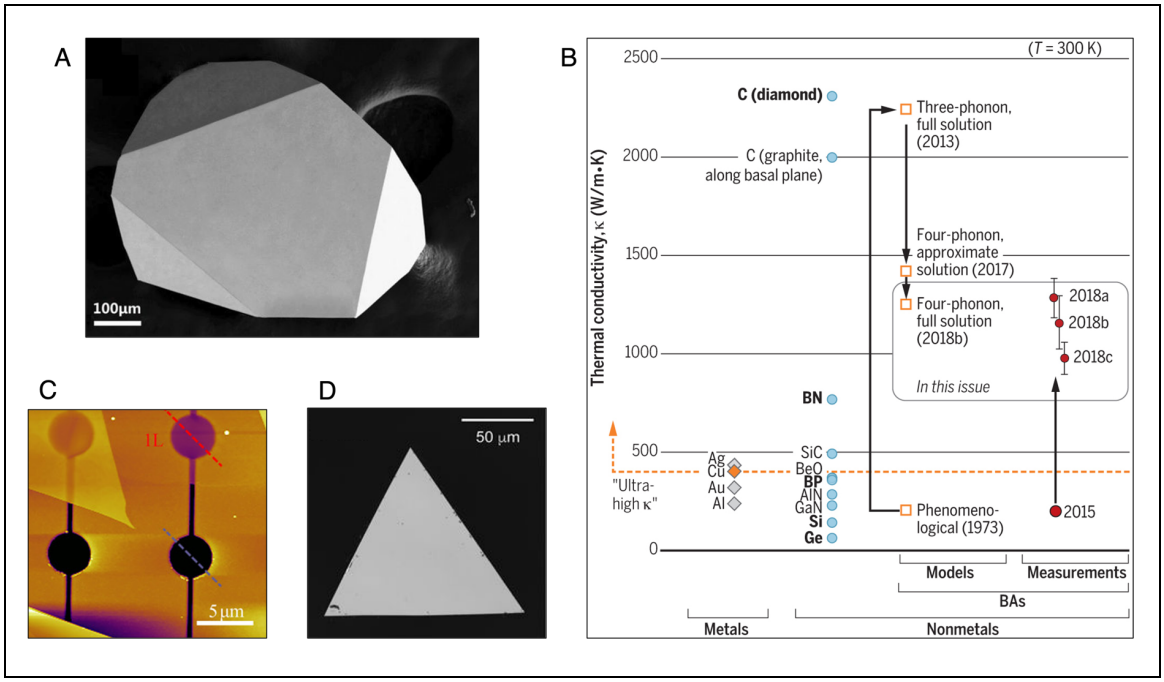

Figure 1.3 (A) SEM image of boron arsenide (BA) sample.[14] (B) Summary of high thermal conductivity materials, showing that high-quality crystals of boron arsenide (BAs) have a thermal conductivity about five times higher than traditionally expected.[16] (C) Optical image of a monolayer boron nitride (BN) sample on SiO_2/Si substrate with prefabricated microwells.[22] (D) Laser confocal scanning microscopy (LCSM) image of a c^{10}BN crystal surface.[23]

The other direction is to look for materials with thermal conductivity as small as possible, such as thermal barriers or thermoelectric materials used for solid-state refrigeration. Thermoelectric energy conversion – the direct conversion of thermal energy into electrical energy and vice versa, results from the fact that electrons (and holes in semiconductors) carry heat as well as charge. Therefore, electrons and holes group movement can be driven not only by an electrical potential, but also by a thermal potential (temperature). The performance of a thermoelectric device is quantified by the figure of merit (ZT), which is defined as:

Equation 1.1 thermoelectric figure of merit

$$ZT = S^2\sigma T/\kappa$$

Here S, σ, T, and κ denote the Seebeck coefficient, electrical conductivity, temperature, and thermal conductivity, respectively.[24] To improve the performance, it is better to reduce the thermal conductivity while the other terms in the figure of merit stay maintained. However, since electrons carry both charge and heat, the material electrical conductivity and the electronic contribution to the thermal conductivity are typically proportional to each other, governed by the so-called Wiedemann-Franz law:

Equation 1.2 Wiedemann-Franz law

$$\frac{\kappa}{\sigma} = LT$$

It states that the ratio of the electronic contribution of the thermal conductivity (κ) to the electrical conductivity (σ) of a metal is proportional to the temperature (T). The proportionality constant L, known as the Lorenz number, can be calculated as:

Equation 1.3 Lorenz number

$$L = \frac{\pi^2}{3}(\frac{k_B}{e})^2 = 2.44 \times 10^{-8}\, W \cdot \Omega \cdot K^{-2}$$

In 2017, Lee et al. reported a large violation of the Wiedemann-Franz law near the insulator-metal transition in vanadium dioxide (VO_2) nanobeams. In the metallic phase, the electronic contribution to thermal conductivity was much smaller than what would be expected from the Wiedemann-Franz law, which indicates the independent propagation of charge and heat in a strongly correlated system.[25] Such novel thermal property makes VO_2 a strong potential candidate for the next-generation thermoelectric material. Besides, Nano-structured materials can present a much lower thermal conductivity than predicted by traditional diffusion heat conduction theory, primarily due to a reduction in lattice thermal conductivity caused by reduced dimensions and material interfaces. As a result, nano-structured materials have exhibited improved thermoelectric performance.[26 – 28]

In a word, nanoscale thermal management has gained intensive attention from both research and industry communities in recent years, nanoscale thermal transport has developed into an interdisciplinary field that requires new fundamental understanding of nanoscale thermal physics, as well as novel engineering strategies.

1.2 Recent Progress in Nanoscale Thermal Transport and Probing

In the area of fundamental research on nanoscale thermal transport, there have been enabled both theoretical descriptions and experimental interrogations of new phenomena that emerge in the nanoscale. Thermal transport mechanisms that are different from conventional heat transfer pathways, universally intrinsic or driven by exotic nanoscale forces, have been experimentally demonstrated. Here two examples, near field radiative heat transfer and vacuum-induced phonon transfer, are selected to discuss below.

Several recent studies has shown that radiative thermal transport via fluctuating electromagnetic near-field in the form of evanescent waves between objects with nanoscale gaps that exceeds the far-field blackbody limit, corralled the attention of researchers and engineers due to its fundamental importance and its impact on a range of applications from data storage to thermal management and energy conversion.[29 – 33] Figure 1.4B shows the experimental results of the measured the heat transfer between two macroscopic sapphire plates as a function of separation over mm to μm and as a function of temperature differences between 2.5 and 30 K, which clearly indicates that the near-field radiation

allows heat to propagate across a small vacuum gap at rates several orders of magnitude above that of far-field, blackbody radiation, in agreement with expectations from theory.[29] Similar results are realized in various material systems in following pursuits, such as dielectric and metallic sample plates[30], semiconductor sample plates[31], and dielectric plates that support surface phonon polaritons[32, 33].

Another new heat transfer mechanism that has been discovered in the nanoscale is the so-called vacuum-induced phonon transfer, where quantum fluctuations of electromagnetic fields induce phonon coupling across vacuum and thereby facilitate heat transfer.[34, 35] Theoretical thermal physicists have sought for a long time the goal of unifying the three mechanisms of heat transfer, heat conduction, heat convection, and heat radiation. Among the topics relevant to this effort, a special interest is given to the regime in between heat conduction, which describes how the heat transfer in solids is conducted through either electrons or atomic vibrations known as phonons, and heat radiation, which determines how heat is transferred in vacuum by radiation. Recent theory has predicted that it is possible for phonon to transfer heat through vacuum without material medium, provided a certain phonon coupling mechanism between the solids separated by the vacuum, and in particular, Casimir force (a macroscopic effect resulting from quantum fluctuations of electromagnetic fields) induced phonon transfer can be very effective and even surpass the near field thermal radiation, given a good combination of the nature of the solid dielectric materials, the distance gap between them, as well as the operating temperature regime.[34] In 2019, experimental physicists successfully demonstrated that quantum fluctuations of electromagnetic fields could induce phonon coupling across a vacuum and thereby facilitate heat transfer in the natural transition from the radiative regime to the conductive regime of heat transfer between two identical isotropic nonmagnetic dielectric solid materials. As shown in Figure 1.4C, a nanomechanical system is used to realize strong phonon coupling through vacuum fluctuations, and the exchange of thermal energy between the two parallel plates is observed by monitoring the thermal Brownian motions of the individual phonon modes via laser interferometry independently. The experimental observation agrees well with theoretical calculations and is unambiguously distinguished from other effects such as near-field radiation and electrostatic interaction, since the phenomenon is observable at gap distance around hundreds of nanometers (300 – 500 nm), one order of magnitude larger than typical near field effect range, as shown in Figure 1.4D. This result reveals a new mechanism of heat transfer through a quantum vacuum. It also opens up new opportunities for studying quantum thermodynamics and energy transport using nanomechanical devices.[35]

These discoveries unveil previously unknown mechanisms of nanoscale radiative heat transfer, and inspire us to search for new exciting and intriguing phenomena of nanoscale heat conduction in solids, in hope for possible applications in nanoscale thermal management in modern devices. Such fundamental research and continued miniaturization of materials, components and systems have raised the need for the development of thermal-investigation methods enabling nanoscale measurements of surface temperature and thermo-physical properties in many areas of science and application fields.

The conventional temperature measurement is mostly based on the electrical or optical physical properties of materials. For example, the widely used temperature probing sensor, thermocouple, utilizes the Seebeck effect (described in Section 1.1) of thermoelectric materials to measure temperature based on the thermal equilibrium established at the mechanical contact point.[36] The infrared thermometer measures the emission of light at infrared wavelength to extract temperature based on the difference in emission from the sample at different temperatures. These methods have played important roles in thermal characterization, being capable of measuring temperature with high accuracy and resolution down to a few microns. However, as discussed in Section 1.1, the development of semiconductor industry, along with others including bio-technologies and medical research, requires spatial resolution as high as a few nanometers, these conventional methods would not be applicable due to either the dimension limit of the thermal probe or the diffraction limit of excitation source.[37] Sensitive probing of temperature variations on nanometer scales is an outstanding challenge in many areas of modern science and technology. In particular, a thermometer capable of sub-degree temperature resolution over a large range of temperatures as well as integration within various nanoscale systems could provide a powerful new tool in many areas of biological, physical and chemical research.[38] Potential applications include the study of heat dissipation in integrated circuits, the temperature-induced control of gene expression[39 - 42] and tumor metabolism[43], and the cell-selective treatment of disease[44, 45]. Over the past twenty years, extensive research efforts have been focused on the field of experimental technologies, and there has been tremendous advances that overcome the limitations of experimental pathways regarding nanoscale temperature measurement and thermal probing, seeking to achieve nanoscale spatial resolution and high-accuracy temperature measurement in various nano-systems, such as nano electronic devices and biomedical systems. A brief review on several methodologies in nanoscale surface imaging and temperature measurement is provided below.

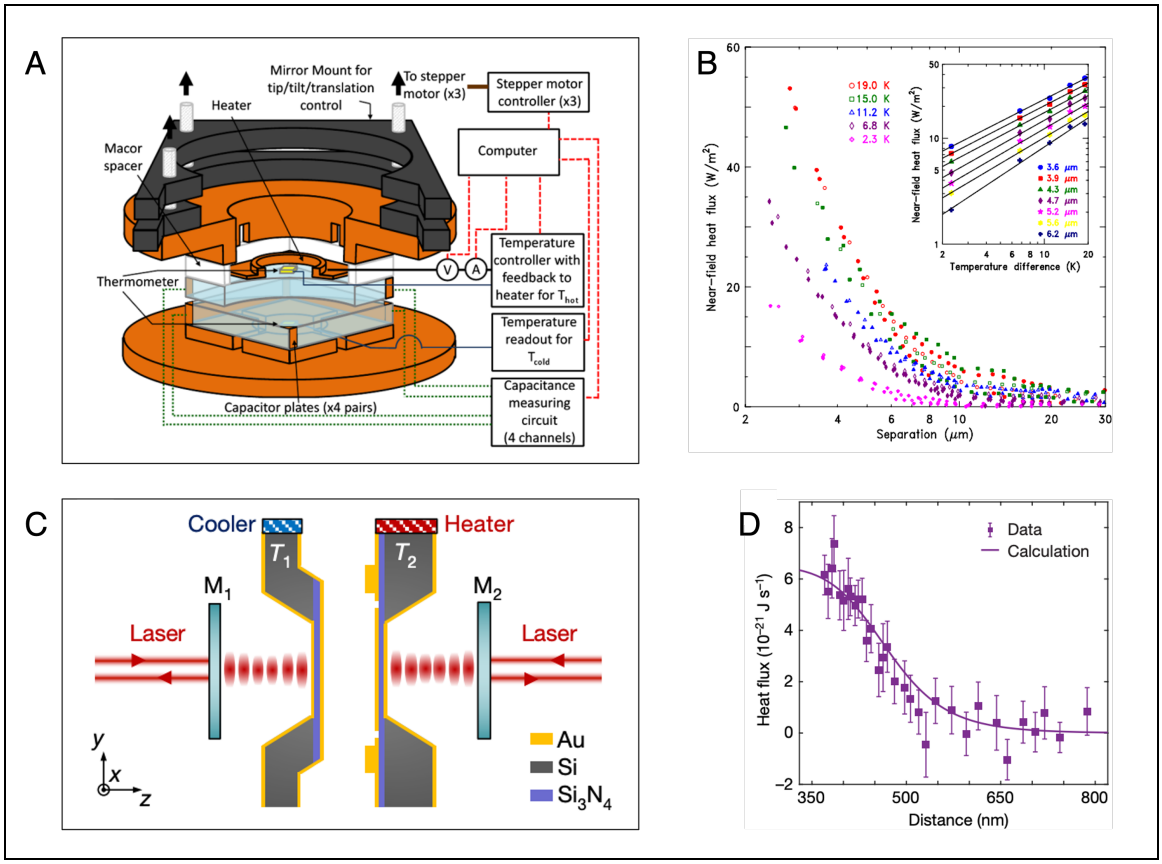

Figure 1.4 (A) A typical experimental apparatus for studying near field heat radiation. Stepper motors or piezo actuators are usually utilized to allow precise adjustment of the spacing, tip, and tilt of two sample plates. The temperatures of the plates are controlled independently by feedback circuits.[29] (B) Near-field heat flux vs distance for multiple temperature differences. The inset shows the near-field heat flux vs temperature difference for several specific separation distances.[29] (C) Cross-sectional view of the experimental setup, showing two nanomechanical Si_3N_4 membranes aligned in parallel and brought close together. Partially reflecting mirrors (M_1 and M_2) are placed behind the membranes, and laser beams (wavelength 633 nm) are sent from both sides to interferometrically measure the thermomechanical motion of the membranes. The distances between the mirrors and the membranes are feedback controlled by piezo actuators to maintain long-term stability of the interferometric detection sensitivity. The two samples are mounted on a closed-loop thermoelectric cooler and heater to stabilize the sample temperatures and tune the mechanical resonance frequencies. The setup is kept in a vacuum below 10^{-6} Torr.[35] (D) Heat flux transferred across the two thermal baths as a function of distance. The solid line represents the theoretical prediction of the coupled-mode model.[35]

The technical barrier to temperature measurement with nanoscale resolution can be overcome in different ways. One approach is to fabricate a nanoscale thermal probe or through a certain medium to achieve thermal probing down to the nanoscale. Scanning thermal microscopy (SThM) technique is one canonical example of this approach. SThM is based on atomic force microscopy (AFM) technique, with a nanometer-scale temperature probe attached or integrated onto the AFM tip.[46] Therefore, the spatial resolution of SThM is only limited by the physical size of the temperature probe. The temperature sensor integrated into a scanning probe tip can be either a thermocouple or a thermistor. Over the last decade, taking advantage of the development of microelectromechanical systems

(MEMS) and nanoelectromechanical systems (NEMS), fabricating temperature sensors with a-few-nanometer size has become readily feasible. Figure 1.5A illustrates the setup of an AFM-based SThM system, by attaching it to the tip of atomic force microscope or directly integrating it to the tip when fabricating the tip, the thermal probe is capable of doing nanoscale temperature imaging. Here, the output signal is the voltage delivered by a "thermal control unit" and a balanced Wheastone bridge can be used to maintain the probe mean temperature at constant value.[50] Figure 1.5B shows the SEM image (top) and the SThM image (bottom) of the self-heated interconnect. The interconnect structure is supplied with an AC voltage bias applied, which leads to enhanced Joule heating around the lithographically defined constrictions.[50] This clearly demonstrates the capacity of the SThM to image the non-uniform temperature field distribution in nanoscale systems, with ultra-high spatial resolution. Up to date, there have been significant improvements in its spatial resolution to ~10 nm, temperature precision to ~50 mK, and measurements of nanometer-scale heat flows to ~10 pW.[46 – 49] Besides using a temperature sensor in the cantilever tip, there are other alternatives such as measuring local thermomechanical strains in the sample or the cantilever, however, efforts along this path has been elusive since such mechanisms are in general more much complicated and are subject to various other factors, including material properties, sample geometries, and tip apex conditions.

Methodologies based on optical methods are also an important strategy for nanoscale temperature measurement, and has been broadly applied in research and industry field due to its non-contact and non-destructive probing features. Some techniques are based on the dependence of material optical properties on temperature, such as emissivity and reflectivity. The temperature can be measured by focusing the light to the target region and monitoring the change of the light reflectance. Several techniques have been developed based on this principle, including infrared thermography and thermo-reflectance method. Same as other far field techniques, the spatial resolution of these techniques is limited by the so-called Abbe diffraction limit, which is defined as:

Equation 1.4 Abbe diffraction limit

$$d = \frac{\lambda}{2n\,sin\theta} = \frac{\lambda}{2NA}$$

Where d, λ, n, θ, and NA denote the minimum resolvable distance (Abbe diffraction limit), the wavelength of the light, the refractive index of the medium, the convergence half-angle, and the numerical aperture of the objective lens, respectively. Considering green light around 500 nm and a NA of 0.5, the Abbe limit is roughly 500 nm. Therefore, it is difficult for these conventional optical probing methods to achieve a resolution down to a few nanometers.

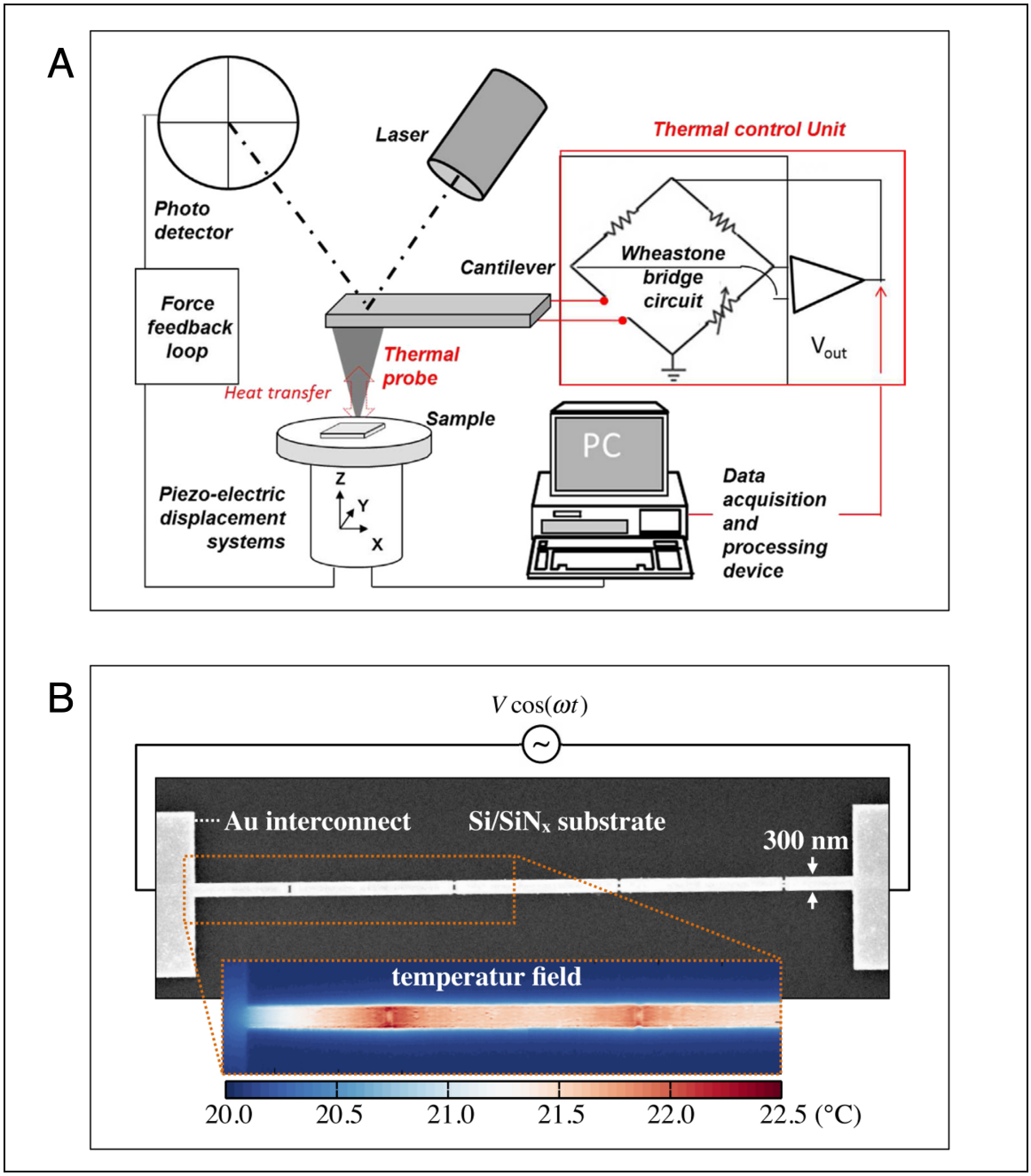

Figure 1.5 (A) The set-up of an AFM-based SThM system. Here, the output signal is the voltage delivered by a ‘‘thermal control unit’’ and a balanced Wheastone bridge can be used to maintain the probe mean temperature at constant value.[50] (B) Illustration of the self-heated interconnect. The top image shows an SEM image of the interconnect structure including a schematic of the electrical circuit applied. The AC voltage bias applied leads to enhanced Joule heating around the lithographically defined constrictions as illustrated in the bottom image with a temperature map obtained by scanning thermal microscopy.[50]

To bypass the physical constraint on the capacity of optical systems, researchers have developed innovative nanoscale temperature probing techniques, of which the most prominent strategy is to introduce well-calibrated “markers” or “indicators” into the target

system, such as special nanoparticles, quantum dots, or molecules, which have strongly-temperature-dependent properties that can be easily measured, such as fluorescence or Raman shift. Specifically, there are nanoscale optical thermal probing techniques which are based on the temperature dependence of electronic and lattice band structure of materials, for example, the fluorescence thermometry and Raman thermometry.[37] The temperature is evaluated by studying the spectrum of emitted photons from the material. Therefore, the resolution will not be limited by the diffraction limit, but by the size of these nanoscale "thermometers" under measurement. For example, in 2013, Kucsko et al. demonstrated a new approach to nanoscale thermometry that uses coherent manipulation of the electronic spin associated with nitrogen–vacancy color centers in diamond.[38] As shown in Figure 1.6A, one gold nanoparticle and a few nano-diamonds were introduced into a single cell, and the gold nanoparticle serves as the heat source (strongly absorbing optical energy and transforming into heat), and the individual nano-diamonds work as nanoscale thermometers. Figure 1.6B plots the measured localized temperature change as a function of the relative distance between the measured location and the heat source (the gold nanoparticle), all the data including the temperature changes and relative distances are measured in a laser confocal microscopy image (not shown here), and the result matches well with theoretical calculations based on heat conduction (blue line). Their technique successfully achieved to detect temperature variations as small as 1.8 mK (a sensitivity of 9 mK·Hz$^{-1/2}$) in an ultra-pure bulk diamond sample. With the nitrogen–vacancy center in diamond nanocrystals (nano-diamonds), the local thermal environment on length scales as short as 200 nanometers was directly measured. In addition, by introducing both nano-diamonds and gold nanoparticles into a single human embryonic fibroblast, they demonstrated temperature-gradient control and mapping at the subcellular level, enabling unique potential applications in life sciences.

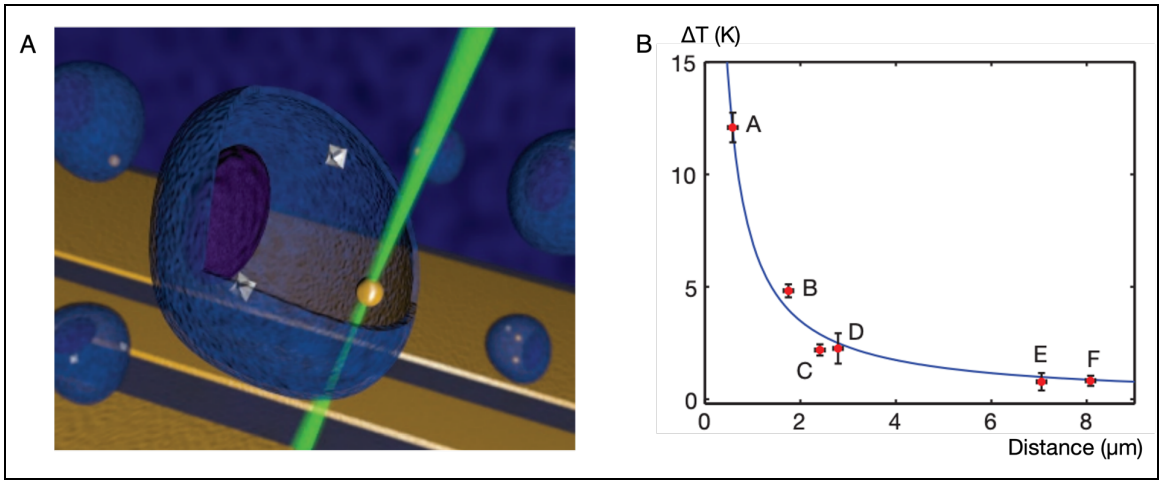

Figure 1.6 (A) Schematic image depicting nano-diamonds (grey diamonds) and a gold nanoparticle (yellow sphere) within a living cell (central blue object; others are similar) with coplanar waveguide (yellow stripes) in the background. The controlled application of local heat is achieved by laser illumination of the gold nanoparticle, and nanoscale thermometry is achieved by precision spectroscopy of the nitrogen–vacancy spins in the nano-diamonds.[38] (B) Temperature changes measured (red points) at the six nano-diamond locations as a function of distance from the illuminated gold nanoparticle (temperature changes and relative

distances are measured in a laser confocal microscopy image. The blue curve is the theoretical temperature profile based on a steady-state solution of the heat equation.[38]

Besides the nanoscale "indicator" method described above, another approach to go beyond the Abbe diffraction limit is to place the excitation source or detection probe close to the sample surface with a distance less than the wavelength, specifically, this will require utilizing the so-called scattering near-field scanning optical microscopy (s-NSOM), a microscopy technique for nanostructure investigation that breaks the far field resolution limit, that is, the Abbe diffraction limit, by exploiting the properties of evanescent electromagnetic waves. In the early stage of the development of SNOM, the excitation laser light is focused through an aperture, fabricated as a hollow tube throughout the AFM tip apex, with a diameter smaller than the excitation wavelength, which results in an evanescent field (or near-field) on the far side of the aperture. The aperture can be used to confine the light source to excite the surface. A high spatial resolution around several nanometers for surface imaging has been achieved by approaching the detector to the object with a very narrow aperture.[37] However, this configuration requires delicate fabrication of the special AFM tip, and also brings technical difficulty to collect optical signals. Today the majority of the modern NSOM operations are done in a tip-based apertureless mode: the excitation laser is directly focused onto the tip apex without going through the channel inside of the tip apex. In both modes, the key challenge for NSOM is to magnify the optical near field interaction with nanoscale local regions of the sample since near field signals are usually weak and hard to effectively collect, and distinguish the near field signal from the overwhelmingly dominant far field signals if the detection mechanism is not exclusively present in near field. To solve this problem, many NSOM applications take advantage of the fact that the near-field interaction has a strong inductive effect from the currents and charges in the antenna (the geometry to induce the near-field effect of the tip apex), which causes enhancement effect of the optical field. The enhanced optical near field existing in a region with only a few nanometers can be used for nanoscale structural imaging, material/chemical detection, and temperature probing. Using near-field temperature measurement, a response time shorter than 10 ms and high temperature resolution with 0.1 K can be achieved, depending on the signal-to-noise ratio of the optical signal.[50]

Using the tip of AFM to produce the near-field enhancement effect works very well in practice. Due to sharpness of the tip apex, the antenna effect can significantly enhance the near-field electromagnetic evanescent wave intensities. With the AFM original nanoscale topography imaging capacity, the NSOM mapping can be easily developed and integrated into the AFM system. Typically, an external laser is loosely focused onto the apex of the tip by an objective lens or parabolic mirror. With the sample engaged only a few nanometers beneath the tip apex, the enhanced near field in the gap between the tip apex and the sample surface can induce localized excitation on the sample. The enhanced optical field induced by the tip is a consequence of plasmon resonances, which can be used in surface imaging and thermal probing. An extremely high spatial resolution has been achieved at the level of 10 nm, and the resolution (size of optical field) depends on the geometry (size and convergence angle) of the tip.[52] The strong optical field leads to intensive near field light-matter interaction and then excites strong inelastic Raman signal and fluorescence, from which the localized temperature can be inferred by the Raman shift

or the fluorescence. In 2011, Yue et al. studied the temperature rise in a silicon substrate under near-field laser heating with the Raman thermometry.[53] As shown in Figure 1.7A, the AFM runs in contact mode (the tip is directly in contact with the sample surface), and an external continuous laser is used to irradiate the contact region between the tip and sample. A strong optical field appears at the apex of the tip and intensive heating was generated at the surface of the sample. The enhanced Raman signal from this region was captured for temperature inference from normal Raman measurement calibration. Based on the temperature dependence of Raman shift and peak analysis from Raman signal, the localized temperature was probed with a spatial resolution down to sub-10 nm.

To conclude, various techniques used in nanoscale temperature measurement are reviewed in this section, such as the scanning thermal microscope (SThM) method, optical feature size method, and near-field optical measurement. Among these techniques, the SThM technique has a wide range of applications such as materials characterization and micro/nanoscale manufacturing in both academic research and industrial fields, but its spatial resolution is limited by the size of the thermal probe. The feature size method provides a unique perspective, achieving the nanoscale temperature probing via the nanoscale thermal "indicators". This method has been widely employed in biology research. The major limitation of this method for more generalized applications lies on the nanofabrication of nano-scale temperature sensors (the "indicators") that are suitable for specific situations, as well as the precise control of measuring locations. The feature size method can achieve high impact when used with other advanced microscopy methods, such as SThM. The near-field optical method offers ultra-high resolution down to sub-10 nm, but relies heavily on the sample's optical properties, such as strong Raman or fluorescence signal. On one hand, the incident laser intensity should be sufficient to produce measurable signals. On the other hand, large laser intensities may cause unwanted heating in the near field, and cause severe perturbation in the local region under measurement. In practice, the trade-off between the two factors has to be carefully evaluated and verified. In summary, nanoscale temperature measurement is critical to the development of nanotechnologies, while the development of nanofabrication techniques could, in turn, significantly advances nanoscale temperature measurement to higher resolutions and accuracy.

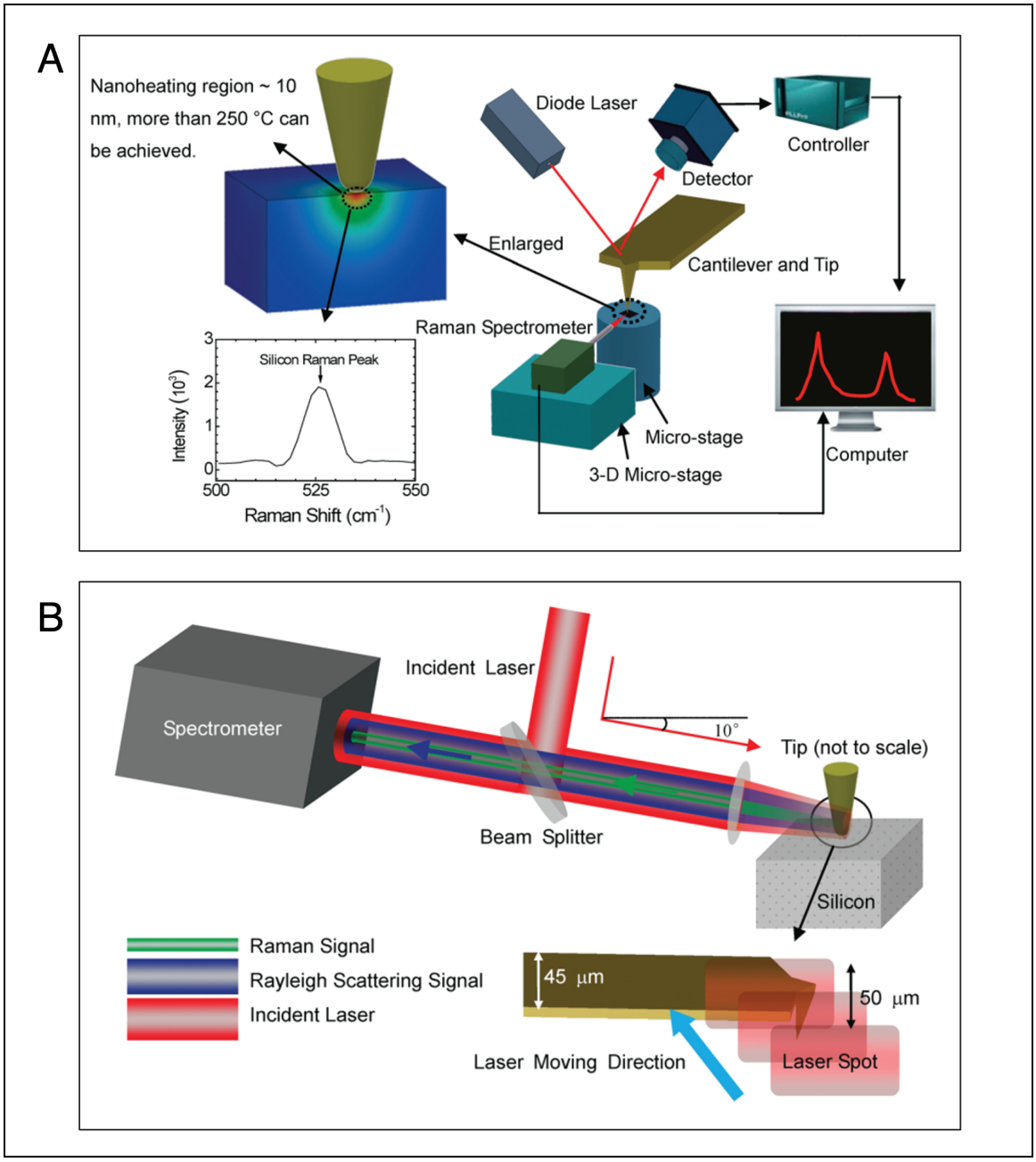

Figure 1.7 (A) (a) Schematic of experimental setup for the apertureless NSOM (not to scale) for thermal sensing. Control of the cantilever and tip is accomplished by monitoring the reflection of the diode laser irradiating the cantilever. A Raman spectrometer is placed in front of the AFM, and the positions of both the Raman spectrometer and the sample are adjusted by the micro-stages.[53] (b) Schematic of the optical system. The incident laser passes through a beam splitter and is focused on the tip by a convex lens. The excited Raman signal and Rayleigh scattering signal go along the same optical trace back to the spectrometer.[53]

1.3 Challenges in Experimental Study of Nanoscale Thermal Transport

One of the overarching challenges in the research area of nanoscale thermal transport is to experimentally understand the physical mechanisms that govern and dictate the nanoscale thermal transport phenomena that are distinct from their macroscopic counterparts, or the cause for events that do not even exist in macroscopic context. As the length scale of interest shrinks to nanoscale and becomes comparable or even smaller than the characteristic mean free paths of energy carriers, such as electrons and phonons, many anomalous thermal transport phenomena may take place. For example, in one-dimensional systems, such as carbon nanotubes or conducting polymer chains, interacting electrons is described by the Tomonaga–Luttinger liquid model, and the universal ratio of electrical to thermal conductance in a Fermi liquid, i.e., the Wiedemann-Franz law (Equation 1.2), is modified.[54] However, the experimental verifications are still not comprehensive since such a classification requires demanding nanoscale thermal probing techniques with ultra-high spatial resolution. On the other hand, recent developments in material synthesis, processing, and nano-device fabrication have made new materials accessible, which present unprecedented properties that justify them as potential candidates for next-generation electronic devices. However, large-scale production of single crystals of these materials is still challenging. For example, vanadium dioxide (VO_2) undergoes a metal–insulator transition coupled with a first-order structural phase transition around 340 K, which makes it promising for novel application in nano thermal regulators. This potential cannot be fully realized at the macroscale, as bulk VO_2 tends to rapidly develop cracks after a few cycles of the phase transition.[55] Therefore, characterizing such nanomaterials is not only of fundamental scientific importance, but also offers high impact in the engineering world.

Besides the spatial resolution limitation mentioned above, there are also many experimental challenges that nanoscale thermal measurement has to overcome. From the perspective of nanoscale thermal management, as the typical operating speed of the electronic units in integrated circuits is in the range from giga-Hertz to tera-Hertz, the fundamental thermal energy diffusion and dissipation are mostly in the transient regime that is far from equilibrium. From the perspective of fundamental thermal physics, as the length scale gets to that of the mean free path of thermal energy carriers, the transition from diffusive to ballistic transport starts to strongly influence the apparent thermal properties. In this non-equilibrium regime, the thermal behavior of carriers reveals much more information about their own characteristics than what steady-state measurement can offer. In the case of light-matter interaction, for example, considering photoexcitation in a small region of a metallic sample, such as aluminum, the conduction electron quasiparticles are excited to higher energy levels within 100 fs, and the localized excited electrons reach a high equivalent temperature (thousands of degrees). Those hot electrons diffuse and collide with other electrons and phonons, through electron-electron and electron-phonon interactions, with their excessive energies transferred to other elementary entropy carriers, in a time scale of 1 ~ 10 ps. These carriers diffuse further to other low-temperature region. If one or more dimension(s) of the sample geometry is in the nanoscale regime, the electron and phonon momentum-energy dispersion relations will be renormalized, which directly changes their dynamics and corresponding interactions. Thus, these nanoscale material systems have the potential to exhibit anomalous non-equilibrium thermal transport

behavior that may even manifest new transport mechanisms. Fundamentally, these microscopic elementary carrier dynamics and many-body interactions, including electron-photon, electron-electron, and electron-phonon interactions, dictate the material thermal properties and thermal transport. Therefore, measuring nonequilibrium thermal transport and characterizing transient material thermal properties is the key to deciphering the pathways through which microscopic interactions determine the thermal transport of materials.

As discussed in the previous two sections, driven by the continuous miniaturization of electronic devices and the urgent need to investigate physical, chemical, and biological phenomena at the nanoscale, nanoscience and nanotechnology have experienced the significant advances in the past two decades, which has empowered exciting development in innovative and advanced experimental techniques for nanoscale thermal transport study. However, those nanoscale measurement techniques are far from meeting this extreme expectation here: the appropriate technique for this purpose must demonstrate both ultra-high spatial resolutions to access the nanoscale regions of interest, and equally importantly, the ultra-high temporal resolution to capture events happening at a time scale of below or on the order of nanosecond. For example, the most promising techniques in this regard are scanning thermometric microscopy and NSOM-based thermometry methodology, but their current applications are limited to resolving the local temperature profile in nano-systems, and such measurements are all steady-state measurement, which can be utilized to measure systems in equilibrium or evolving with a much longer characteristic time scale compared with the temporal resolution of the nano-thermometry technique. Since the latter is usually limited by the lock-in detection time resolution, which typically ranges from 1millisecond to 1 second, it is not possible to study dynamic events that happen at shorter time scale, such as electron-electron interaction, electron-hole interaction and electron-phonon interaction. This setback greatly limits the applications of these advanced techniques, and inspires research communities to develop new experimental strategies to combine spatial and temporal resolutions.

1.4 Research Goals

In order to experimentally access the nonequilibrium regime of thermal transport in the nanoscale, this thesis describes an innovative solution for the overarching problem discussed above. Specifically, the ultra-fast optical pump-probe microscopy based on femto-second laser technology is introduced and integrated into the near-field scanning microscopy. Laser-based optical diagnostics techniques have many advantages over conventional thermal measurement methods that make them versatile tools in the research of nanoscale non-equilibrium thermal science. By the choice of the laser wavelength, pulse width, repetition rate, number of pulses and intensity, laser-based optical diagnostics provide precise regulations of heat transfer and energy transport in both temporal and spatial domains, enabling many thermal measurement configurations that address the on-demand need for studying various nanostructures, including thin metallic film, single crystalline nanowire/nanobeam, monolayer 2D material and Van de Waals heterostructures

of 2D materials. Furthermore, ultra-fast laser pulses from femto-second laser systems offer adequate capability to directly access the nonequilibrium regime (typically < 1 ns), and the ultra-short duration of the laser pulse (on the order of 100 fs) enables sufficiently high temporal resolution that makes the reconstruction of the time-course evolution of the nonequilibrium thermal processes feasible.

Therefore, this research work is targeted to develop a versatile laser-based methodology for measuring nanoscale nonequilibrium heat transfer and energy transport, characterizing time-dependent transient thermal properties of nanomaterials, and investigating new thermal physics that emerges in unconventional material systems. A list of detailed research goals has been provided below:

- Constructing a novel and comprehensive optical diagnostics platform to conduct time-resolved non-equilibrium thermal transport measurements, and to characterize transient material thermal properties across different time scales from 100 fs to 10 ns after thermal excitation.

- Demonstrating experimental capabilities to perform developed thermal measurements for a wide range of nanomaterials and nanostructures, with an emphasis on direct measurement of localized thermal properties with spatial resolution in the neighborhood of 10 nm.

- Developing a theoretical framework to qualitatively and quantitatively distinguish different microscopic degrees of freedom (electrons and phonons) and also shed light on their interactions in different material systems.

- Investigating new nanoscale thermal transport mechanisms in unconventional material systems and explore possible applications for nanoscale thermal management.

To address these challenges, this research has developed a flexible and versatile optical diagnostics platform of ultra-high sensitivity and reliability, which has encountered two major stages. The first stage is setting up the far-field optical instrumentation: a near-infrared femtosecond laser system is utilized to build up the ultrafast optical pump-probe microscopy: the laser beam is split into two branches, the major one being the ‘pump’ that serves as an ultra-fast heating source acting on the sample first, and the other minor one being the ‘probe’, whose transient reflectance off the sample surface or transmittance through the sample at a specified delay time interval is recorded. By varying the optical beam path length difference between the pump and the probe, a delay time sweep is performed, thereby reconstructing the temporal evolution of the ultrafast dynamics ensuing the pump excitation. The recorded change of probe signal represents the dynamic processes that the fundamental thermal carriers (electrons and phonons) undergo under extreme non-equilibrium circumstances. The transient response can be utilized to distinguish different microscopic degrees of freedom (electrons and phonons) and shed light on their interactions in different material systems. The second stage of the development is targeted at integrating the ultrafast optical pump-probe microscopy technique with near field scanning optical microscopy (NSOM), aimed to combine both ultra-high time resolution

(~100 fs) and beyond-diffraction-limit spatial resolution (~10 nm). The enhanced optical field underneath the scanning probe tip can directly access nanodomains, allowing direct measurement of localized thermal properties in inhomogeneous material systems.

Figure 1.8 summarizes a comparison of our developed work and other commonly used thermal measurement methods, showing that the technique developed in this work can readily access the typical range of microscopic thermophysical events, i.e., the lifetime and mean free path of thermal carriers. The developed methodology offers a comprehensive approach to study anomalous thermal properties and transport in unconventional material systems. The gained understanding of new thermal transport mechanisms can be further utilized to innovate new engineering approaches to manipulate the thermal transport in these materials and potential applications in nanoscale thermal management. These accomplishments will constitute a true breakthrough in the research field of nanoscale thermal transport for probing transient non-equilibrium nanoscale thermal transport at high spatial resolution.

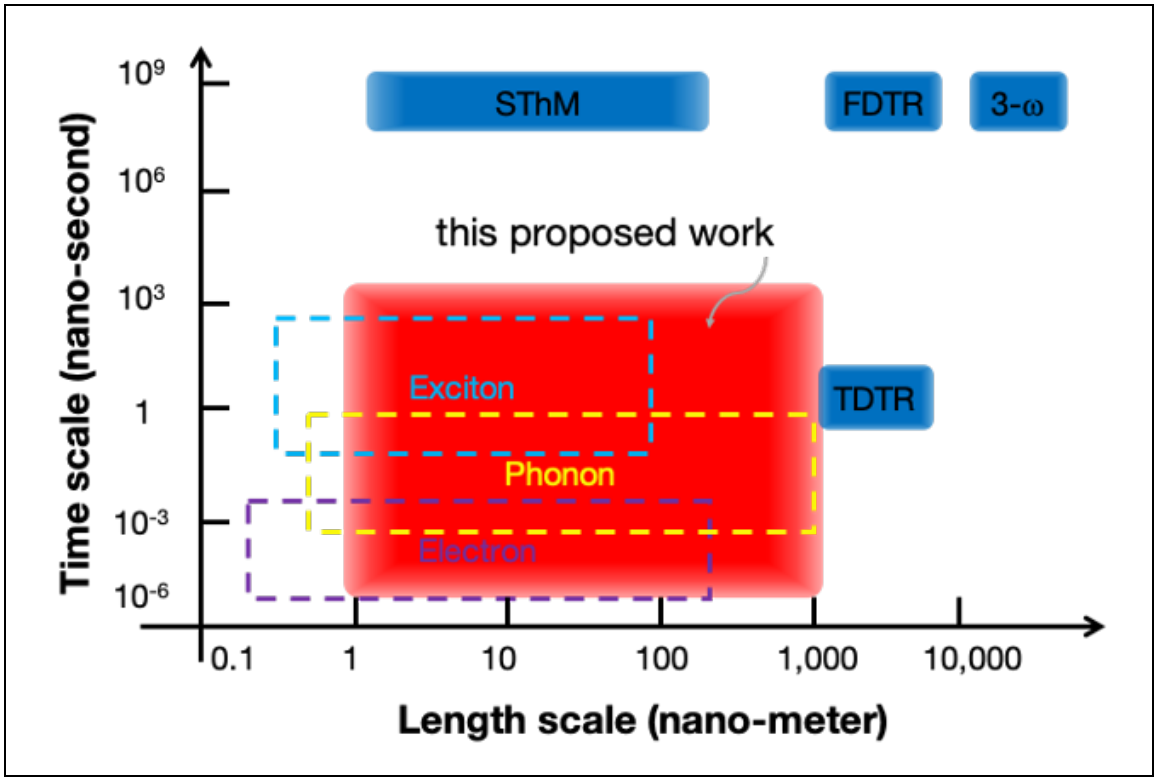

Figure 1.8 Summary of typical temporal and spatial scales in thermal physics and the capacity of common techniques used in thermal measurements. Notice that the capacity of this proposed work covers most of the regimes of interest, including the non-equilibrium regime of thermal transport, where elementary thermal carriers present their individual behaviors. This cannot be achieved by current methods, such as time-domain thermo-reflectance (TDTR), Frequency-domain thermo-reflectance (FDTR), 3-ω method (3-ω), and scanning thermo-microscopy (SThM). Detailed descriptions about these methods will be discussed in later chapters.

1.5 Structure of This Thesis

This thesis reports our recent progress on developing a powerful integrated experimental instrumentation based on ultra-fast optical pump-probe microscopy and near-field scanning optical microscopy, which offers both ultra-high temporal and ultra-high spatial resolution to study ultra-fast thermal physics and transport phenomena in nanoscale material systems. In Chapter 2, we focus on achieving the ultra-high temporal resolution: we will discuss the experimental configuration and theoretical framework to utilize far-field optical pump-probe microscopy for optical characterization of thermal properties of nanomaterials, specifically using time-domain thermo-reflectance (TDTR) to measure the thermal conductivity of the materials, and then extending it to frequency domain to characterize the transient thermal properties of the materials in the extreme non-equilibrium regime after the ultra-fast heating by the femtosecond laser pulses. In Chapter 3, we will discuss the experimental strategies to combine the ultra-high temporal and ultra-high spatial resolution by introducing an atomic force microscopy (AFM) instrument to the developed far-field experimental instrumentation, and we will demonstrate some highlights of the experimental achievements regarding the ultra-fast nanoscale thermal physics and transport phenomena. Chapter 4 will provide a summary of this research work, and furthermore provides some directions for future work to maximize the potential impact of our developed methodologies to facilitate research on related topics.

This page is left black intentionally.

2 Thermal Transport Study via Far-field Ultra-fast Optical Microscopy

This chapter discusses in detail the first stage of this research work, far-field ultra-fast optical microscopy instrumentation. This part of work not only has laid the experimental foundation for the second stage of the work, near-field ultra-fast optical microscopy, but also stands on its own as an independent platform for transient thermal transport study. Specifically, this instrument can be easily adapted to support a wide range of experimental schemes, including optical reflection/transmission-based ultra-fast pump-probe microscopy/spectroscopy and time/frequency-domain thermo-reflectance (TDTR/FDTR). The former is commonly used in experimental condensed matter physics to investigate fundamental particle dynamics and interactions, and the latter has become a powerful tool for measuring thermal properties of various materials and structures. In this chapter, we use the TDTR configuration of the developed instrumentation as an example to illustrate the general mechanism of ultra-fast optical microscopy from both the theoretical and the experimental perspective, which also works in other configuration variations, as well as the near-field ultra-fast optical microscopy covered in later chapters.

2.1 Introduction

Thermal conductivity (κ) is one of the most important concepts in thermal physics, which measures the capability of a material in conducting heat from high-temperature regions to low-temperature domains. Fourier's law of heat conduction states that the heat flux (q) is proportional to the temperature gradient (∇T) by the thermal conductivity:

Equation 2.1 Fourier's law of heat conduction

$$q = -\kappa \nabla T$$

The thermal conductivity of a material is usually temperature-dependent and can be directionally dependent, i.e., anisotropic. Another important concept frequently used in the theoretical framework of thermal physics is the interfacial thermal conductance (G), which is defined as the ratio of the heat flux to the temperature drop across the interface to characterize the interfacial resistance to the heat flow:

Equation 2.2 Definition of interfacial thermal conductance

$$q = G \Delta T$$

The thermal conductance is heavily dependent on the microscopic interfacial geometries, i.e., the micro-contact between the two media. The thermal conductivity dictates how the heat flux flows inside of a medium and the thermal conductance determines how it flows across the boundary between two distinct media. Theoretical

calculation of these thermal properties of many materials and systems has been possible due to advances in simulation methods, such as ab-initio first-principle calculation, molecular dynamics (MD), and density functional theory (DFT). However, for many complex materials and structures, theoretical prediction either is numerically challenging or struggles to account for important physical factors. To experimentally verify or validate theoretical predictions, a variety of measurement techniques and configurations have been deployed for materials over a broad range of temperatures, including the steady-state, transient hot-wire, transient plane source, IR imaging, and the 3ω methods.[56] These methods are typically low-cost and relatively easy to implement, albeit ill-suited for most nanomaterials and nanostructures that present small physical dimensions and are prone to experimental accuracy constraints.

Over the past two decades, laser-based optical techniques have received extensive attention and has become an unprecedented tool for thermal measurement due to their clean, noninvasive and versatile characteristics.[58 – 61] Among them, time-domain thermo-reflectance has emerged and evolved as the most powerful technique and has been applied for characterizing thermal properties of a large variety of samples including both thin films with a thickness down to ~20 nm and bulk materials.[62 – 72] In particular, time-domain thermo-reflectance (TDTR) technique has been used to measure materials with thermal conductivity ranging from a high end at ~2000 $W \cdot m^{-1} \cdot K^{-1}$ (such as diamond[73] and graphite[60, 71]) to as low as 0.03 $W \cdot m^{-1} \cdot K^{-1}$ (such as disordered WSe_2 films[62]). Beside thermal conductivity, thermal conductance of various solid/solid interfaces, and the heat capacity of new materials have also been successfully measured using TDTR.[74 – 83] Recently, TDTR has made notable contributions to significant achievements in thermal science.[13 – 17, 57] As a variation of the usual ultra-fast optical pump-probe technique, TDTR intrinsically has many advantages over other thermal conductivity measurement techniques that lead to its popularity. For example, it requires minimal sample preparation and no delicate design of electrical heaters or temperature sensors, and it works well in both ambient conditions and elevated temperature and/or in vacuum.[84, 85] Continuous efforts have been devoted to advancing the TDTR technique itself as well as its applications in thermal properties characterization of various material systems.

Most of the recently developed TDTR setup follows the prototype crafted by Cahill et al, based on a high-repetition-rate femto-second laser oscillator, typically a Ti:Sapphire oscillator with a repetition rate around 80 MHz, with laser pulses of a few hundred femtosecond duration and a central wavelength of around 800 nm.[59] Compared with lower repetition-rate systems, this has the advantage of a much higher signal-to-noise ratio since noise caused by variance of individual pulses is averaged, and more importantly, it allows to modulate the laser pulses at high frequency, reducing $1/f$ noise.[12] Such properties make it possible to work with small temperature excursions: the peak energy density of the pump pulses is on the order of 1 J/m^2, which usually leads to a temperature rise in the sample of less than 1 K for a single pulse. Following work has added a few new handy features to TDTR setup, such as dual-color pump-probe scheme which drastically reduces optical noise and allows for a simplified coaxial geometry, and an expanded probe beam which reduces divergence over the length of our delay stage and reduces systematic error caused by delay stage sweep.[12, 60 – 67]

We have constructed an ultra-fast optical pump-probe microscopy system that incorporates the TDTR measurement capacity in the Laser Thermal Laboratory at UC Berkeley. Our system follows the general TDTR prototype with a few customized features that will be discussed later in this chapter. We provide a detailed description of the design and implementation of the experimental instrumentation, and walk through the mechanism and theory, and then discuss some of the results obtained with the setup.

2.2 Experimental Instrumentation

Figure 2.1A shows the schematic of the ultra-fast optical pump-probe microscopy, and for clarity, some of the non-critical optical components are now illustrated. A mode-locked Ti:Sapphire laser oscillator (Tsunami from Spectra-physics) is used as the laser source (denoted as 'Femto' in the schematic), generating a train of femtosecond laser pulses at a repetition rate of 80 MHz. The laser wavelength is centered at 800 nm, and the laser pulse duration has a full width as half maximum (FWHM) of around 200 fs. The laser energy per pulse is around 50 nanojoules (nJ). The laser beam is then split into a pump beam and a probe beam through a beam splitter (BS, from CVI laser optics) with a ratio of 90:10. The major branch (90%) is then frequency-doubled through the second harmonic generation (SHG) by a nonlinear crystal (NLC), Beta Barium borate (BBO, from Eksma Optics, model number: BBO-601H) with thickness of 0.1 mm. From theoretical derivation in nonlinear optics, the converted intensity of the frequency-doubled laser light is proportional to the square of the incident intensity, as well as the square of the sinc of the phase mismatch:

Equation 2.3 SHG conversion relation

$$I_{2\omega} \propto I_{\omega}^{2} \cdot \left(\frac{\sin \delta}{\delta}\right)^{2} = I_{\omega}^{2} \cdot (sinc\ \delta)^{2}$$

where $I_{2\omega}$, I_{ω} and δ denote the converted intensity, the original intensity, and the (dimensionless) phase mismatch.

Therefore, in order to optimize the frequency doubling conversion efficiency, there are two necessary aspects to take into consideration, as illustrated in Figure 2.2. Firstly, since the output light from a laser oscillator without amplification has a high repetition around 80 MHz, and the typical laser intensity per pulse is way too small (~45 nJ) to achieve any measurable frequency doubling, it is critical to focus the incident laser beam into the nonlinear crystal to achieve an average intensity above 10^7 W/m^2, which is a typical baseline value for high-efficiency conversion. Note that this does not mean any laser with such intensity can achieve measurable second harmonic generation, instead, it is only achievable with ultra-fast pulsed lasers where the peak intensity of each ultra-short pulses can be as high as 10^{16} W/m^2, which is the fundamental key for the decent SHG conversion efficiency. To make the focusing as tight as possible, it is desired to use a lens with high numeric aperture (NA). The higher the NA, the tighter focal spot it can achieve. However, if the NA of the lens is too high, the thickness of the lens will unavoidably increase by a good amount, which may cause serious group dispersion, resulting in the significant

broadening of the femtosecond laser pulses. In our setup, we choose an ultra-thin lens specialized for femtosecond laser application (from Eksma Optics) with a focal length of 50 mm, as a trade-off between the tightness of the focusing and the thickness of the lens. Secondly, since the converted intensity is also proportional to the square of the sinc of the phase mismatch, and as shown in Figure 2.2B, the sinc function achieves its global maximum at 0, thus it is important to minimize the phase mismatch. In other words, the orientation of the nonlinear crystal needs to match well with the laser optical axis. For those two reasons, we have mounted the nonlinear crystal on a six-dimension-adjustable mounting (from Thorlabs) to achieve full spatial degrees of freedom adjustment (3 translational degrees and 3 rotational degrees). This is also the second reason why the focal length of the focusing lens cannot be too small, otherwise it is physically difficult to place and align the optical components.

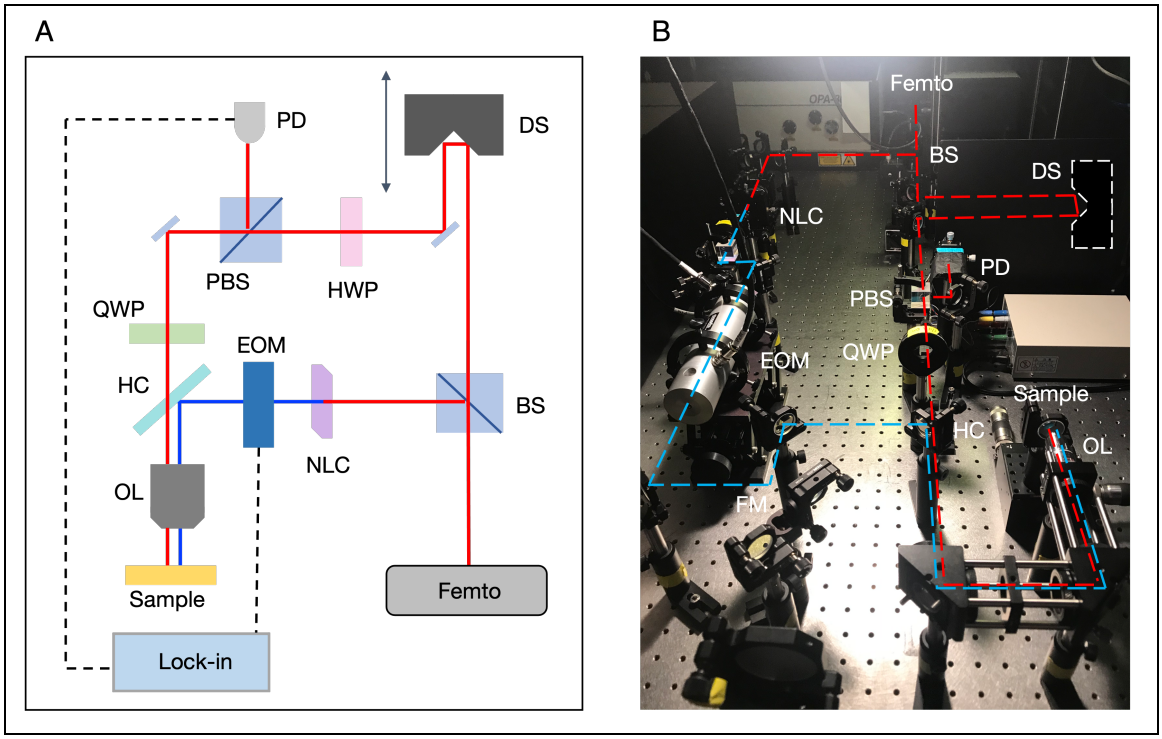

Figure 2. 1 (A) Schematic of the TDTR experimental implementation. The femtosecond laser beam is split into a pump beam and a probe beam through a beam splitter (BS). The pump beam is frequency-doubled through second harmonic generation (SHG) by a nonlinear crystal (NLC), and then is modulated by an electro-optic modulator (EOM) before being directed onto the sample through an objective lens (OL). The transient temperature decay is monitored by the probe beam, which is delayed with a mechanical delay stage (DS) for a femtosecond resolution. Changes in its reflectance signal is measured by a photodetector (PD) connected to a lock-in amplifier. A piezo stage is usually included to mount the sample. (B) A photo of the TDTR setup in Laser Thermal Lab. Note that the delay stage is hidden behind an optical shield (as indicated by the dashed shape near the top right corner, details is shown in Figure 2.3A). FM: flip mirror, it is flipped down in the photo (also in normal pump-probe microscopy experiments with a slightly different beam path), and when in TDTR operation, it is flipped up. The sample is mounted on a 3-axis piezo-stage with an optical mounting, and thus the orientation of sample can be adjusted in 5 degrees of freedom (except rotation around z-axis).

The typical conversion efficiency of SHG is on the order of 0.001 to 0.01. In our experiment, the frequency doubling conversion efficiency can achieve 2%: 4-Watt incident laser with wavelength of 800 nm can obtain around 80-mW of the 400 nm laser pulses. As a result, there is a large residual portion of 800-nm laser in the outgoing light after the nonlinear crystal, and after the divergent laser beam gets collimated by the second thin lens, we add a short-pass filter (from Semrock) which allows the 400-nm laser to pass and blocks the 800-nm laser. This optical filtration ensures that the pump beam is purely a train of pulses with central wavelength of 400 nm. Depending on the filtering power of the short-pass filter, a set of 2 ~ 4 short-pass filters put in series may be needed to eliminate the contamination from the residual 800-nm laser pulses in the pump beam. The mirrors (from Eksma Optics, model number: 032-0400) used in the subsequent pump beam path before merging with 800-nm probe beam are all narrow-band with a center wavelength at 400 nm (380 ~ 420 nm), which also helps to diminish the 800-nm residual in the pump beam.

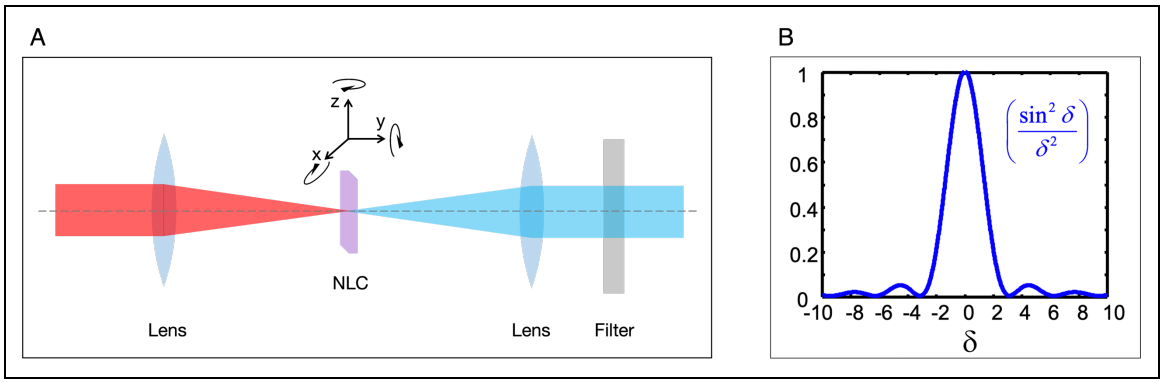

Figure 2. 2 (A) Schematic of the optics for efficient second harmonic generation. An ultra-fast femtosecond thin lens focuses the 800-nm laser into the nonlinear crystal (NLC), and a subsequent lens collects and collimates the frequency-doubled 400-nm laser beam. The NLC is mounted on a six-dimension-adjustable mounting to achieve full spatial degrees of freedom adjustment (3 translational degrees and 3 rotational degrees) to allow good alignment of the orientation of the NLC with the laser optical axis, in hope to minimize the phase mismatch of the frequency-doubling. (B) The square of sinc(δ) vs δ, showing that the global maximum is achieved when the phase mismatch (δ) equals 0.

The 400-nm pump laser beam is then directed to an electro-optic modulator (EOM, from Conoptics, model number: M350-160, with amplifier 25A), which modulates the amplitude of the laser pulses at a frequency in the range of 0.2 ~ 20 MHz. The imposed modulation is controlled by a sinusoidal wave function from a function generator (from Stanford Research Systems, model number: DS345), and the synchronized signal from the function generator is used as the reference input for lock-in detection. More detailed explanation about data collection and interpretation will be covered later in this chapter. The amplitude-modulated pump laser beam then merges its beam path with the probe beam through reflection by a harmonic combinator (HC, from Eksma Optics), which reflects the second-order harmonic wave, i.e., the 400-nm laser beam, and transmits the first-order harmonic wave, i.e., the 800-nm laser beam. Finally, the pump beam is focused on the same location on the sample surface with the probe beam by a long-working-distance objective lens (from Mitutoyo, model: 10x M Plan Apochromatic). The modulated pump pulses

excite the electron in the sample and thus heat up the sample surface, with each pulse creating an individual sharp temperature rise. The detailed theoretical framework will be discussed in later sessions.

The minor branch (10%) after the beam splitter serves as the probe beam. It is delivered to a mechanical delay stage (DS, from Thorlabs). As shown in Figure 2.3A, the delay stage is composed of a prism, which is mounted on the base of the delay stage, and one pair of mirrors, which are mounted on the motorized plate that can move along the track in a range of 0 ~ 220 mm. The plate can move with a precession down to 1 μm, providing a temporal resolution on the order of 1 femto-second. The probe beam passes along the delay track twice, thus the maximum corresponding delay time is around 1.47 nanosecond (ns). Usually when the optical path changes by a large amount will result in noticeable divergence of the beam: a collimated beam with $1/e^2$ radius w_0 will diverge according to:

Equation 2.4 beam propagation divergence

$$w = w_0 \left[1 + \left(\frac{\lambda z}{\pi w_0^2}\right)^2\right]^{1/2}$$

Here w is the $1/e^2$ radius of the beam after propagation, and λ is the wavelength and the z is the propagation distance.[86] When the optical path is delayed by 2 meters, the beam radius may increase by ~12%.[12] There are two methods to minimize the divergence: one option is using an optical fiber after the delay stage to maintain the beam shape and size[87], and the other option is to magnify the beam before the delay stage and demagnify the beam after the delay stage using a pair of beam expnaders[12]. However, both methods will cause significant group delay dispersion which would broaden the laser pulse to the order of 1 picosecond, and will add a fair amount of complexity to the whole system. Since our delay stage can only reach a maximum of 220 mm, the induced beam radius increase in the focal plane is below 1% at maximum delay range without any additional strategy to minimize the beam divergence, and more importantly we care more about preserving the 200-fs duration of the laser pulses to achieve best temporal resolution because we are interested to explore the very few picoseconds after the ultra-fast excitation by the pump, we here do not incorporate either of the two methods to minimize the probe beam divergence due to the optical path change during delay sweep, which is not necessary for our applications.

Existing from the delay stage, the probe beam then passes through a half wave plate (HWP, from Eksma Optics) and a polarized beam splitter (PBS, from CVI Laser Optics). This PBS can allow the horizontally polarized portion of the incident laser to pass through and reflect the vertically polarized portion. Rotating the half wave plate can effectively change the fractions of the horizontally polarized portion and the vertically polarized portion, therefore, the combination of the HWP and the PBS allows continuous tuning of the laser power. In addition, the PBS also plays an important role in redirecting the back-propagating probe beam reflected from the sample surface, as shown in Figure 2.3B. This is done with the help of the quarter wave plate (QWP) placed anywhere in between the PBS and the sample. When the probe beam passes through the QWP, it adds an additional $\pi/4$ phase to the probe laser light, changing the polarization of the probe beam to circularly

polarized. When the reflected probe beam (denoted as the orange dashed line) passes through the QWP, it adds another $\pi/4$ phase to the probe, changing its polarization to vertical. Therefore, when the reflected probe beam reaches the PBS, it is vertically polarized, and as mentioned above, the PBS will reflect the vertically polarized portion, thus this scheme successfully separates the forward-propagating and the back-propagating electromagnetic waves at the PBS. The reflected back-propagating probe beam is then collected by a high-speed PIN photodiode (PD, from Thorlabs, model number: DET10A), and the voltage output of the photodiode is fed into a lock-in amplifier (from Stanford Research Systems, model number: SR844) for signal demodulation.

One critical issue here is that the reflected 400-nm light should not get collected by the photodetector, otherwise the artifact it would produce will make it impossible to distinguish the real signal that we want to measure, which is the amplitude of the reflected 800-nm light at the demodulation frequency after the Fourier transform (details will be covered later in this chapter). However, due to the small value of thermo-reflectance coefficient dR/dT ($\sim 10^{-4}$ K^{-1}), a tiny amount of reflected pump beam even with an intensity less than 0.01% of the reflected probe beam is sufficient to contaminate the TDTR measurements.[88] To ensure the total elimination of the 400-nm light from the collected signal, a set of 3 ~ 5 long-pass filters in series is put in front of the photodiode to block the 400-nm from entering the sensor.

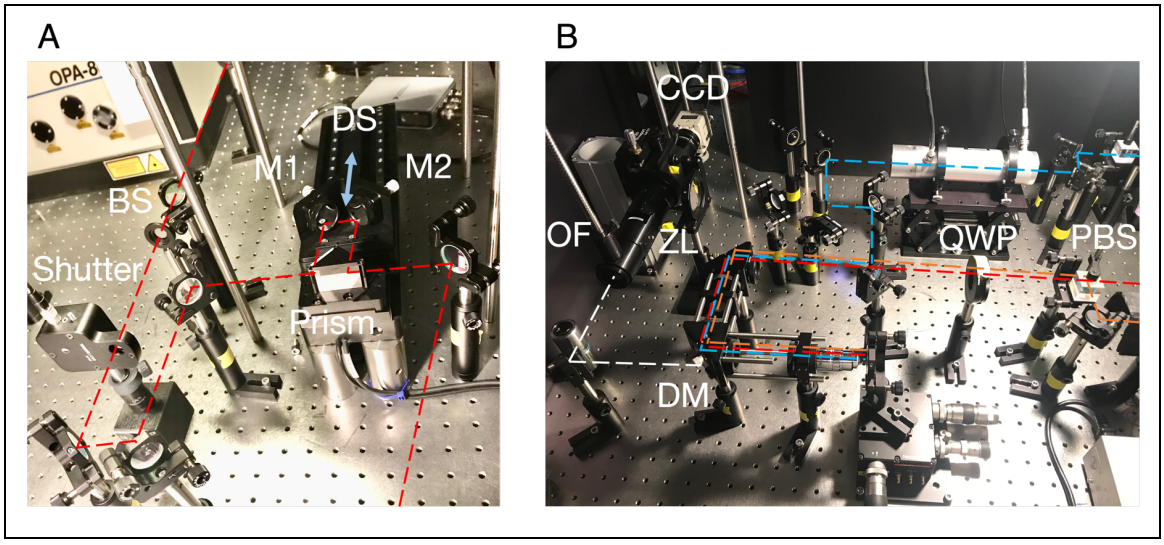

Figure 2.3 (A) A photo of the delay stage. the delay stage is composed of a prism, which is mounted on the base of the delay stage, and one pair of mirrors (M1 and M2), which are mounted on the motorized plate that can move along the track in a range of 0 ~ 220 mm. The probe beam passes along the delay track twice, thus the maximum corresponding delay time is around 1.47 nanosecond. (B) A photo of partial experimental setup, showing the merge of the pump beam (red dashed line) and the probe beam (blue dashed line). The reflected probe beam passes through the quarter wave plate (QWP) twice, adding a total of $\pi/2$ phase, thus the polarization changes from the original horizontal polarization to vertical polarization, and eventually gets reflected by the PBS and redirected to a photodiode. A high-sensitivity colored charge-coupled device camera system (CCD) mounted on a zoom lens (ZL) is used to monitor the alignment of the two laser beams. An optical fiber (OF) is mounted in the front of the zoom lens to deliver white light through the dual-band mirror

(DM), denoted as the white dashed line. The tiny leakage (~1%) of the pump and the probe beams from the DM is used for imaging with the high-sensitivity CCD.

In addition, a high-sensitivity colored charge-coupled device camera system (CCD, from Hitachi, model number: KP-D20AU) mounted on a zoom lens (ZL) is used to monitor the alignment of the two laser beams. An optical fiber (OF) is mounted in the front of the zoom lens to deliver white light. The dual-band mirror (DM, from Eskma Optics, model number: 062-4080) reflects both the 400-nm pump beam and the 800-nm probe beam, while allows visible wavelength range light to pass through, denoted as the white dashed line in Figure 2.3B. The tiny leakage (~1%) of the pump and the probe beams from the DM can be used for imaging with the high-sensitivity CCD. The integration of the CCD system brings a few advantages. Firstly, it enables the user to view the sample in microscale and accurately determine which regions are measured, which is very handy when the sample size is small. Secondly, it allows the user to visually check the overlapping of the pump and probe spots for best alignment. Thirdly, bringing the sample into focus ensures that it is a known distance from the objective, so that the sizes of the focused beam spots are known beforehand. Characterizing the size of the beam spots is done with the so-called knife edge measurement[87]: the pump beam has a $1/e^2$ radius (ω) of 9.93 μm, and that of the probe beam is 3.26 μm in our measurement.

So far, we have provided an informative overview of the TDTR experimental setup, which solidifies and simplifies previous developed systems by Cahill et al[59] and Chen et al[12]. We have covered most of the essential optical components to ensure the basic functionality of TDTR, and have discussed some of the critical technical details for successful measurements. One thing to notice is that as shown in the photos of the physical setup, there are many more optical components that are not included in the schematic illustration, most of which are auxiliary mirror pairs to facilitate easy alignment of the beam paths.

2.3 Theoretical Framework of TDTR

The common analytical strategy used in all variations of the pump-probe technique, data analysis requires that the experimental data is compared to a theoretical model, the unknown properties of interest are deduced from the fitting of the experimental data against the model, that is, the target properties are treated as free parameters to be tuned such that the error between the model and the data is minimized. Cahill et al[59] and Schmidt et al[12] have established a general system-perspective heat transfer model that lays the foundation and nourishes the theoretical study of TDTR. Here we recapitulate some of the key steps and conclusions that not only benefits the data analysis of our research work in the far-field study, but also provides inspirations for the near-field study (covered in later chapters).

In traditional heat conduction, superposition is a commonly used technique for solving complex problems, which holds when the temperature changes are small enough that

physical properties can be safely assumed constant. This underlying idea is well-formulated in the theory of linear time-invariant (LTI) systems: the response of the system to multiple inputs is the sum of the responses to each individual input. The well-developed framework of LTI provides a convenient way to handle the TDTR modeling.

In our TDTR system, laser pulses from the pump beam arrive at the substrate with a frequency of 80 MHz, and each individual pulse has a width of around 200 fs. Since the pulse width is much shorter than the interval between two consecutive pulses, each individual pulse is treated as an impulse with energy Q. To start with, let us consider the response of the thermal system to a train of pulses that are amplitude-modulated by a sinusoid function, as shown in Figure 2.4A. Note that in reality there is a DC term with value of half the maximum amplitude such that the minimum is 0. However, this DC term does not contribute to the periodic response of the LTI system, and it will be rejected by the lock-in amplifier, thus it is ignored in the discussion. Each impulse of heat generates a temperature response in the sample, which may not die away before the next pulse arrives. This so-called "accumulation" effect indeed provides a way to measure the response at a longer delay time scale beyond the range of the delay stage, as we will see later in this chapter. Figure 2.4B shows a schematic of the surface temperature profile in response to the pump pulses in time domain. The probe pulses arrive at the sample surface delayed from the corresponding pump pulses by a time τ, which is determined by the position of the delay stage, as shown in Figure 2.3C. These pulses are reflected by the sample back into the photodiode.

Figure 2.4D depicts the probe pulses sampling the surface temperature. Although the probe pulses also heat up the sample, and indeed its effect may even be stronger than the pump pulses in our measurement for higher signal-to-noise ratio, this has no effect on the measurement results. This is because the probe beam is not modulated by the EOM and the optical signal collected by the photodiode has no frequency component at the modulation frequency and thus its contribution to the signal will be rejected by the lock-in amplifier. This assumption is valid as long as the probe beam is not strong enough to cause the sample to behave in a nonlinear way, i.e., the linear time-invariance assumption still holds. Collectively, these probe pulses excite the photodiode. The component of this probe signal at the reference frequency will be recorded by the lock-in amplifier, while all other frequencies, such as the fundamental laser repetition rate, 80 MHz, will be rejected. In our experiments, the lock-in amplifier time constant is set to 30 ms, which gives a pass band of roughly 10 Hz.[89] Therefore, all the probe frequencies will be well outside the narrow lock-in pass band, and we can safely think that the lock-in amplifier output solely represents the frequency component of the signal at the modulation frequency. The solid line depicts the modulation envelope which serves as the reference for the lock-in amplifier. The dashed red line "connects the dots" of the probe pulses to highlight the fundamental harmonic component purely induced by the modulated pump pulses. Both its amplitude and phase lag with the reference modulation are recorded by the lock-in at each delay position.

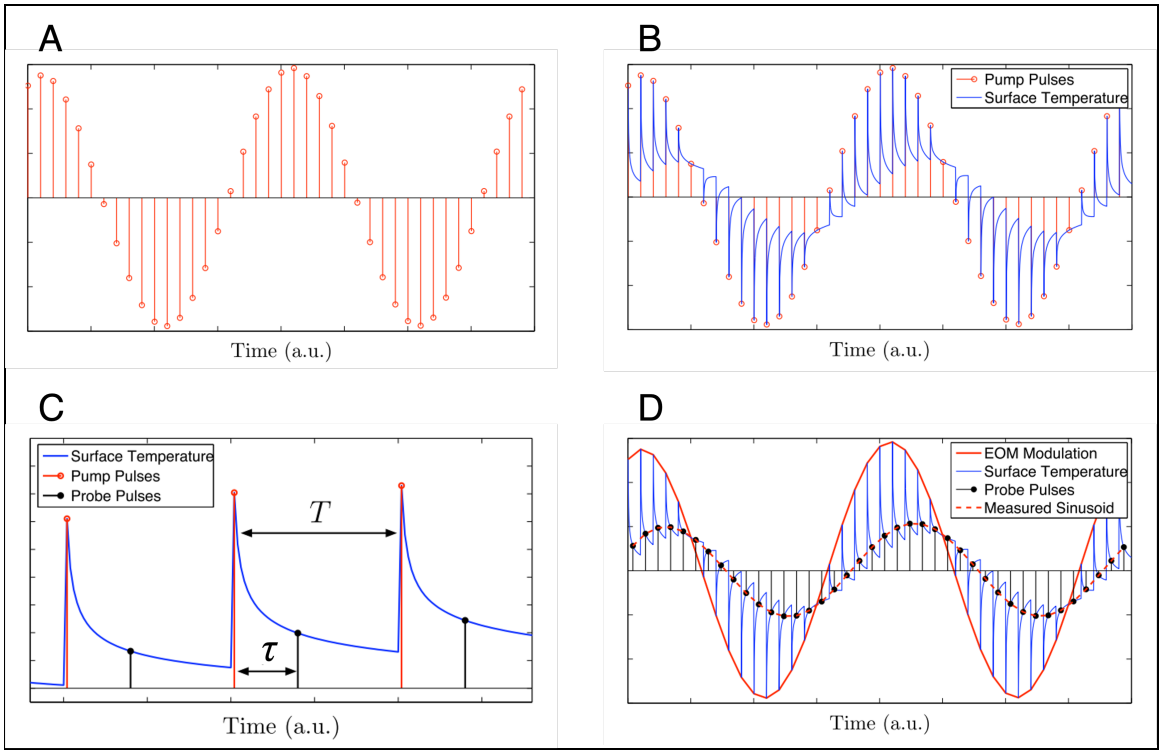

Figure 2.4 (A) Schematic of the pump beam pulses in time domain after passing through the EOM. Although the real modulation of the EOM has a DC offset, the lock-in amplifier only measures the fundamental harmonic, so an idealized sinusoid may be used. (B) Schematic of the surface temperature of the sample in response to the pump beam pulses input. (C) The probe pulses arrive at the sample surface later than the corresponding pump pulses at a delay time (τ) set by the delay stage. (D) Schematic of the relationship between the pump modulation and the corresponding modulation in probed signal as a result. Since the probe beam is not modulated by the EOM, the effect of the probe pulses on the surface temperature does not contribute to the output of the lock-in amplifier. This assumption is valid as long as the probe beam is not strong enough to cause the sample to behave in a nonlinear way, i.e., the linear time-invariance assumption still holds. The solid line depicts the modulation envelope which serves as the reference for the lock-in amplifier. The dashed line connecting the probe pulses is the fundamental harmonic of the probe signal caused by the pump beam. Both the magnitude of this sinusoid and its phase lag from the reference frequency are measured by the lock-in amplifier at every position of the delay stage.[12]

The time-domain representation of the amplitude-modulated pump pulses and can be written as:

Equation 2.5 Pump pulses representation

$$q(t) = e^{i\omega_0 t} \sum_{m=-\infty}^{\infty} Q\delta(t - mT)$$

Here Q is the energy of the impulse, ω_0 is the EOM modulation frequency, δ is the delta function, t is the time, and T is the laser pulse period (12.5 ns for our setup). The temperature response to an impulse of heat with strength Q, $Q\delta(t)$, is $Qh(\boldsymbol{r}, t)$, where $\boldsymbol{r}$ is the spatial coordinate and, and $h(\boldsymbol{r}, t)$ denotes the unit impulse response of the thermal

system. The response to a time varying heat input $q(t)$ at the same location is given by the convolution:

Equation 2.6 temperature response

$$\Theta(\boldsymbol{r},t) = q(t) * h(\boldsymbol{r},t) = \int_{-\infty}^{\infty} q(t')h(\boldsymbol{r},t-t')dt'$$
$$= Q\sum_{m=-\infty}^{\infty} e^{i\omega_0 mT}h(\boldsymbol{r},t-mT)$$

Here Θ denotes the sample surface temperature. The reflectivity of the sample is assumed proportional to its surface temperature since the temperature perturbation is small. Therefore, the reflected probe light is described by $\beta\Theta$ multiplied by the incident probe pulses input, where β is a constant that includes the thermo-reflectance coefficient and gain of the electronics. Mathematically, the collected raw probe signal can be written as:

Equation 2.7 collected raw probe signal

$$\mathrm{z}(t) = \beta\Theta(t)\sum_{n=-\infty}^{\infty} Q_{probe}\delta(t-nT-\tau)$$
$$= \left(\beta Q Q_{probe}\sum_{m=-\infty}^{\infty} e^{i\omega_0 mT}h(t-mT)\right)\sum_{n=-\infty}^{\infty} Q\delta(t-nT-\tau)$$

Here Q_{probe} is the energy per probe pulse, and we have dropped the spatial variable $\boldsymbol{r}$ in the impulse response for simplicity. Taking the Fourier transform of equation 2.7, the frequency-domain representation of the collected raw probe signal can be expressed as:

Equation 2.8 Fourier transform of probe signal

$$\mathcal{F}[\mathrm{z}(t)] = Z(\omega) = \int_{-\infty}^{\infty} z(t)e^{-i\omega t}dt$$
$$= \beta Q Q_{probe}\sum_{n=-\infty}^{\infty}\sum_{m=-\infty}^{\infty} e^{i\omega_0 mT}h(\tau-mT+nT)\,e^{-i\omega(nT+\tau)}$$

$$= \frac{\beta Q Q_{probe}}{T}\sum_{k=0}^{\infty} e^{-i\omega_0(kT+\tau)}h(kT+\tau)2\pi\delta(\omega_0-\omega)$$

The last step is achieved by defining $k = n - m$, and taking the fact that $h(t) \equiv 0$ for $t < 0$, along with some algebra derivations. Taking the inverse Fourier transform:

Equation 2.9 inverse Fourier transform of probe signal

$$z(t) = Z(\omega_0)e^{i\omega_0 t}$$

Equation 2.10 probe signal amplitude

$$Z(\omega_0) = \frac{\beta Q Q_{probe}}{T} \sum_{k=0}^{\infty} h(kT+\tau) e^{-i\omega_0(kT+\tau)}$$
$$= \frac{\beta Q Q_{probe}}{T^2} \sum_{k=-\infty}^{\infty} H(\omega_0 + k\omega_s) e^{ik\omega_s\tau}$$

As we discussed earlier, we measure the fundamental harmonic of the probe signal caused by the pump beam, and both the magnitude (R) of this sinusoid and its phase lag (φ) from the reference frequency are measured by the lock-in amplifier at every position of the delay stage. Specifically, in TDTR we measure the in-phase (X) and out-of-phase (Y) components of this signal, equivalent to R and φ through $R = \sqrt{X^2 + Y^2}$ and $\tan(\varphi) = \frac{Y}{X}$. The X and Y are indeed the real part and the imaginary part of $Z(\omega_0)$, which can be expressed as:

Equation 2.11 lock-in output components

$$X = Re\{Z(\omega_0)\}$$
$$Y = Im\{Z(\omega_0)\}$$

The above derivation sets up the general framework for the data interpretation from the perspective of LTI system. Note that this framework does not depend on the details of the system response, which only comes in play through the response function $h(t)$, or its frequency-domain counterpart, the transfer function $H(\omega)$. Therefore, this framework can help to study not only the thermal response of the system, as in TDTR measurement, but also other ultra-fast events, including photo-induced electron-hole generation in semiconductors. The latter will be the emphasis of the latter chapters.

As seen from the Equation 2.10, the true signal we are measuring here, $Z(\omega_0)$, is linearly proportional to the thermo-reflectance coefficient, which is lumped in β. In order to achieve sufficient signal-to-noise ratio, the thermo-reflectance coefficient needs to be relatively high. Unfortunately, not many materials have good thermo-reflectance coefficient for TDTR to work reliably. To solve this problem, the sample is usually deposited with a thin layer of metal with thickness of ~100 nm by electron-beam physical vapor deposition (EBPVD) or other fabrication techniques. This thin metal film has two purposes: firstly, the metal layer absorbs the pump laser pulse energy and convert into thermal energy, and secondly it acts as the temperature transducer due to the temperature dependence of its reflectivity. Therefore, a good candidate for these purposes must have strong absorption near 400 nm, and present a high thermo-reflectance coefficient at 800 nm. A commonly used material is aluminum, whose absorption depth at 400 nm is ~35 nm and thermo-reflectance coefficient is ~1.4×10^{-4} K^{-1} at 800 nm. Therefore, the typical material system investigated by TDTR is a two-layer structure: a thin aluminum layer on top of the bulk material of interest.

To mathematically formulate the heat transfer model in layered structures, here we adopt the approach described in *Conduction of Heat in Solids* by Carslaw and Jaeger[90] for

one-dimensional conduction. Figure 2.5A illustrates the problem for a single layer with heat flow in the *z* direction. In the frequency domain, thermal response of the sample, $H(\omega)$, can be found by relating the temperature, θ_t, and heat flux, f_t, on the top side of the slab to the temperature, θ_b, and heat flux, θ_b, on the bottom side through:

Equation 2.12 1D heat conduction in a slab

$$\begin{bmatrix} \theta_b \\ f_b \end{bmatrix} = \begin{bmatrix} \cosh(qd) & \frac{-1}{\kappa_z q}\sinh(qd) \\ \kappa_z q \sinh(qd) & \cosh(qd) \end{bmatrix} \begin{bmatrix} \theta_t \\ f_t \end{bmatrix}$$

Here d and κ_z are the layer thickness and the cross-plane thermal conductivity, respectively. $q^2 = i\omega/\alpha$, where α is the thermal diffusivity. The problem of one-dimensional heat flow through multiple layers is illustrated in Figure 2.5B. Mathematically, multiple layers are handled by multiplying the matrices for individual layers together:

Equation 2.13 1D heat conduction in multi-layers

$$\begin{bmatrix} \theta_b \\ f_b \end{bmatrix} = \mathrm{M}_n \mathrm{M}_{n-1} \cdots \mathrm{M}_1 \begin{bmatrix} \theta_t \\ f_t \end{bmatrix} = \begin{bmatrix} A & B \\ C & D \end{bmatrix} \begin{bmatrix} \theta_t \\ f_t \end{bmatrix}$$

Here M_n is the matrix for the bottom layer. Each matrix contains the thickness and thermal properties of one layer of material in the same fashion as shown in equation 2.12. If the bottom surface of the *n*th layer is assumed to be adiabatic, or if the *n*th layer is treated as semi-infinite, then in both cases Eq. 2.13 reduces to $C\theta_t + Df_t = 0$, and the surface temperature will be given by:

Equation 2.14 relation between surface temperature and heat flux

$$\theta_t = \frac{-D}{C} f_t$$

Here f_t is the heat flux boundary condition applied to the top surface. In all the experiments, the semi-infinite boundary condition is a valid assumption since the bottom bulk material always has a large thickness compared with the thermal penetration depth. One important factor has not been taken into consideration is the interfacial thermal resistance between materials layers, which comes from sources such as acoustic and electronic impedance, as well as the microscopic interfacial contact quality. As discussed in the beginning of this chapter, thermal conductance (G) is introduced to account for this effect. Mathematically, Equation 2.2 can be reformulated as:

Equation 2.15 heat flux across interface

$$f = G(\theta_t - \theta_b)$$

Here f is the heat flux across the interface and θ_t and θ_b are temperatures on either side. Denoting the heat flux on top side and bottom side with f_t and f_b, respectively, use the fact that the heat flux across the boundary is constant (f), and rearrange Equation 2.15 into a matrix form in a similar fashion with equation 2.12:

Equation 2.16 heat flux across interface in matrix form

$$\begin{bmatrix} \theta_b \\ f_b \end{bmatrix} = \begin{bmatrix} 1 & G^{-1} \\ 0 & 1 \end{bmatrix} \begin{bmatrix} \theta_t \\ f_t \end{bmatrix}$$

Therefore, the interface is effectively abstracted by another material layer with a close-to-zero heat capacity, a diminishing thickness (d) and an effective cross-plane thermal conductivity $\kappa_{z,e}$ such that $G = \kappa_{z,e}/d$. When fitting experimental data, the thickness usually is set to 1 nm, and $\kappa_{z,e}$ is treated as a free parameter for tuning.

To extend this framework to 2-dimensional to take into consideration the radial thermal transport and anisotropic effect, Cahill et al[59] introduced a Hankel transformation to solve the problem. Besides, since both the pump beam and the probe beam have a gaussian-distribution energy profile in the cross-section, spatial convolution is sufficient under the LTI assumption, which essentially employs the powerful idea of superposition. Without going further into the details, here we present the final formula for the transfer function of the multi-layer thermal system under investigation, as shown in Figure 2.5C.

Equation 2.17 transfer function for multi-layer thermal system

$$H(\omega) = \frac{A_0}{2\pi} \int_0^\infty k \left(\frac{-D}{C}\right) \exp\left(\frac{-k^2(w_0^2 + w_1^2)}{8}\right) dk$$

Here A_0 is the power absorbed, w_0 is the $1/e^2$ radius of the pump beam, and w_1 is the $1/e^2$ radius of the probe beam. Additionally, taking the radial heat transfer into consideration requires a modification for the definition of q in Equation 2.12. Let the radial thermal conductivity, the density, and the specific heat denoted as κ_r, ρ, and c, respectively:

Equation 2.18 revised definition of thermal wave vector

$$q^2 = \frac{\kappa_r k^2 + \rho c i\omega}{\kappa_z}$$

Here k is the dummy integral variable used in Equation 2.17. Equations 2.10, 2.12, 2.13, 2.16, 2.17 and 2.18 provide the complete theoretical solution for TDTR measurements that the experimental data can be fitted against. As mentioned earlier, the most common material system is a bulk material of interest with a thin film of aluminum deposited on top. Thus, there are effectively three layers in this configuration: the aluminum transducer layer (layer 1), the abstract interface layer (layer 2), and the bulk material of interest layer (layer 3). For such sample system, there are typically two free parameters used in the fitting: one is the thermal conductivity of the material of interest (layer 3), and the other one is the effective thermal conductivity of layer 2, which equals interface thermal conductance divided by the nominal thickness (usually set to 1 nm).

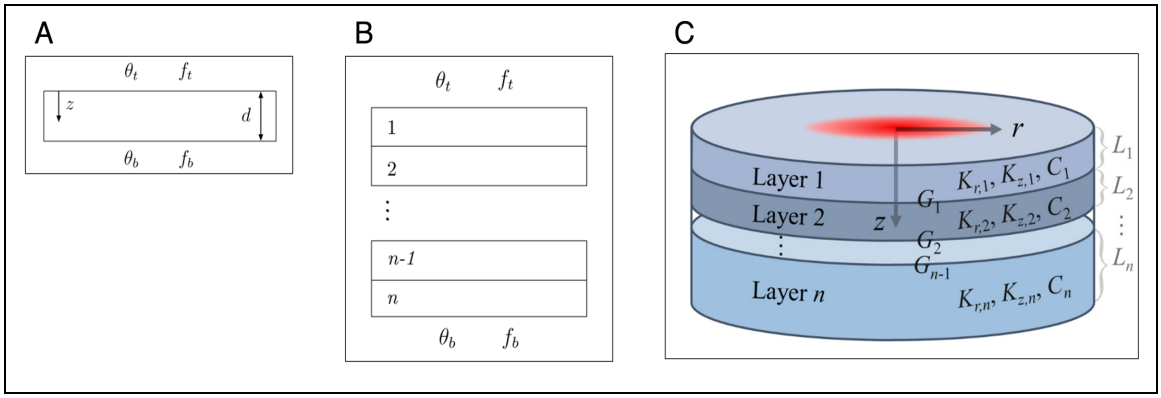

Figure 2.5 (A) Conduction through a one-dimensional slab. The temperature and heat flux on the top surface, θ_t and f_t, can be related to the temperature and heat flux at the bottom surface, θ_b and f_b, through a matrix equation. (B) Schematic of one-dimensional heat conduction through multiple layers. (C) Schematic of TDTR material model, two-dimensional heat conduction through multiple layers with gaussian-distributed surface heat flux.

2.4 TDTR Results

Figure 2.6 provides some examples of the TDTR measurements results. The sample under investigation is a piece of bulk silicon with a thin film of aluminum deposited on the top surface. The silicon has a thickness around 1 mm, which is sufficient enough to satisfy the adiabatic condition assumed in the theoretical modeling (equation 2.14), i.e., the sample is thick enough such that the heat flux exiting from the bottom surface of the silicon layer can be regarded as zero. The aluminum layer has a thickness of 103.5 nm, measured from atomic force microscopy (AFM) and laser confocal microscopy (LCM). A sinusoid wave is used to modulate the amplitude of the pump beam. In Figure 2.6, measurement results on the same sample with two different modulation frequencies are demonstrated: in A and B, the modulation frequency is 0.9375 MHz, and in C and D, the modulation frequency is 9.5 MHz. Typical modulation frequency used in TDTR ranges from 0.2 MHz to 20 MHz. In general, the sensitivity of the TDTR measurement increases as the modulation frequency increases. However, if the modulation frequency is too high, there will be only several laser pulses within one modulation period, which causes significant noise in the measured signals, since the variation in the energy of the pulses will invalidate those important assumptions made in the theoretical framework. For example, the pulse energy strength Q used in Equation 2.5 cannot be considered as a constant in this case.

In the multi-layer thermal system described above, there are 3 parameters per layer that our model cares about, the thermal conductivity (κ), the heat capacity (ρc), and the layer thickness (d). [For anisotropic material, both axial conductivity (κ_z) and the radial conductivity (κ_r) will be included.] In our example, the three layers from the top to the bottom are the aluminum thin film, the abstract interface layer, and the silicon layer. Table 2.1 summarizes all the parameters used in the fitting process.

Table 2.1 Parameters used in fitting

	Thermal conductivity (κ, W·m^{-1}·K^{-1})	Heat capacity (ρc, J·m^{-3}·K^{-1})	Thickness (d, m)
Aluminum	110	2.396×10^6	103.5×10^{-9}
Interface	0.165*	1**	1×10^{-9}**
Silicon	145.1*	1.549×10^6	10^{-3}

Note: * denotes the free parameters for tuning to minimizing the error between the theoretical calculation and the experimental data. ** denotes the pre-set parameters that are chosen to mimic real physical situation.

Figure 2.6A and C illustrate the calculated (denoted as the black solid line) and the experimental (red hollow dots) values of the negative ratio of the in-phase component (X, V_{in}) over the out-of-phase component (Y, V_{out}) of the output from the lock-in amplifier, defined by Equation 2.11, versus the time delay. The fitting is done by tuning the two free parameters, the thermal conductivity of the silicon (κ_{Si}) and the nominal thermal conductivity of the interface ($\kappa_{interface}$), so as to minimize the sum of the difference between the experimental value $(-V_{in}/V_{out})_{\text{exp}}$ and calculated value $(-V_{in}/V_{out})_{\text{cal}}$ across the whole delay time range, i.e., the error function is the sum of least square of the deviation between these two values across the whole delay time range:

Equation 2.19 TDTR fitting error function

$$\mathbb{E}\left[-\frac{V_{in}}{V_{out}}\right] = \sum_{\tau_{exp}} \left| -\frac{V_{in,exp}}{V_{out,exp}} - \left(-\frac{V_{in,cal}}{V_{out,cal}}\right)\right|^2 \to 0$$

There are two major reasons why we choose the $-V_{in}/V_{out}$ as the target variable for fitting. First of all, the ratio is dimensionless, and compared with fitting V_{in} or V_{out} solely, it eliminates lot of experimental errors that may cause severe problem for the optimization. For example, as we discussed earlier, when the delay stage moves to large delay time, the divergence of the probe beam could cause the radius of the probe on the sample surface to be slightly delay-time-dependent, which may bring systematic errors in the measured V_{in} and V_{out}. Since the signal is linearly proportional to the laser, this fact will have the same effect on the measured V_{in} and V_{out}, taking the ratio of them effectively cancels out the power-dependence. This is the same reason for some other TDTR users to choose the phase $[\varphi = \arctan(V_{out}/V_{in})]$ as the target variable of fitting. Secondly, instead of fitting the phase, we choose its inverse counterpart, this is because mathematically V_{in}/V_{out} has high sensitivity in the shorter range of delay time (0 ~ 1 ns), while V_{in}/V_{out} has high sensitivity in the longer range of delay time (1 ~ 4 ns). This is also one of the reasons that other TDTR researchers only fit the data after 1ns.[12] Since our delay stage can only reach a maximum of around 1.44 ns, we choose the V_{in}/V_{out} as the target variable of fitting. The negative

sign does not have any effect on the fitting, it is set only to make the plot in the positive regime.

In Figure 2.6A, when using a modulation frequency of 0.9375 MHz, the measured thermal conductivity of the silicon sample is 145.1 $W \cdot m^{-1} \cdot K^{-1}$, and the measured thermal conductance of the interface is 165 MW·m-2·K-1. The measured thermal conductivity agrees well with literature and results from other TDTR research groups.[58 – 62] The interface thermal conductance is heavily dependent on the sample surface roughness and the metal deposition technique used to prepare the sample; therefore, it varies a lot from sample to sample. Reasonable results for the interface between aluminum and silicon are in the range from 50 to 300 $MW \cdot m^{-2} \cdot K^{-1}$.[58 – 62] Our results are very well within this range. In Figure 2.6C, when using a modulation frequency of 9.5 MHz, the measured results for the thermal conductivity of silicon and the interface thermal conductance are 144.8 $W \cdot m^{-1} \cdot K^{-1}$ and 170.1 $MW \cdot m^{-2} \cdot K^{-1}$, respectively, agreeing well with the case of 0.9375 MHz.

In our measurement, multiple modulation frequencies within the range from 0.5 MHz to 20 MHz are used to measure the same region on the sample. For each frequency, 5 runs are performed at different locations within a 10 × 10 μm region of the sample surface. Table 2.2 summarizes the averaged results for the thermal conductivity of silicon and the interface thermal conductance, along with the normalized variance among each group of measurement runs. Within this frequency range, we did not observe any modulation-frequency dependencies in the measured results, which validates the theoretical framework described above. Modulation frequencies out of this range are also tested, as low as ~1 kHz or as high as 40 MHz, however, due to the low sensitivity in the low frequency case and the high noise level in the high frequency case, optimization in the fitting process can easily get stuck in local minimums of the error function defined in Equation 2.19, thus the parameters of interest deduced from the fitting may have strong dependence on the initial values used in the optimization. Perhaps advanced optimization techniques, such as machine learning, can help to increase the reliability of the fitting in such situation, but this is beyond the topic of this work. Note that the variances are relatively large at frequencies 2.687 and 4.979 MHz, this is because that the lock-in amplifier (SR844) that we use has poor screening ability for coherent radio frequency pickup in the range from 1 to 5 MHz.[12, 89] We have used RF chokes, which are ferrite toroidal cores around which the cables are wrapped, to attenuate RF current flowing along the outside of the coaxial signal lines and in the power cord.[12] However, this cannot fully cancel out the contributions from the RF pickup. Therefore, we usually use frequencies outside of this range. The other range of frequencies that present higher variance is 15 ~ 20 MHz. As previously discussed, this is due to the strong contribution from the energy variance of the laser pulses since there are less than 6 pulses in one modulation cycle. In this range, the raw V_{in} and V_{out} signals have fairly high noise levels, which propagate and get amplifed in the ratio V_{in}/V_{out}, thus lead to large variances in the fitted parameters among a group of runs with the same experimental configurations.

Table 2.2 Measured results for various modulation frequencies

Modulation frequency (ω_0, MHz)	Thermal conductivity ($\bar{\kappa}_{Si}$, W·m^{-1}·K^{-1})	Variance ($\overline{\overline{\sigma}}_{\kappa}$)	Thermal conductance ($\bar{G}$, MW·m^{-2}·K^{-1})	Variance ($\overline{\overline{\sigma}}_{G}$)
0.531	143.6	1.6%	160.3	5.9%
0.938	145.0	1.2%	165.0	3.0%
2.687	145.3	8.7%*	167.2	12.9%*
4.979	145.9	9.3%*	173.5	14.1%*
7.511	146.7	0.5%	178.7	6.3%
9.506	144.8	0.7%	159.1	5.9%
12.189	143.8	2.2%	155.6	8.7%
15.215	144.1	3.7%	163.3	9.0%
17.923	146.0	5.6%**	170.8	13.2%**
20.039	145.8	7.1%**	168.7	12.7%**

Note: * denotes the abnormally high variances due to the lock-in amplifier's poor screening of the RF pickup.
** denotes the high variances due to strong contribution from energy variance of the laser pulses.

Figure 2.6B and D plot the V_{in} and V_{out} normalized to the calculated temperature increase of the sample. In both cases, the experimental data do not perfectly match with calculated values. The major reason is that as the delay stage moves, the divergence of the probe beam cause the beam radius to undergo a slight change. Additionally, the experimental data in 0.9375 MHz case are slightly noisier than those of 9.5 MHz case. This is due to the so-called 1/f noise, or "pink noise," fluctuations in the probe intensity around the reference frequency, as discussed in reference [12].

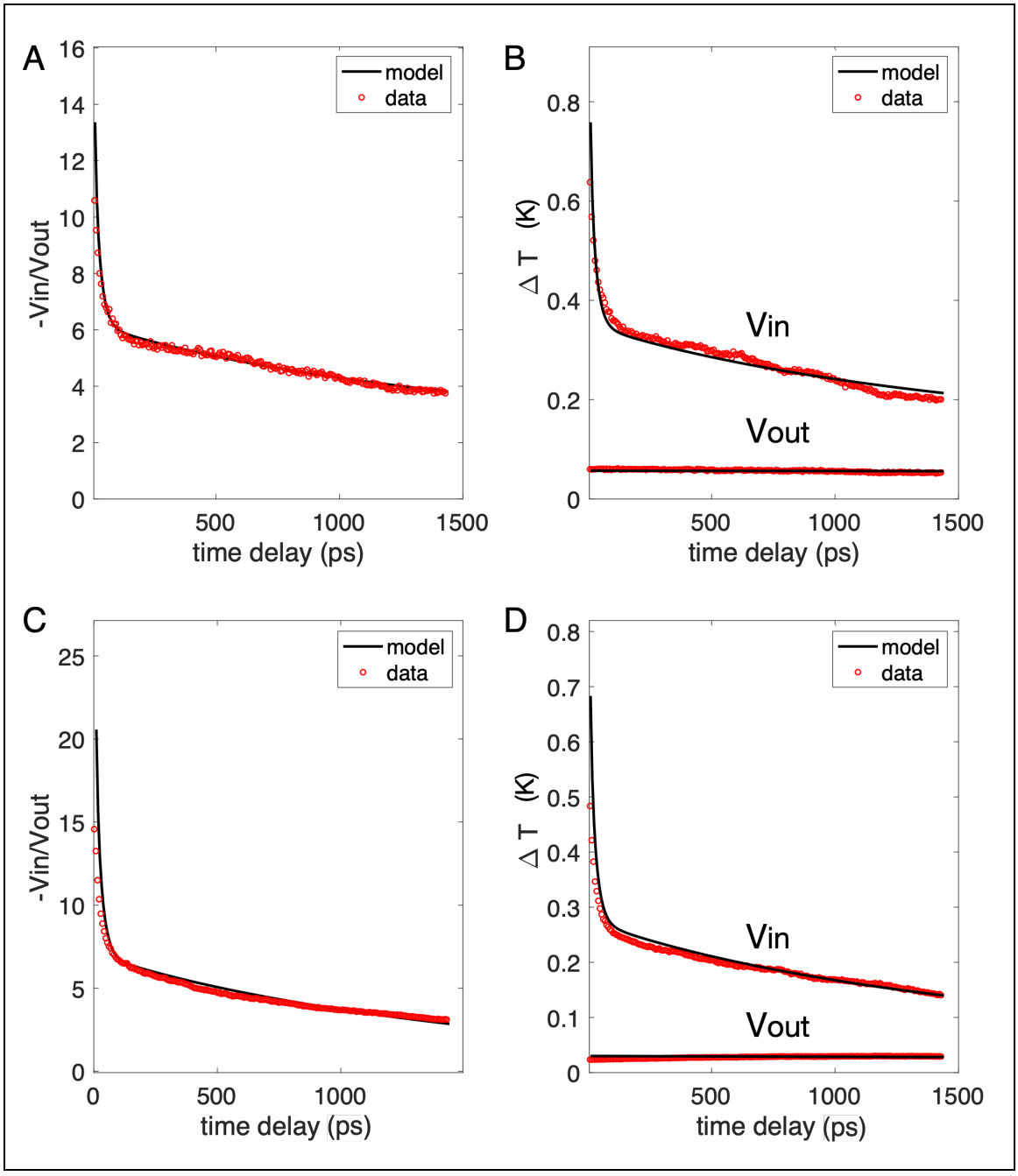

Figure 2.6 (A) and (C) plot the calculated (the black solid line) and the experimental (red hollow dots) values of $-V_{in}/V_{out}$ versus the time delay for modulation frequency of 0.9375 MHz and 9.5 MHz, respectively. (B) and (D) plot the V_{in} and V_{out} normalized to the calculated temperature increase of the sample versus the time delay for modulation frequency of 0.9375 MHz and 9.5 MHz, respectively.

One fact observed from Table 2.2 is that across the frequency range, the averaged measured thermal conductivity of the silicon sample ($\bar{\kappa}_{Si}$) are roughly around 145 W·m-

$^{1}\cdot K^{-1}$, and the corresponding normalized variances are all small expect the two mentioned abnormalities, but the interface thermal conductance ($\bar{G}$) has a much wider range (155.6 ~ 178.7 $MW\cdot m^{-2}\cdot K^{-1}$), and the corresponding variances are much larger than those of the thermal conductivity results. The reason is that the measurement has much higher sensitivity on the thermal conductivity of the material under investigation than the interface thermal conductance. To quantify how sensitive the measurement is to the parameter of interest, ξ, we need to evaluate the degree to which the target variable of fitting, R, depends on ξ. Mathematically, the sensitivity of R to a parameter ξ is defined as[76, 91]:

Equation 2.20 Definition of sensitivity coefficient

$$S_{\xi} = \frac{\partial \ln R}{\partial \ln \xi} = \frac{\xi}{R}\frac{\partial R}{\partial \xi}$$

The higher the absolute value of the sensitivity coefficient $|S_{\xi}|$ is, the more dependent R is on ξ, the more accurate and more reliable the ξ deduced from fitting R will be. Figure 2.7A plots the sensitivity coefficients of the ratio $-V_{in}/V_{out}$ to the thermal conductivity of silicon κ_{Si} (the blue dots), the nominal thermal conductivity of the interface κ_{Int} (the red dots), and the laser spots radius r, denoted by $S_{\kappa(Si)}$, $S_{\kappa(Int)}$, and S_r, respectively. Note that in Equation 2.17, the pump beam radius w_0 and the probe beam radius w_1 are interchangeable with each other, thus there is no point studying the sensitivity to each of them separately. We define an effective beam radius r, where $r = \sqrt{w_0^2 + w_1^2}$, to lump them together.

As shown in Figure 2.7A, the sensitivity coefficient of the ratio to the thermal conductivity of silicon, $S_{\kappa(Si)}$, has a much higher absolute value over the whole time delay range (0.6 ~ 0.9), while the sensitivity coefficient of the ratio to the nominal thermal conductivity of the interface, $S_{\kappa(Int)}$, has a diminishing absolute value in the first 100 ps range, and then gradually ramps to 0.3. This fact indeed offers great advantage for our purpose, since among the two unknown parameters, the one we care about has higher absolute sensitivity coefficient, which means the fitting result is more reliable. To verify this statement in a more intuitive way, Figure 2.8A and B plot the comparison between the experimental data (red hollow dots) and the calculated results (black solid lines) with 20% less and 20% more of the thermal conductivity of the silicon deduced from Figure 2.6A, respectively, while all the other parameters remain unchanged. Figure 2.8C and D plot the comparisons between the experimental data and the calculated results with 20% less and 20% more of the interfacial thermal conductance, respectively. Conclusion can be easily drawn that the 'compromised' thermal conductivities of the silicon cause much more noticeable deviations of the calculated results from the experimental data, while the nominal thermal conductivity of the interface, even compromised at the same level as the former, do not cause obvious deviations of the calculated results.

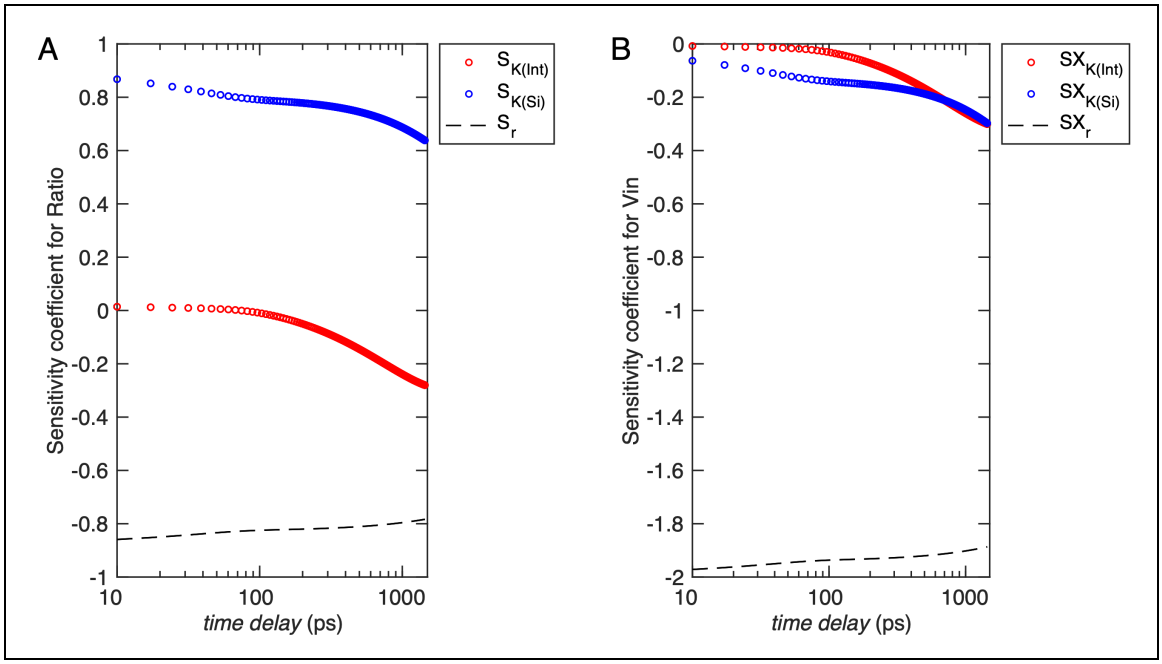

Figure 2.7 (A) The sensitivity coefficients of the ratio $-V_{in}/V_{out}$ to the thermal conductivity of silicon κ_{Si} (the blue dots), the nominal thermal conductivity of the interface κ_{Int} (the red dots), and the laser spots radius r, denoted by $S_{\kappa(Si)}$, $S_{\kappa(Int)}$, and S_r, respectively. (B) The sensitivity coefficients of the in-phase component V_{in} to the same three parameters.

As a side note here, the sentivity coefficient for $-V_{in}/V_{out}$ to the laser beam radius r has a large absolute value around 0.8 across the whole time delay range. This means that small experimental errors in determining the beam spot radii w_0 and w_1 may affect the calculation results. The smaller the beam spot size is, the higher temperature increase it will induce, and the stronger signal the lock-in amplifier will output. However, smaller beam size will bring higher uncertainty or experimental error in determining the spot size by experimnetal technique, such as knife edge measurement or laser beam profile sensor arrays. Therefore, as a trade-off, typical TDTR measurements use lens with small magification values below 10 and the pump and probe spot radii are on the order of 10 μm.

Figure 2.7A Figure2.7B plots the sensivity coefficient for V_{in} with respect to the three parameters. It has very similar behavior to the interficial nominal thermal conductivity as $-V_{in}/V_{out}$, but has a much lower absolute value to the thermal conductivity of the silicon (0 ~ 0.3). Besides, it also has more than two-times absolute values (above 1.9) to the laser spot size compared with the ratio. Such observations also support the claim made earlier for why we chose the ratio $-V_{in}/V_{out}$ as the target variable for fitting.

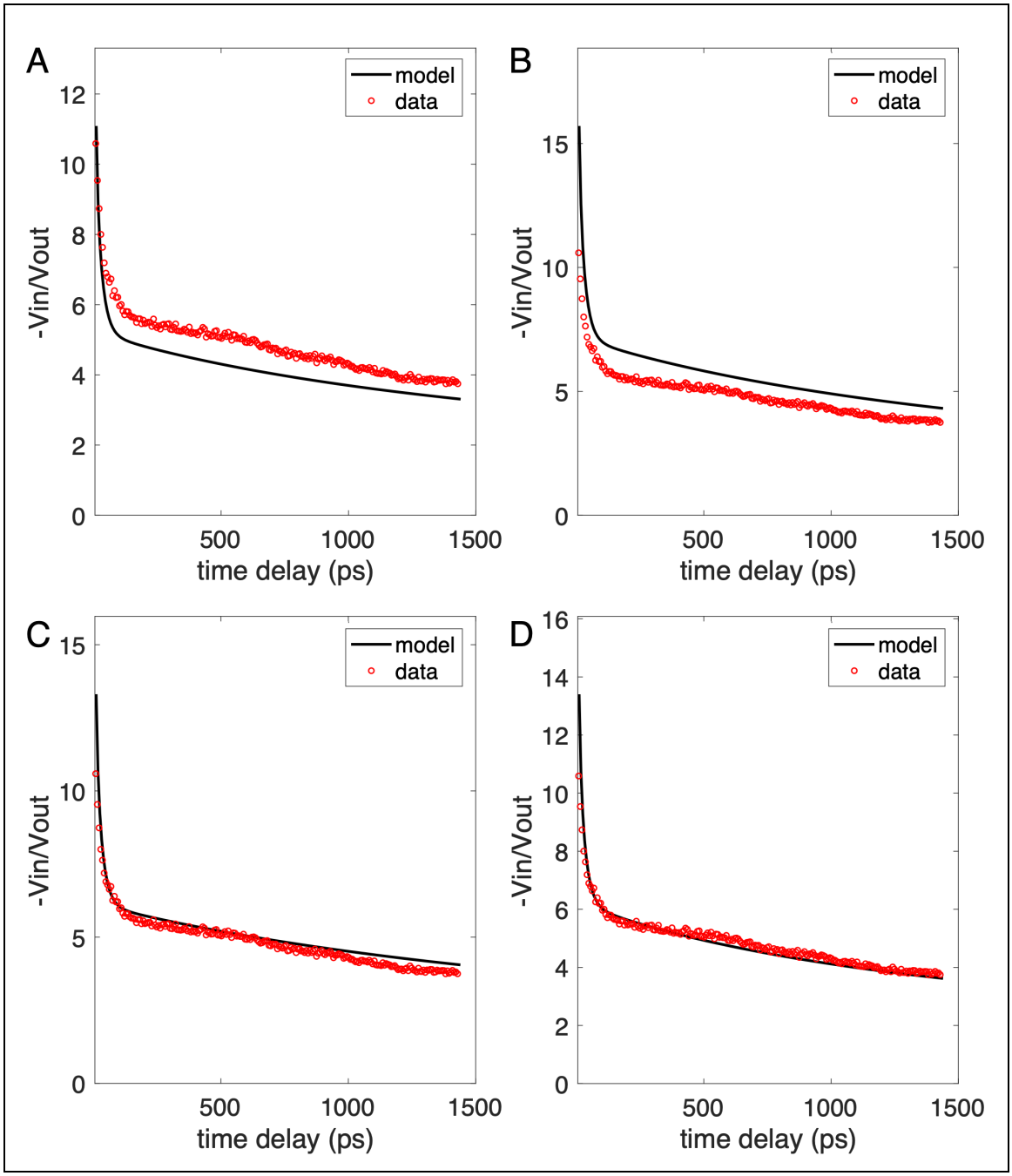

Figure 2.8 (A) and (B) plot the comparison between the experimental data (red hollow dots) and the calculated results (black solid lines) with 20% less and 20% more of the thermal conductivity of the silicon deduced from Figure 2.6A, respectively. (C) and (D) plot the comparison between the experimental data and the calculated results with 20% less and 20% more of the interfacial thermal conductance, respectively. The experimental data is the same as plotted in Figure 2.6A. In each of the four subplots, only one parameter is adjusted accordingly, while others remain the same as in Figure 2.6A. Conclusion can be easily drawn that this TDTR measurement has much higher sensitivity on the thermal conductivity of the silicon sample than the interfacial thermal conductance.

2.5 Additional comments on TDTR

So far, we have covered the experimental setup and theoretical framework for TDTR. We have also demonstrated sample results and analysis on the aluminum-on-silicon sample. The results for other samples measured with our setup are summarized in Table 2.3. Note that all the samples are deposited with a thin aluminum layer. Conclusions made in previous section also hold, such as no modulation-frequency-dependence of the fitted parameters. Results are averaged against the modulation frequency. These results are all in good agreement with other groups' work or literature.

Table 2.3 Summary for other samples

sample	Thermal conductivity ($\bar{\kappa}$, W·m^{-1}·K^{-1})	Variance ($\bar{\bar{\sigma}}_{\kappa}$)	Thermal conductance ($\bar{G}$, MW·m^{-2}·K^{-1})	Variance ($\bar{\bar{\sigma}}_{G}$)
Sapphire	36.0	1.7%	160.1	1.4%
Quartz	8.7	3.6%	147.6	0.8%
Glass	1.1	3.9%	125.2	1.0%

There are a few suggestions for a successful and reliable TDTR measurement. Firstly, the sample should have a smooth surface.

In addition to the standard TDTR configuration described above, there are a few variations based on TDTR, such as frequency-domain thermo-reflectance (FDTR)[92 – 114], time-resolved magneto-optic Kerr effect (TR-MOKE)[115 – 130], and asynchronous optical sampling (ASOPS)[131 – 144], which have significantly enriched the experimental technology stack that are suitable for micro- and nano-scale thermal transport studies. Below we illustrate one of the new ideas examined by extending the TDTR setup and theory described above.

2.6 Extension to FDTR

As its name implies, instead of varying the time delay between the pump and the probe in TDTR, frequency-domain thermo-reflectance (FDTR) collects and models the probe reflectance signal intensity versus the modulation frequency. The formal formulation of FDTR was first introduced by Schmidt et al in reference [93], where they described two experimental ways to implement FDTR. One is based on continuous wave (CW) lasers, and the other is based on the ultrafast femto-second laser system, same as TDTR. While the CW-laser-based implementation are much easier to achieve since it does not involve ultra-fast lasers and mechanical delay stage, the femtosecond-laser-based configuration offers new approaches for investigating non-equilibrium thermal transport and

characterizing transient material thermal properties that cannot be achieved with the CW-laser configuration, as discussed below.

The experimental setup for femtosecond-laser-based FDTR is exactly the same as that of TDTR as shown in Figure 2.1 and Figure 2.3, and the general theoretical framework from the perspective of the LTI system response dictated by Equations 2.9 ~ 2.11 also apply to FDTR. Note that in equation 2.10, the probe signal amplitude is not only a function of the delay time (τ) as in the first sub-equation, but also a function of the modulation frequency (ω_0) as in the second sub-equation, which are just Fourier-transform pairs. Therefore, by holding the delay stage at a fixed location, we can collect the reflectance signal and plot it against the modulation frequency. Typically, the modulation frequency is swept from 10 kHz to 20 MHz. Similar optimization process is performed by tuning the parameters of interest, such as the thermal conductivity of the substrate material and the interfacial thermal conductance for the typical aluminum-on-sample structure, to minimize the modified error function:

Equation 2.21 FDTR fitting error function

$$\mathbb{E}[\varphi] = \sum_{\omega_{0,exp}} \left|\varphi_{exp} - \varphi_{cal}\right|^2 \to 0$$

Here the target variable of fitting is chosen to be the phase delay of the reflectance signal [$\varphi = \arctan(V_{out}/V_{in})$]. Therefore, FDTR can essentially achieve the same results as TDTR.

Equipped with this new strategy, we have developed the FDTR into a time-resolved frequency-domain thermal diffusivity (Tr-FDTD) measurement technique. The fundamental idea behind this is that in the short time range (0 ~ 100 ps) right after the ultra-fast photoexcitation from the pump pulses, the material will undergo a fast-changing extreme non-equilibrium process (electron excitation, electron-electron interaction, electron-phonon interaction, etc.), thus the thermal properties of material system will also demonstrate certain dynamic process, i.e., in this ultra-fast regime, the transient thermal properties will be time-dependent. To characterize the material thermal properties at a specific time interval after the ultra-fast excitation, we utilize the extra flexibility of control offered by the femtosecond-laser-based FDTR. The experimental process is as follow: we fix the delay stage at delay time (τ_1), and by varying the modulation frequency (ω_0) and fitting the experimental data to the theoretical calculation via the optimization indicated by Equation 2.21, we can extract the transient thermal properties of the sample at τ_1. Then we adjust the delay time to τ_2, and repeat the process and get the transient properties at τ_2. By iterating the above step a few times at other delay time, we are able to reconstruct the time-dependence of thermal properties of the material under interrogation.

Here we utilize a simple material system to illustrate this technique. Consider a bulk aluminum sample as the system of interest, and the Green's function for 3-dimensional semi-infinite domain, that is, the impulse response to point source of unit energy released at $t_0 = 0$ at origin ($x_0 = y_0 = z_0 = 0$) is:

Equation 2.20 Green's function for 3-D semi-infinite domain

$$g(x,y,z,t) = \frac{1}{\rho c(4\pi\alpha t)^{\frac{3}{2}}} \exp\left(\frac{x^2+y^2+z^2}{-4\alpha t}\right)$$

Here α denotes the material thermal diffusivity, which is associated with the thermal conductivity through $\alpha = \frac{\kappa}{\rho c}$. The reason why we choose the thermal diffusivity, instead of the thermal conductivity, is that the thermal diffusivity measures the rate of heat transfer in a material, which is more appropriate to describe the dynamic non-equilibrium process that we are studying here. After two spatial convolutions with the Gaussian profiles of the heating source (the pump) and the probe, the system's response function, denoted as h in Equation 2.10, is:

Equation 2.21 Response function of 3-D semi-infinite domain

$$h(t) = \frac{\beta}{\rho c(4\pi)^{\frac{3}{2}}(\alpha t)^{\frac{1}{2}}} \cdot \frac{2}{{w_0}^2 + {w_1}^2 + 2\alpha t}$$

Combining Equations 2.21 with the LTI-framework described above in TDTR, we can now deduce the transient thermal diffusivity of bulk aluminum at a specific delay time τ. As mentioned in equation 2.21, we use the phase of the reflectance signal as the target variable of fitting. Figure 2.9A plots the experimental data as a function of the modulation frequency (25 kHz ~ 20 MHz), and the delay time (-10 ps ~ 10 ps). Note the negative delay time refers to the fact that the probe pulses come before the corresponding pump pulses, and due to the accumulation effect (the effect induced by a pump pulse cannot die away before the next pump pulse comes, i.e., the system cannot restore to its unperturbed state before the next perturbation comes.), at negative delay time the probe pulses is effectively probing the effect induced by the previous pump pulses. Therefore, the negative delay time $-\tau$ is equivalent to the positive delay time $T - \tau$, where is the interval between two pump pulses (12.5 ns). Therefore, the accumulation effect allows us to measure the system's response at much longer delay time range ($\sim T$).

Figure 2.9B plots the comparisons between the theoretical calculation (solid lines) and experimental data (hollow dots) for 3 delay-time cases, 10 ps (right after the excitation), 1.44 ns (maximum delay of the delay stage), and the 12.49 ns (-10 ps, right before the excitation). We first perform the fitting of the 12.49-ns case and deduce that the thermal diffusivity of the bulk aluminum sample is 1.04×10^{-4} m^2/s, which agrees well with results reported in literature ($0.8 \times 10^{-4} \sim 1.2 \times 10^{-4}$ m^2/s).[144 – 146] Since at such long delay time, the transient thermal diffusivity should be close to the results measured by steady-state methods. We anticipate that the thermal diffusivity shows its time-dependence in the delay time range within 10 pico-second after the pump pulse excitation, since the electron-phonon interaction time scale is on the order of 1 ps. Then we plot the theoretical calculation using this deduced thermal diffusivity for the other two cases as well. As shown in Figure 2.9B, the calculation agrees well with the experimental data for the 1.44-ns case,

which indicates that at this delay time, the transient thermal diffusivity has already decreased to its steady-state value. On the other hand, there is some noticeable discrepancy between the theoretical calculation and the experimental data for the 10-ps case, which suggests that at the early stage of the restoring process after the ultra-fast photoexcitation, the transient thermal diffusivity may deviate from the steady-state value.

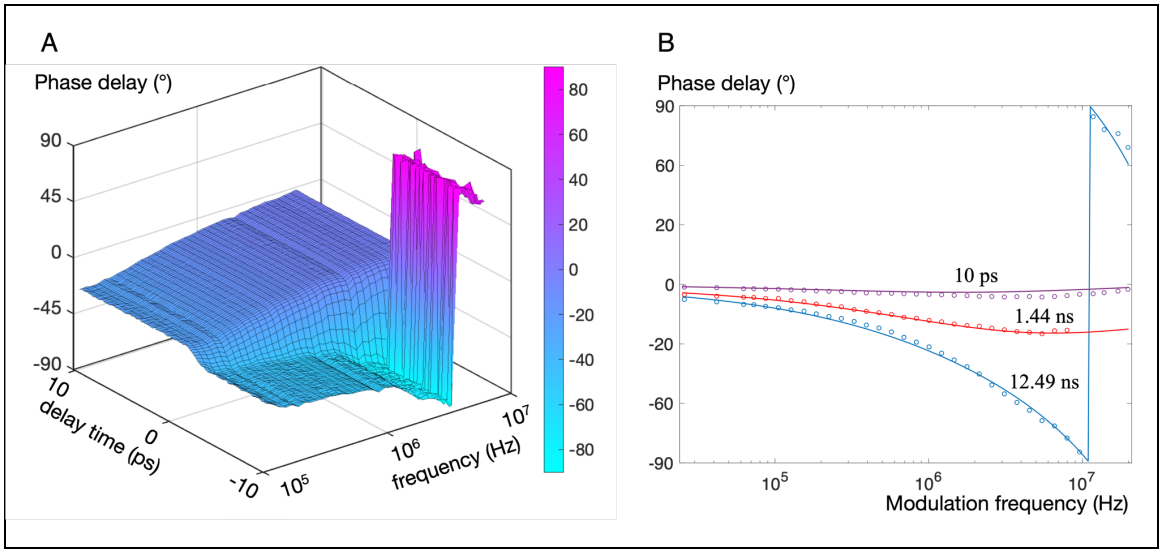

Figure 2.9 (A) Experimental data of time-resolved frequency domain thermo-reflectance on bulk aluminum sample, phase delay as a function of the modulation frequency (25 kHz ~ 20 MHz), and the delay time (-10 ps ~ 10 ps). (B) Comparisons between the theoretical calculation (solid lines) and experimental data (hollow dots) for 3 delay-time cases, 10 ps (purple), 1.44 ns (red), and the 12.49 ns (blue).

The good agreement between the calculation and experiment for the long delay time cases (1.44 ns and 12.49 ns) validate the concept of time-resolved frequency domain thermo-reflectance. However, measuring the quasi-steady-state thermal diffusivity at long delay time isn't interesting, since the fundamental thermal energy carriers, electrons and phonons have almost reached a quasi-equilibrium state where the ultra-fast dynamic process has already diminished. When a pump pulse comes at the sample surface, the electrons inside of the material system capture the photon energy and get excited instantaneously (10 ~ 100 femtosecond). At the early stage, the excited electrons have a much higher nominal temperature (a few thousand kelvin), which means they have high kinetic energy to diffuse away from the illuminated area, collide with other unexcited electrons (electron-electron interactions) and phonons (electron-phonon interactions), transferring the thermal energy from the high-temperature electron-subsystem to the low-temperature phonon-subsystem, as well as spatially transporting mass and energy, until the electron-subsystem and phonon-subsystem reach an equilibrium, that is to say, the material system has a unified temperature. This electron-phonon interaction process usually happens at a time scale of a few picoseconds. Then only the long-time scale (on the order of nanosecond to microsecond) spatial thermal transport continues to take place.

We are particularly interested in the thermal transport behavior before the electron sub-system and the phonon-subsystem reach the equilibrium, since in the beginning the majority of the thermal carriers will be the electrons, which have an effective mass smaller than that of phonons by a few orders of magnitude and diffuse much faster than phonons. Therefore, we anticipate the nominal thermal diffusivity of the material at the early stage will be noticeable higher than the steady-state value. From Figure 2.9B, the phase delay for short delay time (10 ps) across the whole frequency range is very close to 0, therefore, we use the inverse of the phase delay ($1/\varphi$) as the target variable of fitting to study the early-stage behavior.

Figure 2.10A and B plot the inverse of the phase delay versus the modulation frequency from 25 kHz to 20 MHz, for delay time at 0.4 ps and 4 ps, respectively. The experimental data (denoted as the hollow red dots) can be fitted well by the theoretical calculation (denoted as the solid blue lines). The deduced transient apparent thermal diffusivity for these two cases is 18.81×10^{-4} m^2/s at 0.4 ps, which is 18.1 times larger than the steady-state value measured at long delay time (1.04×10^{-4} m^2/s), and 10.37×10^{-4} m^2/s at 4 ps, 10 times larger than the steady-state value. The yellow solid lines and orange solid lines plot the theoretical calculations with 20% less and 20% more of the deduced thermal diffusivity value, respectively, indicating high sensitivities for the thermal diffusivity in these measurements.

To quantitively illustrate the time-dependence of the transient thermal diffusivity measured in Tr-FDTR, we here define an enhancement coefficient of the thermal diffusivity (c_α) as:

Equation 2.22 Definition for the enhancement coefficient

$$\alpha(t) = c_\alpha \cdot \alpha(t \to +\infty) = c_\alpha \cdot \alpha_{steady-state}$$

Here we use the thermal diffusivity measured at -10 ps, which is right before the delay time 0 and equivalent to delay time of 12.49 ns, sufficient to approximate the steady-state value defined in Equation 2.22. In Figure 2.10C, the time-dependent enhancement coefficient of the transient thermal diffusivity of the bulk aluminum is plotted versus the delay time from 0.1 ps up to 12.49 ns. The enhancement coefficient remains close to 1 from long delay time all the way down to around a few tens of pico-seconds. As the delay time continues to go down, the enhancement coefficient starts to drastically increase and reaches a maximum around 20 at 0.1 ps, which is the smallest delay time value we have measured. This behavior validates the presumption made earlier: when the ultra-fast pump pulse comes, the high-density free electrons in the bulk aluminum sample captures the photon and absorb the photon energy instantaneously, thus the local electron-subsystem has a much higher transient temperature, while the phonon sub-system remains unheated. The hot electrons start to diffuse to surrounding areas, while there is a low density of excited phonons. Therefore, at this early stage (0 ~ 1 ps), the hot electrons are the major thermal carriers in the extreme non-equilibrium, and the nominal thermal diffusivity reflects exclusively the diffusive capability of the hot electrons. The electrons have significantly smaller effective mass and much lower specific heat compared with phonons, thus the 'thermal inertia' of the electron-subsystem is small and the thermal diffusivity is high. As

the electrons diffuse away and collide with the lattice, through electron-phonon interactions, the excessive thermal energy in the electron sub-system is transferred to the phonon sub-system, and eventually an equilibrium is established between these two sub-systems. At this stage, the phonons start to contribute more to the thermal transport, and due to its sluggish kinetic characteristics and large specific heat, the 'thermal inertia' of the thermal transport process increases by a few orders of magnitude. Phenomenologically, the nominal thermal diffusivity is drastically decreased. When the equilibrium between the two sub-systems is fully established, the thermal transport process is equivalent to that of a slowly-heating case without involving ultra-fast photoexcitation, thus the thermal diffusivity measured at this stage is equal to the steady-state result. This conclusion agrees well with the well-known two-temperature model in the research area of ultra-fast laser diagnosis and manufacturing.[147 – 153]

Similar results have been reported in reference [154], but their work shows that the maximum transient thermal diffusivity of a metallic sample can be as large as 100 times larger than the steady-state value, while in our experiments, the largest enhancement coefficient is around 20. This discrepancy comes from the fact that the femto-second laser pulses used in our experiments have a full-width-at-half-maximum (FWHM) of ~ 400 fs after the objective lens, thus measured transient thermal diffusivity at delay time τ is actually an averaged value in a small time range around τ ($\tau \pm \Delta\tau$). The direct consequence of this fact is that the measured transient thermal diffusivity right after the delay time zero, which is supposed to be 100 times larger than the steady-state value, actually is 'contaminated' by the steady-state values in the range from -200 fs to 0 fs which corresponds to the range from 12.48 ns to 12.5 ns from the previous pump pulse. Therefore, the highest value for the transient thermal diffusivity is compromised. Mathematically, this causes the assumption made earlier in the theoretical framework to be compromised, since at a short delay time right after the delay time 0, the laser pulses cannot be mathematically expressed as a train of delta functions as in Equations 2.5 and 2.7. Figure 2.10D plots the experimentally collected phase delay data versus the delay time, which illustrates the effect of the finite laser pulse duration. The plot of the phase delay versus the delay time should converge to 0 at delay time 0 ($\tau = 0$) based on Equation 2.10 for lasers that have an ideal pulse duration of 0 and can be truly represented by a delta-function in time domain is indicated by the gray dashed line in Figure 2.10 D. The finite duration width of the laser pulses blurs the true signal, and as a result, causes an underestimation for the transient thermal diffusivity in the theoretical calculation. Compressing the laser pulses with a pair of prisms used in reference [154] can help to minimize this unwanted effect, and replacing the delta function in Equations 2.5 and 2.7 with a Gaussian function to represent the laser pulse profile may also increase the accuracy of the model and the fitting. However, both two methods add significant complexity to either the experimental instrumentation or the theoretical calculation. Therefore, we did not pursue the efforts toward this direction in this work.

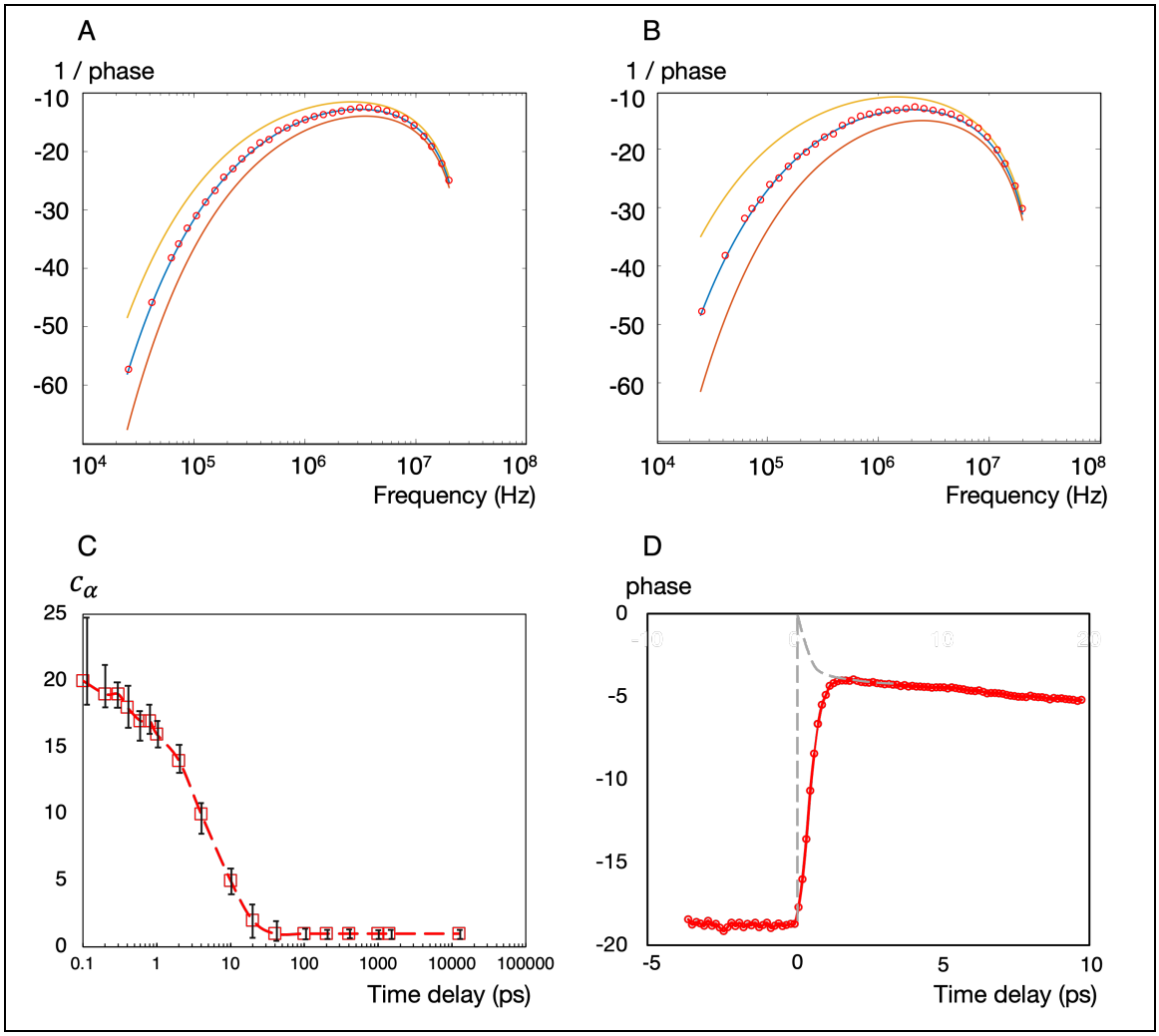

Figure 2.10 (A) and (B) plot the inverse of the phase delay versus the modulation frequency from 25 kHz to 20 MHz, for delay time at 0.4 ps and 4 ps, respectively. The experimental data (denoted as the hollow red dots) can be fitted well by the theoretical calculation (denoted as the solid blue lines). The deduced transient thermal diffusivity for these two cases is 18.81× 10^{-4} m^2/s at 0.4 ps, which is 18.1 times larger than the steady-state value measured at long delay time (1.04 × 10^{-4} m^2/s), and 10.37 × 10^{-4} m^2/s at 4 ps, 10 times larger than the steady-state value. The yellow solid lines and orange solid lines plot the theoretical calculations with 20% less and 20% more of the deduced thermal diffusivity value, respectively, indicating high sensitivities for the thermal diffusivity in these measurements. (C) plots the time-dependent enhancement coefficient of the transient thermal diffusivity of the bulk aluminum versus the delay time from 0.1 ps up to 12.49 ns. The enhancement coefficient remains close to 1 from long delay time all the way down to around a few tens of pico-seconds. As the delay time continues to go down, the enhancement coefficient starts to drastically increase and reaches a maximum around 20 at 0.1 ps. The error bars are evaluated based on measurements on different sample locations. The red dashed line serves as a view-guide and is not a fitted line. (D) plots the experimentally collected phase delay data (hollow red dots) with fitting (red solid line) versus the delay time, which illustrates the effect of the finite laser pulse duration. The plot for lasers that have an ideal pulse duration of 0 is indicated by the gray dashed line.

2.7 Summary

In this chapter, we have discussed the experimental instrumentation and theoretical framework for out customized time-domain thermo-reflectance (TDTR) setup and have demonstrated some of the measurement results using the developed TDTR technique to measure the material thermal conductivity and the interfacial thermal conductance. Sensitivities of the measurement have been discussed in detail. We have also covered the innovative technique, time-resolved frequency-domain thermo-reflectance (Tr-FDTR) developed based on the TDTR framework, and have shown its application in characterizing the transient thermal properties of materials in the process of ultra-fast laser heating. These powerful techniques not only facilitate future studies in the research area of nanoscale thermal transport, but also the foundation for the near-field ultra-fast optical pump-probe microscopy technique which will be discussed in the next chapter.

This page is left black intentionally.

3 Thermal Transport Study via Near-field Ultra-fast Optical Microscopy

As mentioned in Chapter 1, the second phase of this research work is to pursue the integration of ultra-high temporal and spatial resolution and develop a comprehensive optical diagnostics platform that builds up new avenues for studying nanoscale transient heat transfer and energy transport processes.

In this chapter, we describe the extension of the far field ultra-fast optical pump-probe microscopy technique with integrated near-field scanning optical microscopy (NSOM) in detail, which has been introduced and briefly discussed in Chapter 1. We start with a detailed description of the experimental instrumentation, and then discuss some of the measurement results on semiconducting materials. Applications of this novel and powerful thermal measurement tool will be demonstrated.

3.1 Experimental Instrumentation

The accessibility of the near field is realized by introducing the atomic force microscopy (AFM) instrument into the ultra-fast optical pump-probe microscopy platform discussed in the previous chapter, specifically in the configuration of scattering near-field scanning optical microscopy (s-NSOM). Figure 3.1 provides a schematic illustration for the instrumentation of the near-field in-situ ultra-fast optical pump-probe microscopy, which essentially is very similar to the optical delivery system that is built for the far field measurement previously described in Figure 2.1. Here we briefly recapitulate the overall implementation design, as well as the integration with the scattering near-field optical microscopy.

The 800-nm femto-second laser beam coming from the Ti:Sapphire oscillator (Tsunami, from Spectra Physics) is split by the 9:1 beam splitter (BS, from CVI Laser Optics) into two branches: the major branch (90%) serves as the pump beam, and is frequency-doubled via second harmonic generation (SHG) by a non-linear crystal (NLC), beta Barium borate (BBO, from Eksma Optics), into pulses with 400-nm wavelength (represented as the blue light ray), and then is amplitude-modulated by an electro-optic modulator (EOM, from Conoptics); the minor branch (10%) serves as the probe beam, and passes through a mechanical delay stage (DS, from Thorlabs), and then merges its beam path with the pump beam. Both the pump beam and the probe beam are sent into the optical delivery system inside of the optical chamber (denoted as the gray box) of the customized atomic force microscopy instrument (from Molecular Vista). The pump beam and the probe beam are then loosely focused by a parabolic mirror (PM) towards the apex of the AFM tip. The sample is mounted on a 3-axis piezo-stage (S). During normal AFM operation, the stage is automatically adjusting the z-axis position such that the tip apex is right in contact

with the sample surface (contact mode) or several nanometers above the sample surface (tapping mode). The probe light backscattered from the tip apex and the sample surface is then collected and collimated by the parabolic mirror and redirected to a fast-response avalanche photodiode (APD, from Thorlabs) by a beam splitter (BS). A long-pass filter (LPF) is put in between the BS and the APD to prevent the scattered pump light from contaminating the signal, and a lens (L) is used to focus the reflected beam into the active sensing area of the APD. The voltage signal from the APD is sent to a lock-in amplifier for signal demodulation, referenced at a frequency determined by the controller embedded in the Molecular Vista AFM system, which also acts as the function generator for control the modulation at the EOM on the pump beam. Note that the controller can generate functions with multiple frequencies simultaneously via different channels, and depending on the actual experimental configuration, the modulation frequency of the EOM may be different from the demodulation reference frequency of the lock-in amplifier. Part of the reason is that the back-scattered signal contains both the far-field reflectance and the near-field reflectance, and the far-field signal can be a few orders of magnitude larger than the near-field signal. To extract the near field signal from the overwhelmingly dominant far-field signal, special techniques (modulation-demodulation schemes) are needed. We will discuss this topic in detail later in this chapter. The controller also controls the modulation at the acoustic-optical modulator (AOM) on the probe beam, which is only utilized in PiFM measurement. In the SNOM configuration the AOM is temporarily removed. We will cover its functionality when we discuss the PiFM measurement later in this chapter.

Both the AFM measurement and the NSOM measurement is extremely sensitive to environmental vibrations, which may cause significant noise in the measured results, and even worse, may cause irreversible damage to the AFM tip and the sample. To alleviate this threat as much as possible, the AFM system, including the optical chamber, is mounted on an active vibration isolator to cancel the high-frequency environmental vibrations that cannot be efficiently damped by the floated optical table. Besides, an acoustic enclosure (denoted as the hollow gray rectangle) is utilized to encapsulate the whole AFM system, which can effectively screen vibrations from the ambient environment (the air). The core part of the AFM measurement, including the sample mounting platform, the AFM tip, and its mounting (the AFM head) can be encapsulated by an environmental chamber (EC, denoted as the gray dashed rectangle), which supports various experimental conditions, such as vacuum and specific-gas filling environment. An objective lens (OL) and an imaging system are integrated on a motorized movable mechanical arm (not shown in Figure 3.1) for online monitoring through the optical window (denoted as the light-yellow thin slab) on the EC lid.

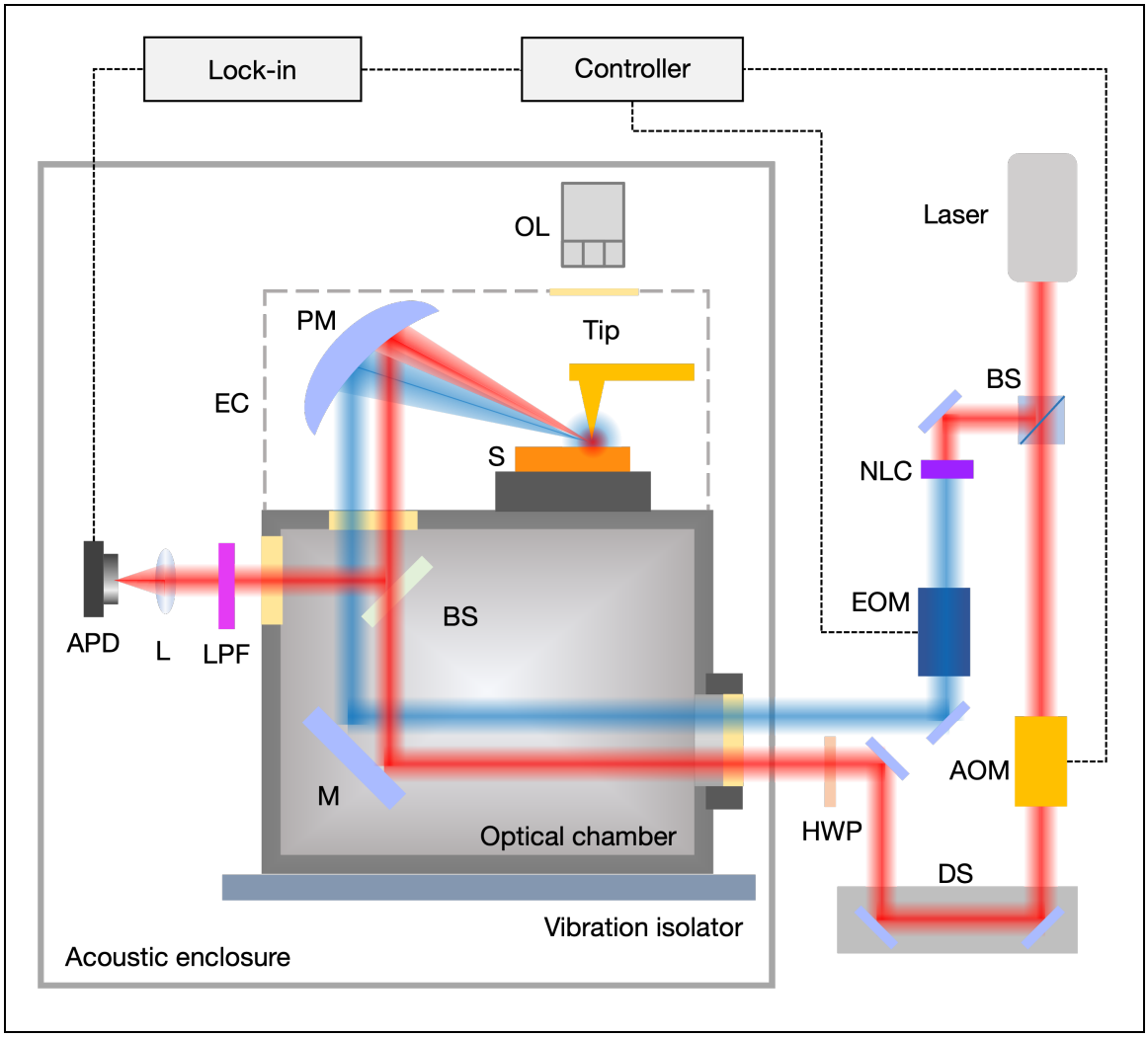

Figure 3.1 Schematic of the near-field in-situ ultra-fast optical pump-probe microscopy. The 800-nm femto-second laser beam is split by the beam splitter (BS) into two branches: the major branch (the pump) is frequency-doubled by a non-linear crystal (NLC), and then is amplitude-modulated by an electro-optic modulator (EOM); the minor branch (the probe) passes through a mechanical delay stage (DS), and then merges its beam path with the pump beam. Both are sent into the optical chamber of the atomic force microscopy instrument, and then loosely focused by a parabolic mirror (PM) towards the apex of the AFM tip. The sample is mounted on a 3-axis piezo-stage (S). The probe light backscattered from the tip apex and the sample surface is then collected by the PM and redirected to an avalanche photodiode (APD) by a beam splitter (BS). A long-pass filter (LPF) is put in between the BS and the APD, and a lens (L) is used to focus the reflected beam into the APD. The voltage signal from the APD is sent to a lock-in amplifier for signal demodulation, referenced at a frequency determined by the controller, which also controls the modulation at the EOM on the pump beam. The controller also controls the modulation at the acoustic-optical modulator (AOM) on the probe beam, which is included in PiFM measurement. The AFM system is mounted on an active vibration isolator and encapsulated by an acoustic enclosure. An environmental chamber (EC) can support various experimental conditions. An objective lens (OL) and an imaging system is integrated for online monitoring. A half-wave plate (HWP) for the probe beam is placed outside of the acoustic enclosure to allow polarization control and maximize the near field coupling with the AFM tip.

Note that for clarity, the schematic illustration in Figure 3.1 leaves out various optical or mechanical components that are included in real instrumentation, such mirror pairs for fine optical alignment, and half-wave plate and polarized beam splitter for continuous laser power attenuation. Compared with far field optical delivery system, the most noticeable difference is that in the near-field setup the separation of the scattered backward-traveling probe beam from the forward-traveling incident probe beam is done via simply redirecting by a non-polarizing beam splitter. This design indeed causes a decent amount of probe beam intensity loss in both forward and backward paths. Compared with the far-field configuration where a combination of the quarter wave plate and the polarizing beam splitter is used to maximize the probe light collection efficiency, the non-polarizing beam splitter will cause the collection efficiency decrease by more than 75%. The reason why we cannot use the same design as the far-field setup for probe light redirection here is that the quarter wave plate would cause the probe light at the tip apex to be circularly polarized. The near field coupling efficiency is highly dependent on the polarization of the incident light, and achieves its maximum when the light has vertical polarization and aligns with the vertical axis of the tip-gap-sample system. To maximize the near field efficiency in our measurement, more accurately to maximize the ratio of the near-field signal over the far-field signal, we sacrifice the probe signal intensities, which is compensated by using the APD. In addition, to allow the best match of the probe light polarization with the tip apex, a half-wave plate (HWP) for the 800-nm probe beam is placed outside of the acoustic enclosure to facilitate fine tuning of the probe light polarization. The effect of the probe light polarization will be discussed later in this chapter.

Figure 3.2A shows the modification on the far field optical beam path to extend to the pump-probe technique to the scattering near-field optical microscopy instrument. A flip mirror is placed right after the harmonic combinator (HC), originally where the pump beam path and the probe beam path merge. In far-field measurement, the flip mirror is flipped down so it will not interfere with the far-field setup, and in near-field measurement, the flip mirror is flipped up to redirect both the pump beam and the probe beam to another mirror (M) towards the s-NSOM instrument. Figure 3.2B shows the optical beam path before entering the acoustic enclosure: the harmonic separator transmits the pump beam and reflects the probe beam, to allow the probe beam to pass the acoustic-optical modulator (AOM), the linear polarizer (P) and the half-wave plate (HWP) without affecting the pump beam. The AOM is only used in PiFM measurement, and in s-NSOM measurement it is temporarily removed. The linear polarizer sanitizes the polarization of the probe beam, and the half-wave plate is used to fine-tune the alignment of the probe light polarization along the axis of the AFM tip. The pump beam and the probe beam merge again at the harmonic combinator (HC) before entering the acoustic enclosure.

Figure 3.3A shows the exterior look of the acoustic enclosure, and the structural layout inside of the acoustic enclosure is presented in Figure 3.3B. The optical chamber is mounted on an active vibration isolator, and the environmental chamber is placed on top of the optical chamber. An objective lens and a CCD camera system are installed on the motorized mechanical arm to allow online monitoring and imaging. The optical beam path is also included. Figure 3.3C demonstrates the interior of the optical chamber, and the structural layout and optical beam path inside of the environmental chamber is shown in

Figure 3.3D. The parabolic mirror loosely focuses the pump beam and the probe beam on to the apex of the AFM tip. The AFM tip is too small to be visually observed in Figure 3.3D, and the arrow denotes its approximate location.

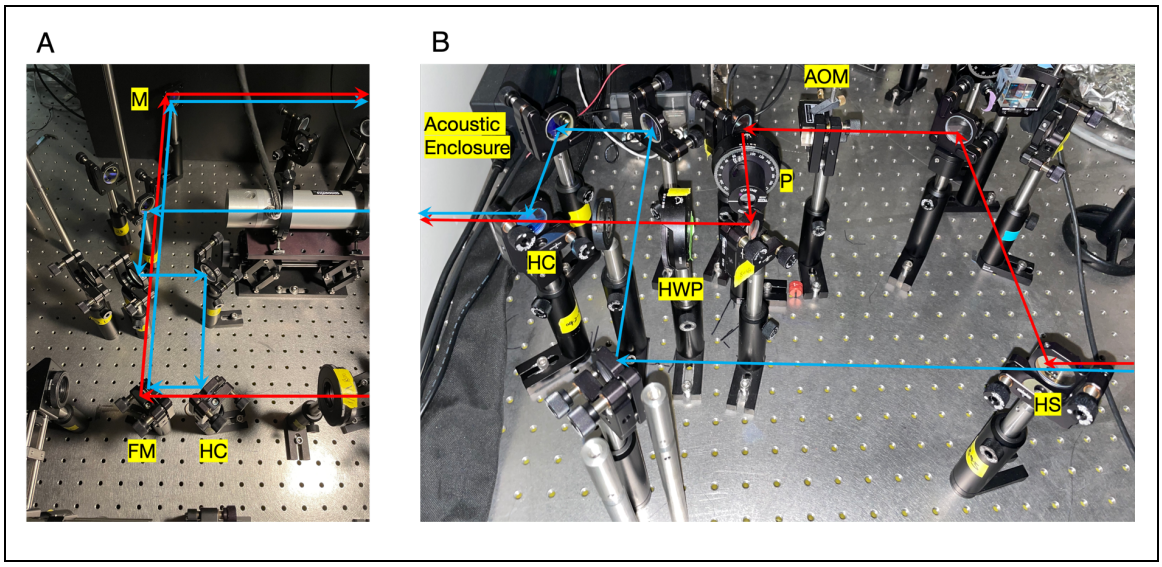

Figure 3.2 (A) The modification on the far field optical beam path to extend to the pump-probe technique to the SNOM microscopy instrument. A flip mirror is placed right after the harmonic combinator (HC). In far-field measurement, the flip mirror is flipped down so it will not interfere with the far-field setup, and in near-field measurement, the flip mirror is flipped up to redirect both the pump beam and the probe beam to another mirror (M) towards the s-NSOM instrument. (B) The optical beam path before entering the acoustic enclosure. The harmonic separator transmits the pump beam and reflects the probe beam, to allow the probe beam to pass the acoustic-optical modulator (AOM), the linear polarizer (P) and the half-wave plate (HWP) without affecting the pump beam. The AOM is only used in PiFM measurement, and in s-NSOM measurement it is temporarily removed. The linear polarizer sanitizes the polarization of the probe beam, and the half-wave plate is used to fine-tune the alignment of the probe light polarization along the axis of the AFM tip. The pump beam and the probe beam merge again at the harmonic combinator (HC) before entering the acoustic enclosure.

So far, we have provided an overview of the design and implementation of the near-field in-situ ultra-fast optical pump-probe microscopy. As a high-level comparison with the far-field measurement, with the near-field setup, the optical pump and probe beams will couple to the AFM tip and the enhanced localized near-field signal will be utilized to investigate the ultra-fast kinetics and dynamics in the material system under investigation. In general, the LTI-system perspective theoretical framework and the experimental techniques introduced in Chapter 2, including the time-domain and the frequency-domain methods, can still apply here. In the work, we focus on the time-domain technique: each of the modulated pump pulses causes an instantaneous excitation (~100 fs) at the illuminated area and a following relatively slow restoring process (~100 ps). Such processes can be monitored by characterizing the sample material optical property change. By varying the optical path difference between the pump and the probe, we can reconstruct the dynamic process in time domain.

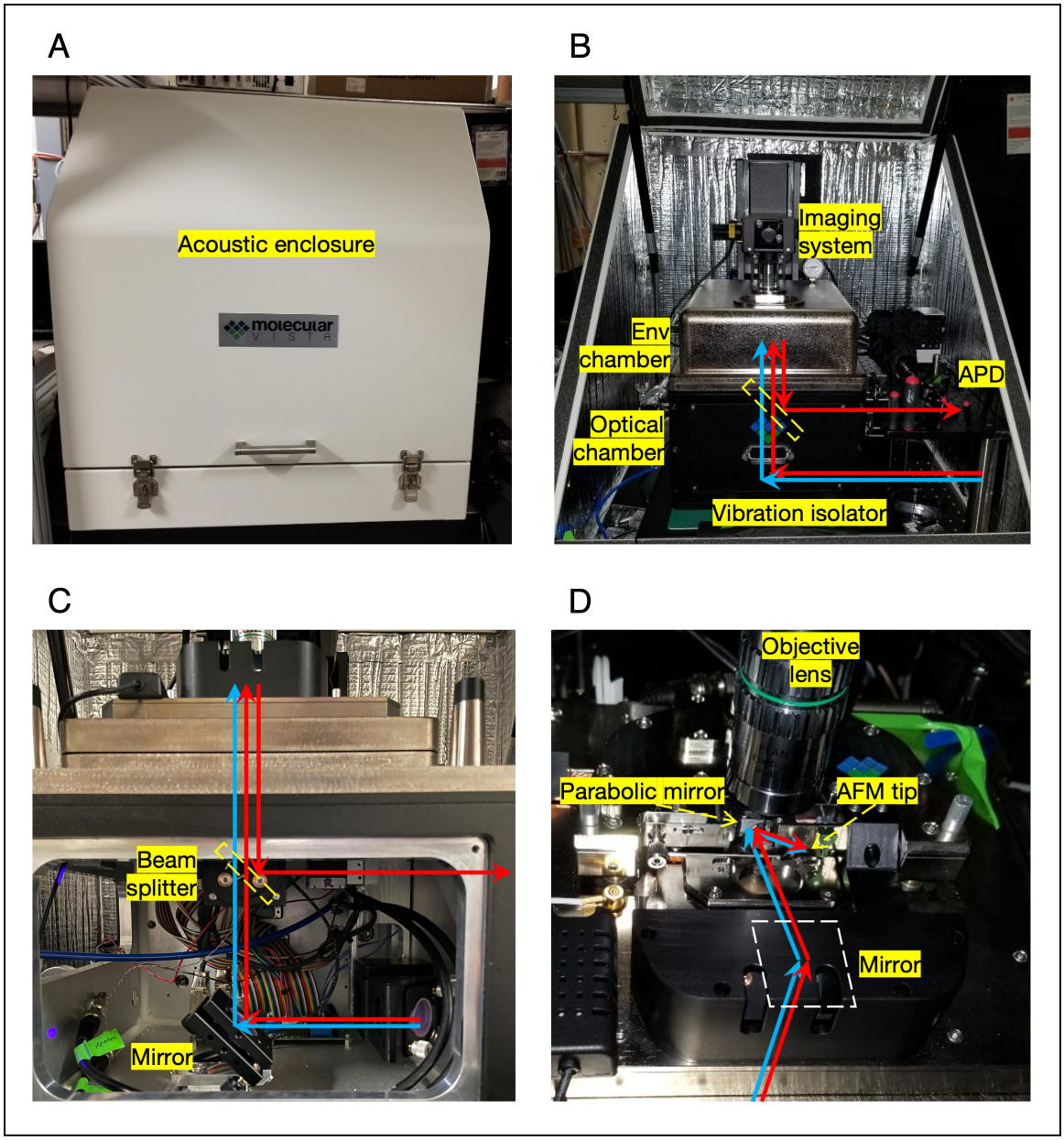

Figure 3.3 (A) The exterior look of the acoustic enclosure. (B) The structural layout inside the acoustic enclosure. The optical chamber is mounted on an active vibration isolator, and the environmental chamber is placed on top of the optical chamber. An objective lens and a CCD camera system are installed on the motorized mechanical arm to allow online monitoring and imaging. The optical beam path is also included. (C) The interior of the optical chamber. (D) The structural layout and optical beam path inside of the environmental chamber. The parabolic mirror loosely focuses the pump beam and the probe beam on to the apex of the AFM tip. The AFM tip is too small to be visually observed, and the arrow denotes its approximate location.

In the next section, we will use the measurement of a silicon nanowire as an example to illustrate the experimental details of the near-field in-situ ultra-fast optical pump-probe

microscopy, and discuss the major results.

3.2 Measurement of Silicon Nanowire

In this section, we exclusively focus on a silicon nanowire sample. Silicon nanowires fabricated by etching process are diffused in solvent and then drop-cast on a quartz substrate. The lateral length of the nanowire ranges from 50 nm to 1 μm, and the axial length is typically a few micrometers.

3.2.1 Scattering-based Pump-probe Microscopy

We firstly verify that the ultra-fast optical pump-probe microscopy can work properly on the AFM instrument. In other words, the ultra-fast dynamics induced by the pump pulses must cause the intensity of the collected probe signal to have resolvable changes through certain mechanism, similar to a far-field optical pump-probe measurement such as transient absorption and/or reflection measurements. Here the priority is given to the pump-probe effect, even though the signal may mostly come from the far field, since we need to locate the delay time 0 and have backbone reference before we move towards the near field measurement.

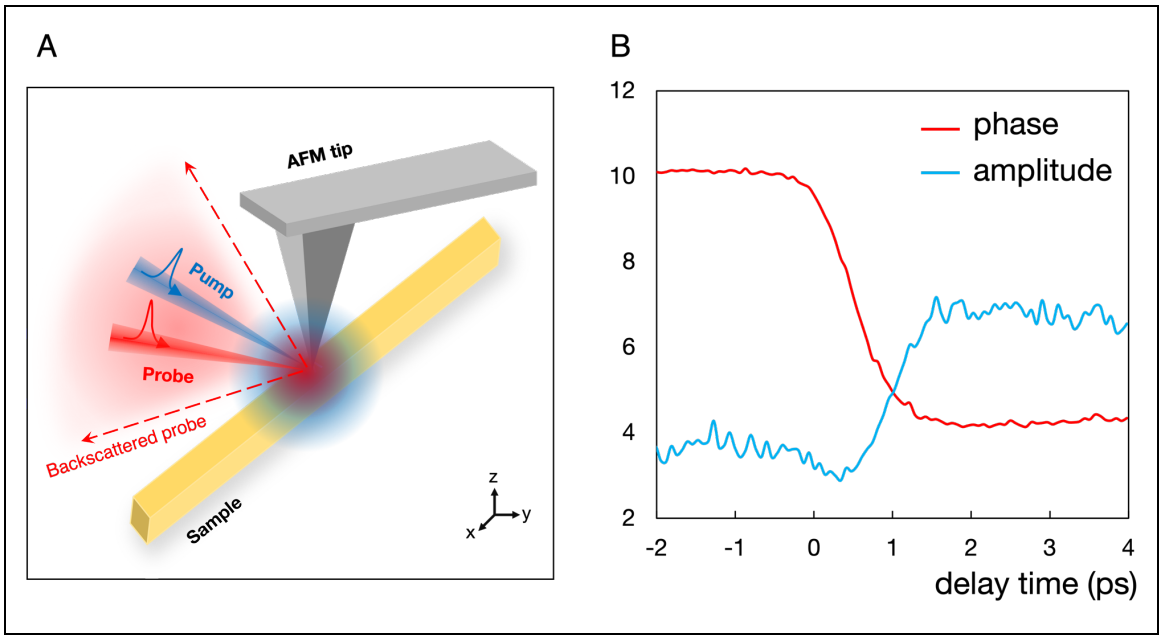

Figure 3.4 (A) Schematic of the experimental configuration for the near-field in-situ ultra-fast optical pump-probe microscopy measurement of a silicon nanowire. Both the pump beam and the probe beam are focused to the AFM tip apex, which is engaged at around 10 nm above the sample surface. With the presence of the AFM tip, some portion of the probe light can be scattered back towards the parabolic mirror, which collects

and collimates the scattered probe light and deliver it to the downstream photodetector. (B) The amplitude (denoted as the solid line) and the phase (denoted as the red line) of the demodulated probe signal in the narrow time range across the delay time 0. The phase starts to rapidly decrease and reaches a plateau after 1 ps, while the amplitude undergoes a small decrease from 0 to 0.3 ps, then starts to increase and reaches a plateau at 1.5 ps.

Figure 3.4A demonstrates the experimental configuration for the near-field in-situ ultra-fast optical pump-probe microscopy measurement of a silicon nanowire. Both the pump beam and the probe beam are focused to the AFM tip apex, which is engaged at around 10 nm above the sample surface. Since the incident beam comes at an oblique angle to the sample surface, without the AFM tip, the reflected beam will not travel back along the same incident path towards the parabolic mirror, thus there will not be any probe light reaching the downstream photodetector. With the presence of the AFM tip, some portion of the probe light can be scattered back towards the parabolic mirror, but the scattered light has a much wider angular distribution than the incident probe beam. Due to the finite size of the parabolic mirror, only a small portion of the scattered probe light will be collected and collimated by the parabolic mirror. This is the major reason that the raw intensity of the probe beam collected by the photodetector is much lower than our far-field measurement where both the pump beam and the probe beam co-axially illuminate the sample surface perpendicularly. Fortunately, with the high gain of the avalanche photo diode (APD) used as the photodetector in the near-field measurement, we have successfully produced similar results regarding the ultra-fast dynamics as the far-field pump-probe measurement. We modulate the amplitude of the pump beam at frequency of 100 kHz (arbitrarily chosen), and demodulate the collected probe signal at the same frequency. Figure 3.4B plots the amplitude (denoted as the solid line) and the phase (denoted as the red line) of the demodulated probe signal in the narrow time range across the delay time 0. The phase starts to rapidly decrease and reaches a plateau after 1 ps, while the amplitude undergoes a small decrease from 0 to 0.3 ps, then starts to increase and reaches a plateau at 1.5 ps.

3.2.2 Extracting Near-field Signal

So far, we have verified and validated the feasibility to do the ultra-fast optical pump-probe measurement with the scattering-based configuration embedded in the s-NSOM instrument. With this progress, we are now ready to focus on the near-field measurement. As in all types of apertureless near-field optical microscopy measurement, the most significant challenge here is to extract the near-field signal from the overwhelmingly dominant far-field signal. Figure 3.5 shows the optical views from the CCD camera installed on the AFM system when the pump beam (A) and the probe beam (B) are focused onto the AFM tip apex. The AFM tip is located beneath the cantilever and cannot be captured in the top view. The parabolic mirror loosely focuses the two beams into a spot with radius on the order of 1 millimeter, which is 5 orders of magnitude larger than the characteristic size of the AFM tip apex. Figure 3.6 A shows an SEM image of the Platinum-coated AFM tip (from Molecular Vista) used in the near field measurement. The metallic

coating can significantly improve the coupling efficiency of the optical energy into the apex-gap-sample nano-system through plasmonic resonance in the metallic layer such that the near field optical intensity is enhanced.[199 – 201] The lateral dimension of the tip apex is around 50 ~ 70 nm, which sets the spatial resolution limit for the near field measurement. This sharp tip apex structure can strongly magnify the optical field intensity in the close vicinity of the tip apex due to the antenna effect, typically up to a few tens of nanometers.[155] Figure 3.6B shows an optical image of the AFM tip mounted on the AFM head and floated at 5 μm above the sample surface (not engaged), taken by scanning the parabolic mirror to steer the probe beam. Note that the tip apex cannot be resolved in the optical image since its size is well below the Abbe diffraction limit.

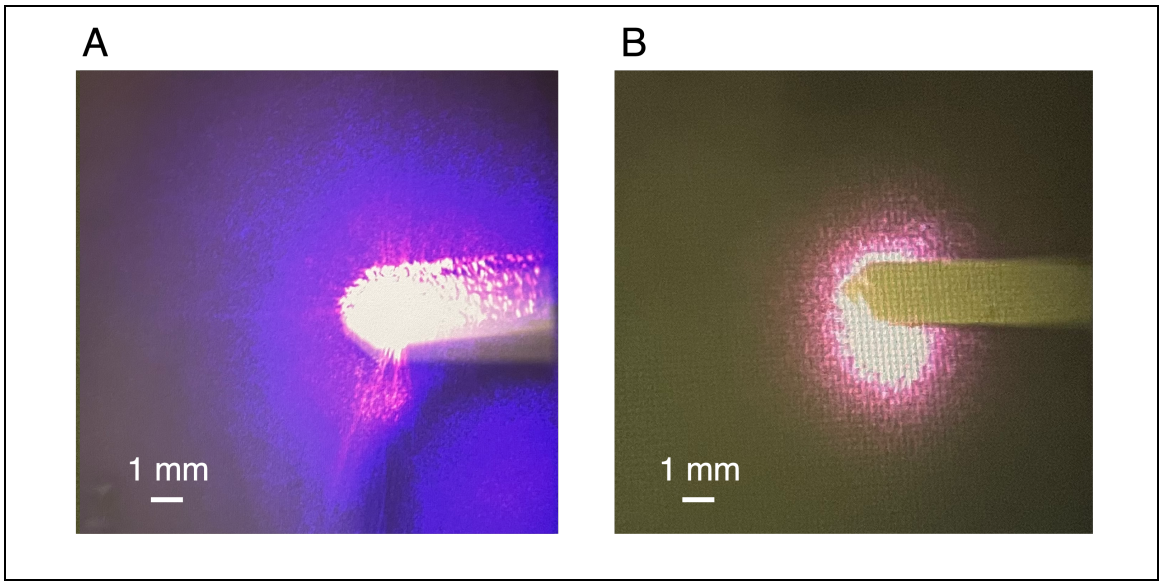

Figure 3.5 Top views from the CCD camera showing the pump beam (A) and the probe beam (B) are focused onto the AFM tip apex. The AFM tip is beneath the AFM tip cantilever and cannot be captured in the top view. The parabolic mirror loosely focuses the two beams into a spot with a radius on the order of 1 millimeter, which is 5 orders of magnitude larger than the characteristic size of the AFM tip apex (~60 nm).

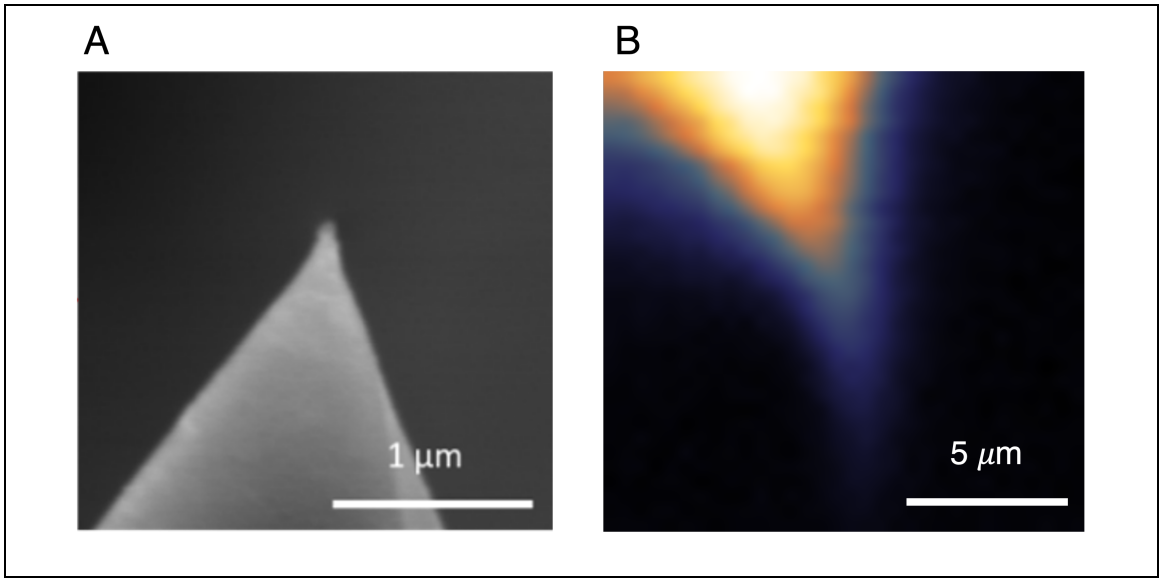

Figure 3.6 (A) An SEM image of the Platinum-coated AFM tip for plasmonic enhancement of the near field optical intensity. The lateral dimension of the tip apex is around 50 ~ 70 nm. (B) An optical image of the AFM tip mounted on the AFM head and floated at 5 μm above the sample surface (not engaged), taken by programmatically scanning the parabolic mirror to stir the probe beam. Note that the tip apex cannot be resolved here since its size is well below the Abbe diffraction limit.

The pump light can excite the sample via light-matter interaction both in the far field and in the near field, and the far-field probe light measures the far-field pump effect while the small portion of the probe light that couples to the tip-gap-sample nano-system measures the near-field pump effect. Since both the near-field and the far-field pump effect are modulated simultaneously by the same sinusoidal function, we cannot solely rely on the pump modulation to extract the near-field signal. One way to solve this problem is to take advantage of the tapping motion of the AFM tip in the non-contact mode: the driven vibration of the tip causes a periodic change in the gap distance between the tip apex and the sample surface. From the theory of classical electromagnetics, unlike in the Fraunhofer regime (far field) where the amplitude of the electromagnetic (EM) field falls off as $1/r$, in the Fresnel regime (near field), the amplitude of the EM field decays as $1/r^2$, thus the energy intensity of the near-field EM drops as $1/r^4$.[86, 155] Under tapping mode, the tip apex is engaged at 10 nm above the sample surface (preset by the AFM manufacturers), and the amplitude of the tapping motion of the tip is 2 nm, that is, the gap between the tip apex and the sample surface is periodically changing between 8 nm and 12 nm. As illustrated in Figure 3.7, the near-field signal changes drastically as the gap distance varies. This indeed provides another amplitude modulation mechanism on the near field signal, and thus facilitate the separation of the near-field signal from the dominant far-field background signal.

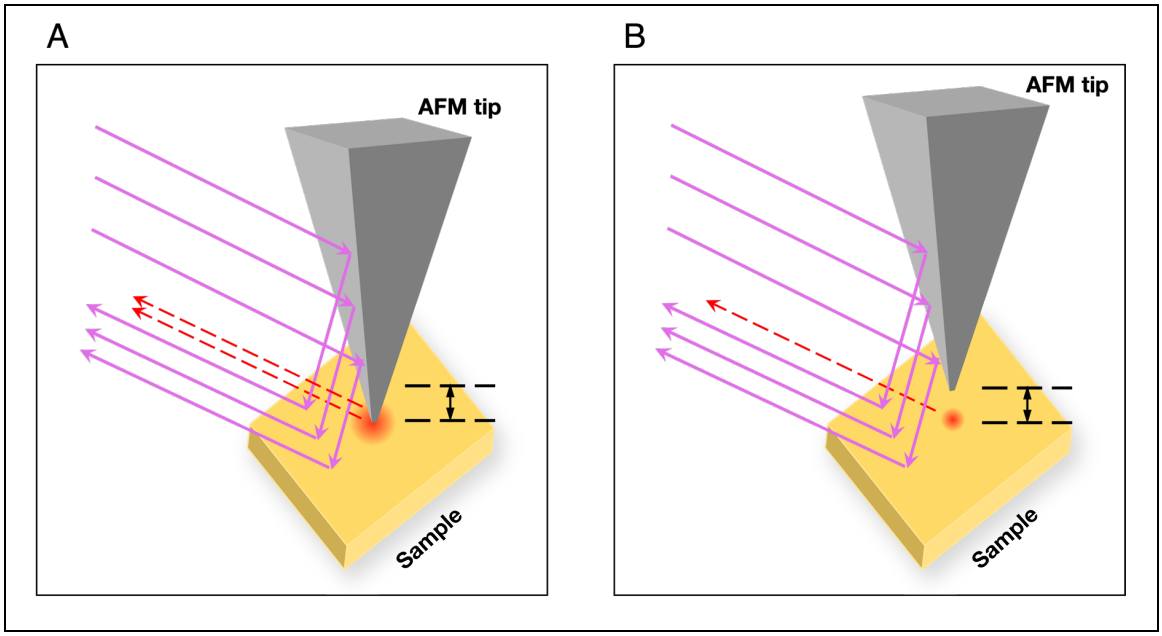

Figure 3.7 Illustration of the gap-distance dependence of the near-field signal. For clarity purpose, the pump light is not included here, and the far-field probe light is denoted as the purple solid line. When the tip apex is close to the sample surface (A), the near-field effect is greatly enhanced, and more near-field probe light is scattered out from the gap (denoted as the red dashed lines), and when the gap distance is large (B), there is less probe light scattered out. Note that the drawing is qualitative and only for illustration purpose, and quantitative analysis will be discussed later.

The tapping motion is determined by the resonance frequencies of the AFM tip cantilever. The AFM tip cantilevers used in our experiments have two resonance frequencies at around 265 kHz (f_1) and 1670 kHz (f_2), respectively. The strategy here is to couple the pump excitation with the resonance vibration of the AFM tip cantilever such that the near-field pump effect can be in 'resonance' with the gap distance modulation imposed by the tapping of the tip. Mathematically, the gap distance can be expressed as:

Equation 3.1 Harmonic decomposition of the gap distance

$$d(t) = d_0 + \sum_{k=1}^{\infty} \left(A_k e^{-i(2\pi k f_1 t + \varphi_{1,k})} + B_k e^{-i(2\pi k f_2 t + \varphi_{2,k})} \right)$$

Here d_0 is the equilibrium gap distance. That is, the periodic change in gap distance can be decomposed to infinite series of harmonics of the two resonance frequencies ($k = 1$) and their higher orders ($k = 2, 3, 4 \ldots$). Note that the mixture of the two groups of components, such as $e^{-i[2\pi(f_1+f_2)t]}$ and $e^{-i[2\pi(f_1-f_2)t]}$, is ignored here due to the high quality factor (Q-factor) of the cantilever resonator.

Finding a good detection scheme is not trivial, and indeed has been one of the toughest challenges encountered in this work. A good choice of the combination of the pump modulation frequency (set to the EOM) and the probe signal demodulation frequency (set

to the lock-in amplifier) should exclude the far-field signal as much as possible, while maintaining a measurable intensity of the near-field signal. We first try to set the pump modulation frequency to the lower resonance frequency (f_1) or its higher orders, and demodulate the probe-scattering signal at the same frequency as the pump modulation. We fix the delay stage position at certain delay time, and move the piezo stage in the horizontal plane, while collecting the demodulated pump-probe signal intensities at each location. Therefore, the snapshot of the 2D mapping of the pump-probe signal in the measured region of the sample surface can be recorded. Figure 3.8A shows the topography of the measured region on the sample surface, and the resolved silicon nanowire has a width of around 350 nm. Figure 3.8 B and C show the pump-probe signal mappings for the same region at delay time at -1 ps and 1 ps, respectively, where the pump beam is modulated at f_1 and the probe signal is demodulated at f_1 as well. Despite the noticeable difference between the two images, which indicates resolvable pump effect, the structure of the nanowire can hardly be identified in the pump-probe signal mappings (the red dashed lines indicate the edge of the nanowire). The interference pattern observed in both images is a result of the incident probe light interaction with the reflected probe light in the far field; the tip scatters and effectively modulates the far-field electromagnetic field with f_1, and this f_1 component is eventually extracted by the lock-in demodulation. The pump effect here is purely due to the far-field pump induced changes in the probe reflectance, thus the intensity of the 'stripes' increases. This indicates that coupling to the f_1 component is not sufficient to extract the near-field signal from the far-field background, since the f_1 component of the tip tapping motion also effectively modulates the far-field signal. Similar results are obtained when the pump beam is modulated at $2f_1$ and the probe signal is demodulated at $2f_1$, as shown in Figure 3.8D and E. Figure 3.8 F and G plot the results of the measurement where the pump beam is modulated at $3f_1$ and the probe signal is demodulated at $3f_1$, at -1 ps and 1 ps, respectively. Under such detection scheme, the far-field signal is significantly suppressed compared with the former two cases, and we do observe obvious signal changes on the nanowire due to the pump excitation, even though the signal distribution does not follow the topography exactly.

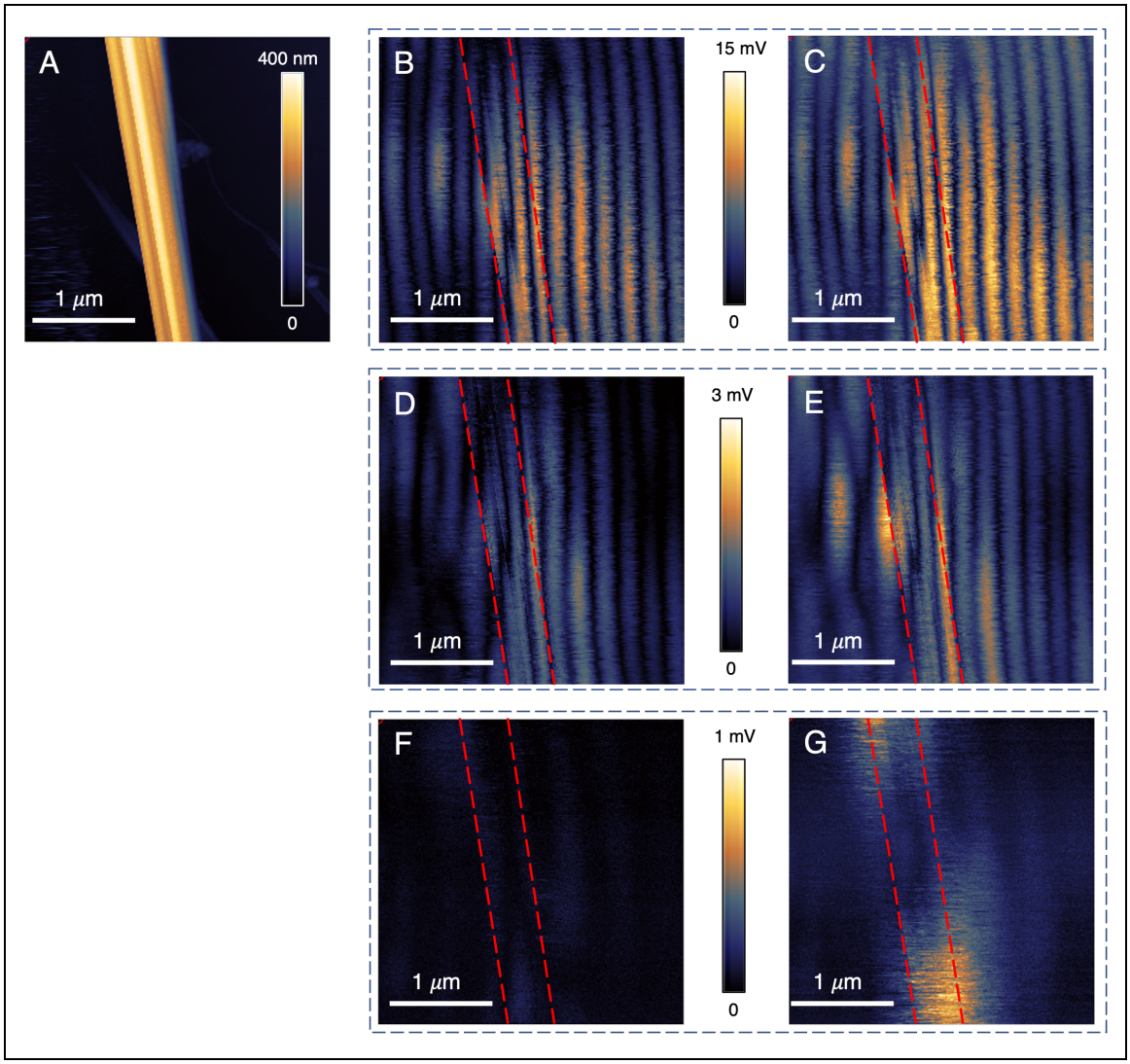

Figure 3.8 (A) The topography of the silicon nanowire under investigation. It has a width of ~350 nm. (B) and C show the pump-probe signal mappings for the same region at delay time at -1 ps and 1 ps, respectively, where the pump beam is modulated at f_1 and the probe signal is demodulated at f_1 as well. Despite the noticeable difference between the two images, which indicates resolvable pump effect, the structure of the nanowire can hardly be identified in the pump-probe signal mappings (the red dashed lines indicate the edge of the nanowire). This indicates that coupling to the f_1 component is not sufficient to extract the near-field signal from the far-field background, since the f_1 component of the tip tapping motion also effectively modulates the far-field signal. (D) and (E) plot similar results that are obtained when the pump beam is modulated at $2f_1$ and the probe signal is demodulated at $2f_1$. (F) and (G) plot the results of the measurement where the pump beam is modulated at $3f_1$ and the probe signal is demodulated at $3f_1$, at -1 ps and 1 ps, respectively. Under such detection scheme, the far-field signal is significantly suppressed compared with the former two cases, and obvious signal changes on the nanowire due to the pump excitation is resolved, even though the signal distribution does not follow the geometry exactly. Note that (B) and (C) are plotted with the same scale indicated by the scale bar between them, so do (D) and (E), (F) and (G). As the harmonic order used in the detection scheme increases, the absolute signal intensity also decreases.

It is reasonable to infer from Figure 3.8 that higher-order harmonics are likely to be better at extracting the near-field signal from the large far-field background. Figures 3.9B, C and D show the pump-probe signal mappings for the same region at delay time at -1 ps, 0.5 ps, and 1 ps, respectively, where the pump beam is modulated at $4f_1$ and the probe signal is demodulated at $4f_1$. Compared with the $3f_1$ case shown in Figure 3.8, the pump-probe signal distribution demonstrates a much better correspondence of the nanowire topography shown in Figure 3.9A. and the edge of the nanowire can clearly be identified in the pump-probe signal mapping images captured right after the delay time 0. Measurements using higher-order harmonics above $4f_1$ show similar results. However, as the harmonic order used in the detection scheme increases, the absolute signal intensity also decreases, as shown in Figure 3.8. Besides, the pump-probe signal profile measured with such detection scheme, for example in the $4f_1$ case, has a width of around 1 μm, which is approximately double of the nanowire width, as shown in Figure 3.9H which plots the topography (red solid line) and the pump-probe signal (green solid line) along the white dashed line in Figure 3.9D.

Another approach is to utilize the mixture terms of the two modulations here, the pump intensity modulation imposed by the EOM, and the gap-distance modulation imposed by the tapping motion of the AFM tip. Denote the modulation frequency of the former as f_a, and the latter as f_b, then the signal may have measurable components at $f_a - f_b$ and $f_a + f_b$. A natural idea of the detection scheme is to modulate the pump beam at nf_1, and demodulate the probe signal at $(n-1)f_1$ or $(n+1)f_1$. Figure 3.9E, F, and G show one example using this strategy, where the pump beam is modulated at $4f_1$, and the probe signal is demodulated at $3f_1$, at delay time of -1 ps, 0.5 ps, and 1 ps, respectively. The pump-probe signal distribution is more confined within the vicinity of the nanowire itself, compared with Figures 3.9B, C and D. Figure 3.9I plots the topography (red solid line) and the pump-probe signal (green solid line) along the white dashed line in Figure 3.9G, indicating that the pump-probe signal are sensitive to the edges of the nanowire. However, the pump-induced probe signal intensity change is still more obvious in the region off the nanowire surface. The results with demodulation at $5f_1$ are similar. We did not observe better results with the value of n other than 4. From the comparison between the two cases in the Figure 3.9, it is clear that detection scheme based on the frequency mixture term results in much lower absolute signal intensity.

Our best results are obtained by coupling the pump-probe effect to the second resonance frequency (f_2) of the AFM tip cantilever. Unlike the previous results, detection scheme using the first order harmonic of the resonance frequency f_2 is sufficient to significantly suppress the far-field signal and extract the near-field signal. This implies that the f_2-component of the AFM tip's tapping motion has an appropriate amplitude value (B_1 in Equation 3.1) such that the f_2-component motion is not too drastic to measurably modulate the far-field signal, but it is sufficient to modulate the gap distance between the tip apex and the sample surface to effectively modulate the near-field signal enhancement. From the perspective of the signal processing, the signal-to-noise ratio in lock-in-based signal amplification and demodulation used in TRTR and related experiments is dependent on the modulation-demodulation frequency, and typically the higher the frequency is, the higher the signal-to-noise ratio will be, which is why we need an EOM in TDTR

measurements to achieve high-frequency modulation rather than using a mechanical chopper or an AOM.

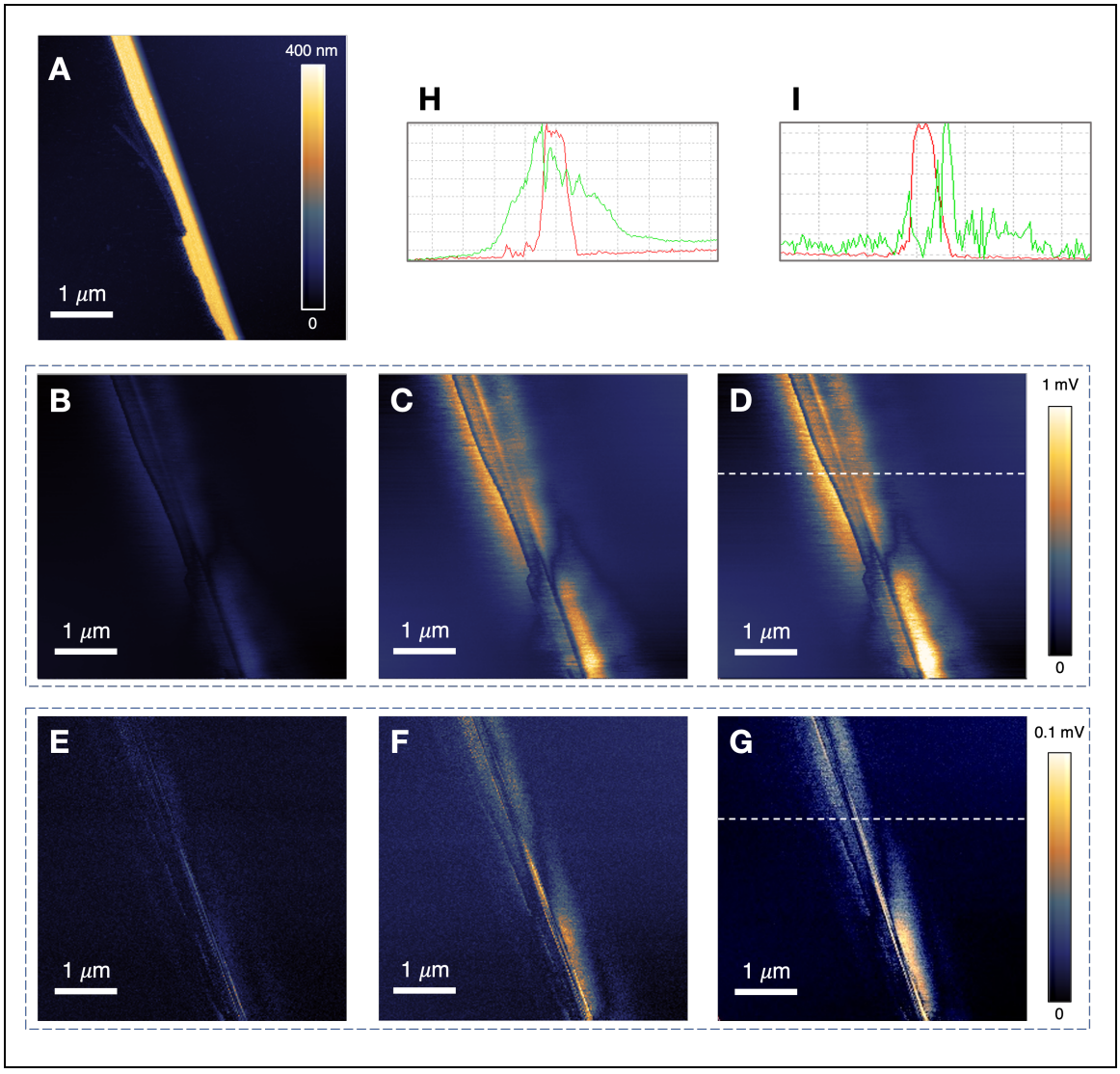

Figure 3.9 (A) The topography of the nanowire under investigation. (B), (C) and (D) show the pump-probe signal mappings at delay time at -1 ps, 0.5 ps, and 1 ps, respectively, where the pump beam is modulated at $4f_1$ and the probe signal is demodulated at $4f_1$. The pump-probe signal distribution demonstrates a much better correspondence to the nanowire topography, compared with the $3f_1$ case shown in Figure 3.8, and the edge of the nanowire can clearly be identified in the pump-probe signal mapping images captured right after the delay time 0. (E), (F), and (G) show the results where the pump beam is modulated at $4f_1$, and the probe signal is demodulated at $3f_1$. The pump-probe signal distribution is more confined within the vicinity of the nanowire itself. (H) and (G) plot the topography (red solid lines) and the pump-probe signal (green solid lines) along the white dashed line in (D) and (G), respectively. Note that (B), (C) and (D) are plotted with the same scale as indicated by the scale bar on the right, so do (E), (F) and (G).

Figure 3.10 shows one example of the measurement results where the pump beam is modulated at f_2 and the probe signal is demodulated at f_2 as well. Figure 3.10A shows the topography mapping in the 1-by-1-μm area, indicating both the width and the height of the silicon nanowire are around 200 nm. Figures 3.10B, C and D show the pump-probe signal mappings at delay time at -1 ps, 0.5 ps, and 1 ps, respectively. The pump-probe signal distribution demonstrates a strong correspondence to the nanowire topography, except that the edges of the nanowire are blurred. We will discuss the fact shortly. The drastic change from B to C and D as the delay time changes indicates strong pump-probe effect in the near field. This is a milestone in this research work since we have successfully realized the combination of the ultra-high temporal resolution (on the order of 100 fs) and ultra-high spatial resolution (on the order of 10 ns) of the developed experimental instrumentation.

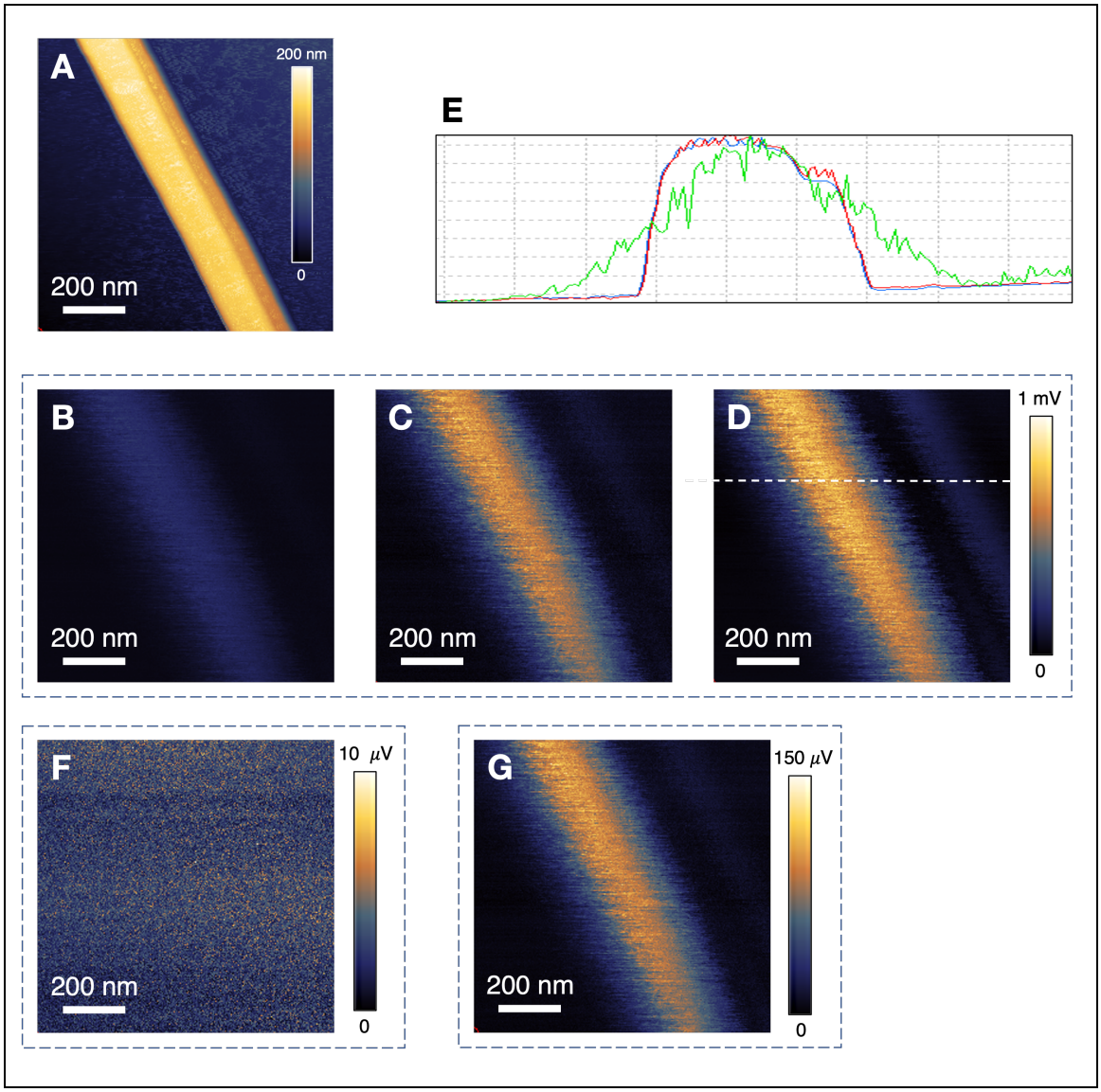

Figure 3.10 (A) The topography of the nanowire under investigation, which has a characteristic length in the cross-section of 200 nm. (B), (C) and (D) show the pump-probe signal mappings at delay time at -1 ps, 0.5

ps, and 1 ps, respectively, where the pump beam is modulated at f_2 and the probe signal is demodulated at f_2. The pump-probe signal distribution demonstrates a strong correspondence to the nanowire topography, with a slight residual near the edge, up to 50 nm out of the sample surface. Note that (B), (C) and (D) are plotted with the same scale as indicated by the scale bar on the right. (E) plots the topography (red solid line and blue line, forward and backward, respectively) and the pump-probe signal (green solid line) along the white dashed line in (D). (F) and (G) show the probe signal mapping images at -1 ps, without and with the pump excitation, respectively. Note that (B) and (G) are the same mapping image but with different scales.

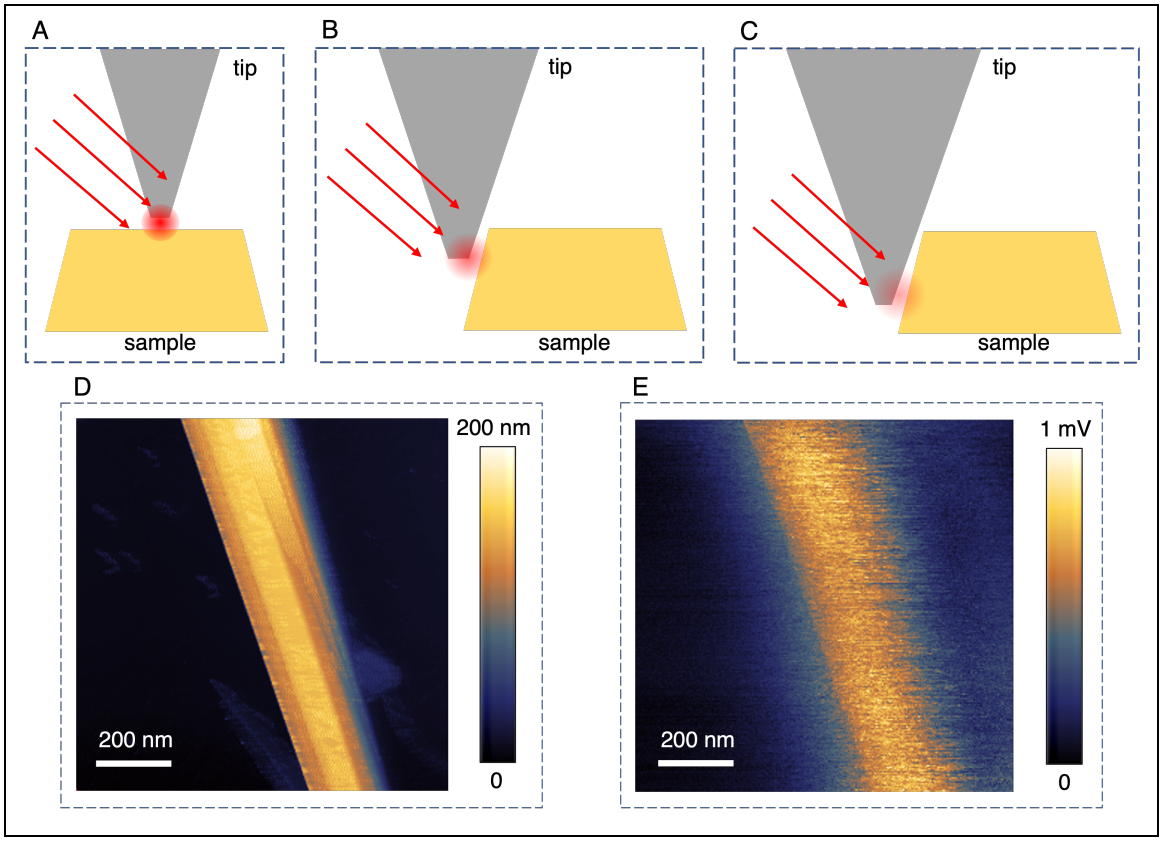

Figure 3.11 (A) When the tip apex is engaged above the sample surface, the signal measures the localized region beneath the tip, and the resolution is equal to the size of the tip apex. (B) When the tip moves onto the slope of the edge, it also measures the region near the side of the tip apex, which worsens the spatial resolution and causes the edge in the pump-probe signal mapping blurred. (C) When the tip moves off the nanowire but are still close to it, the plasmonic resonance on the side of the tip apex still interacts with the local region on the slope of the sample edge, which induces measurable signal. (D) and (E) plot the topography and pump-probe signal mapping at 1 ps for a nanowire with a sharper edge, respectively, showing that the edge-blurring issue illustrated in (B) and (C) has less effect on sharper edges.

Figure 3.10E plots the topography (red and blue lines) and the pump-probe signal (green solid line) along the white dashed line in (D). The pump-probe signal profile has a slight residual near the edge, up to 50 nm out of the sample surface. Note that the red and blue solid lines are the topography profiles collected when the tip travels forward and backward, respectively, and the good agreement between them indicates the sample scanning speed is appropriate to allow the tip to follow the surface topography well. The

topography profile shows that the edges of the nanowire are not as sharp as they appear in the topography (Figure 3.10A). Each edge spans around 30 nm, and this is one of the reasons why the nanowire looks wider in the pump-probe signal mappings than in the topography. The signal in the vicinity out of the nanowire can be explained by the finite size of the AFM tip. As shown in Figure 3.11, when the tip apex is engaged above the sample surface (A), the signal measures the localized region beneath the tip, and the resolution is equal to the size of the tip apex; as the tip moves onto the slope of the edge (B), it also measures the region near the side of the tip apex, which worsens the spatial resolution and causes the edge in the pump-probe signal mapping blurred; when the tip moves off the nanowire but are still close to it, the plasmonic resonance on the side of the tip apex still interacts with the local region on the slope of the sample edge, which induces measurable signal. The edge-blurring issue explained in Figure 3.11B can be alleviated if the nanowire has a sharper edge, as shown in Figures 3.11D and E. However, the unwanted signal in the vicinity of the nanowire illustrated in Figure 3.11C is difficult to minimize, unless the tip apex is very long and thin. Therefore, the broadening of the pump-probe signal along the tip moving direction (technically the moving direction of the sample) is an artifact resulting from the geometry of the AFM tip apex, which unfortunately is not avoidable.

Figures 3.10F and G show the probe signal mapping images at -1 ps, without and with the pump excitation, respectively. Note that Figures 3.10B and G are the same mapping image but with different scales. As we discussed in the previous chapter, the measurable signal at negative delay time (the probe pulse comes before the corresponding pump pulse) indicates that the dynamic process induced by the last pump pulse has not died away before the next pump pulse comes, that is, each pump pulse causes a response that lasts longer than the laser pulse interval, 12.5 ns. At -1 ps, with the pump we observe similar pump-probe signal distribution in the mapping image shown in Figure 3.10G (with low intensities), and as we will see later, this is due to the thermal expansion of the nanowire; without the pump as shown in Figure 3.10F, there is no signal across the 2D mapping, which verifies that the signal that we observe here are purely pump-probe effect. This validates the detection scheme, setting both modulation and demodulation at f_2, is an excellent choice for extracting the near-field pump-probe signal from the overwhelmingly strong background signal, which contains the far-field signal and the DC term induced by the sample surface structure. The latter refers to the fact that certain structural irregularity on the sample surface can enhance the resonance of the tip tapping Figure 3.12B and C show the measurement results on the same sample area with modulation at $4f_1$ and demodulation at $3f_1$, at -1 ps, without and with the pump, respectively. Although there is some slight intensity increase on the upper part of the measured nanowire in Figure 3.12C, the large background signal present even without the pump excitation shown in Figure 3.12B implies large contamination in the collected pump-probe signal if we use the detection scheme with modulation at $4f_1$ and demodulation at $3f_1$.We have experimented with higher-order harmonics of f_2, such as setting modulation and demodulation at $2f_2$, $3f_2$ or $4f_2$, and setting modulation at $2f_2$ and demodulation at f_2. These measurements produce similar results as what we have demonstrated for f_2 case, but the absolute signal intensities decrease drastically as the order increases. Therefore, for the rest of this work

presented in this thesis, all the experimental measurements are done using the detection scheme with both modulation and demodulation at f_2, unless explicitly clarified.

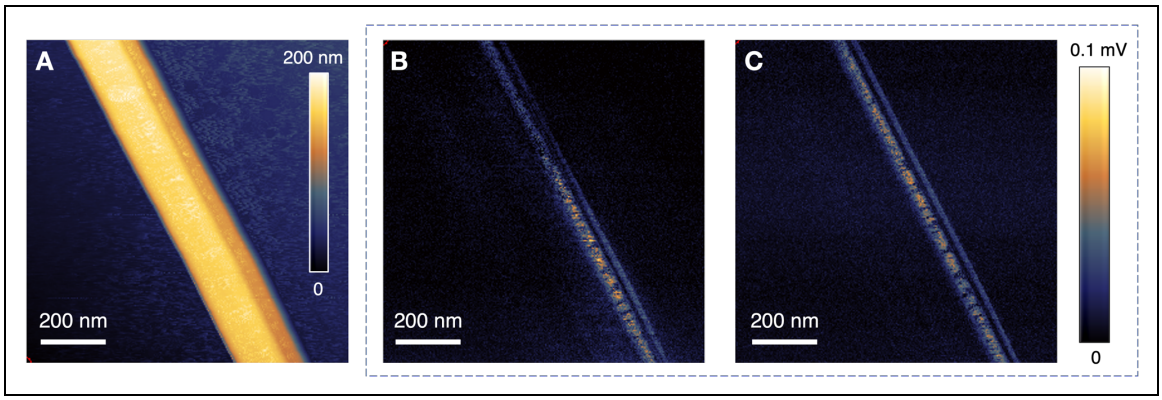

Figure 3.12 (A) The topography of the nanowire under investigation. (B) and (C) show the pump-probe signal mappings at delay time at -1 ps without and with the pump excitation, respectively, where the pump beam is modulated at $4f_1$ and the probe signal is demodulated at $3f_1$.

As a benchmark for the spatial resolution, we have successfully measured silicon nanowires with width down to 50 nm via the detection scheme with both modulation and demodulation at f_2, as shown in Figure 3.13. Strong localized pump-probe effect on the nanowire is also observed. Note that this sample is the thinnest silicon nanowire that we can find among this batch. We anticipate that the developed instrumentation can provide reliable measurements of the near-field in-situ ultra-fast optical pump-probe microscopy on nanoscale samples with characteristic length down to the size of the AFM apex.

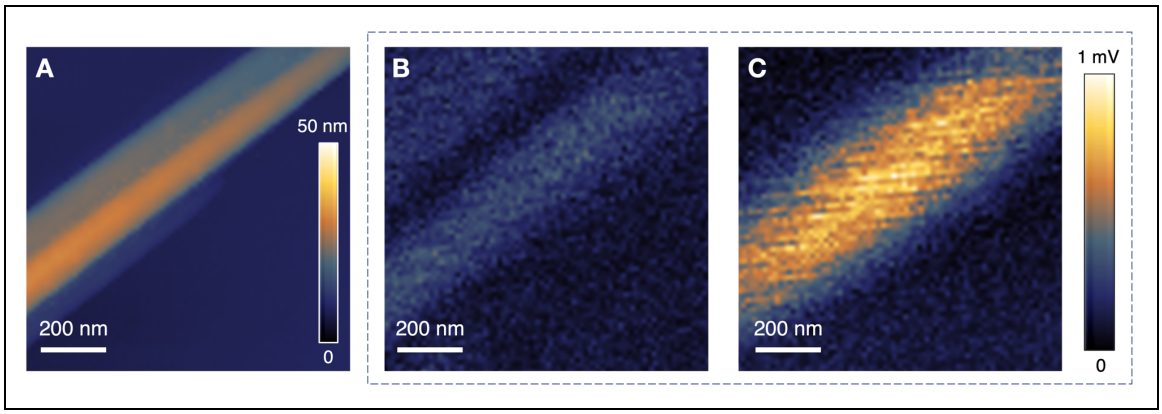

Figure 3.13 (A) The topography of the nanowire under investigation, which has a width of ~50 nm and a height of ~40 nm. (B) and (C) show the pump-probe signal mappings at delay time at -1 ps and 1 ps, respectively, where the pump beam is modulated at f_2 and the probe signal is demodulated at f_2 as well.

3.2.3 Time-domain Study of The Near Field Effect

With the confidence that we are able to exclusively collect the near-field signal, next we examine the ultra-fast dynamic process induced by the pump effect in the near field. Here we fix the tip apex at a specific location on a silicon nanowire surface, and sweep the delay stage while recording the outputs from the lock-in amplifier via a data acquisition device (DAQ, from National Instruments) Figure 3.14 plots the pump-probe signal versus the delay time at the center of a silicon nanowire with both width and height at ~500 nm, under various pump powers ranging from 0.5 mW to 21 mW. The probe power is always fixed at 0.1 mW. Note that the power is measured before the laser beams enter the acoustic enclosure, and the above values do not indicate the actual power coupled to the near field, since there is significant loss at the beam splitter, and the parabolic mirror (small-size mirror can crop the laser beam), and the coupling efficiency to the near field is below 5% by estimation, as the parabolic mirror loosely focuses the laser beams. Therefore, we estimate that only 1% ~ 5% of the measured power is transferred to the near field. However, since it is extremely difficult to calibrate the actual power at the tip apex, we use the measured power values as references throughout our discussion here. Additionally, the polarization of both the pump beam and the probe beam is optimized by the tuning the corresponding half-wave plate, and the alignment of the two beams are fine-tuned, to maximize the signal.

Figure 3.14A plots the raw data of the pump-probe signal across the whole delay range, specifically, the amplitude of the normalized change of the scattered probe light (NCS), which is defined as:

Equation 3.2 Definition of change of the scattered light intensity

$$NCS = \frac{S' - S}{S} = \frac{\Delta S}{S}$$

Here $S'$and S denote the scattered light intensity with and without the pump excitation, respectively, and the difference between them, ΔS, corresponds to the outputs from the lock-in amplifier. Note that in practice, the scattered probe light has a much wider angular distribution than the incident probe beam, and due to the finite size of the parabolic mirror, only a small portion of the scattered probe light will be collected and collimated by the parabolic mirror and eventually delivered to the photodetector. Here the scattered light intensities, $S'$and S, refer to the photodetector-collected portions. As in most of the pump-probe experiments, the pump excitation is weak perturbation, and the NCS is typically on the order of 10^{-6} ~ 10^{-4}, which is why the lock-in detection is needed. In order to compare the general shapes of the signals under different pump powers, we normalize the raw data regarding the lowest-power case in the form of linear transformation:

Equation 3.3 Signal normalization (linear transformation)

$$A(p) = b(p)A(p = 0.5\,mW) + c(p)$$

Here A denotes the amplitude and b is the normalization constant. The normalization is done regarding the maximum value of the amplitude, and the normalized data is plotted

in Figure 3.14B. Note that there are two 'normalizations' here, the first one refers to the definition of NCS, and the second one refers to the linear transformation of the raw signals. The data can be roughly classified into two groups based on their shape: the higher-power group (cases with pump powers larger than 3 mW), and the lower-power group (0.5 mW). The transient signals exhibit an instantaneous intense positive increase (bleach) feature near delay time 0, followed by an exponential decay feature which returns to 0 around 400 ps. At this stage, plot structures of both of the two groups match each other well until the 'transition' point around 400 ps. After that, the plot structure of higher-power group shows an increase feature with a slow rate, while that of the lower-power group remains close to 0. Clearly, there are two sub-processes that may take place during the studied time-range after the pump pulse excitation, and in the lower-power group the second sub-process does not happen, or its effect is too neglectable to be measured.

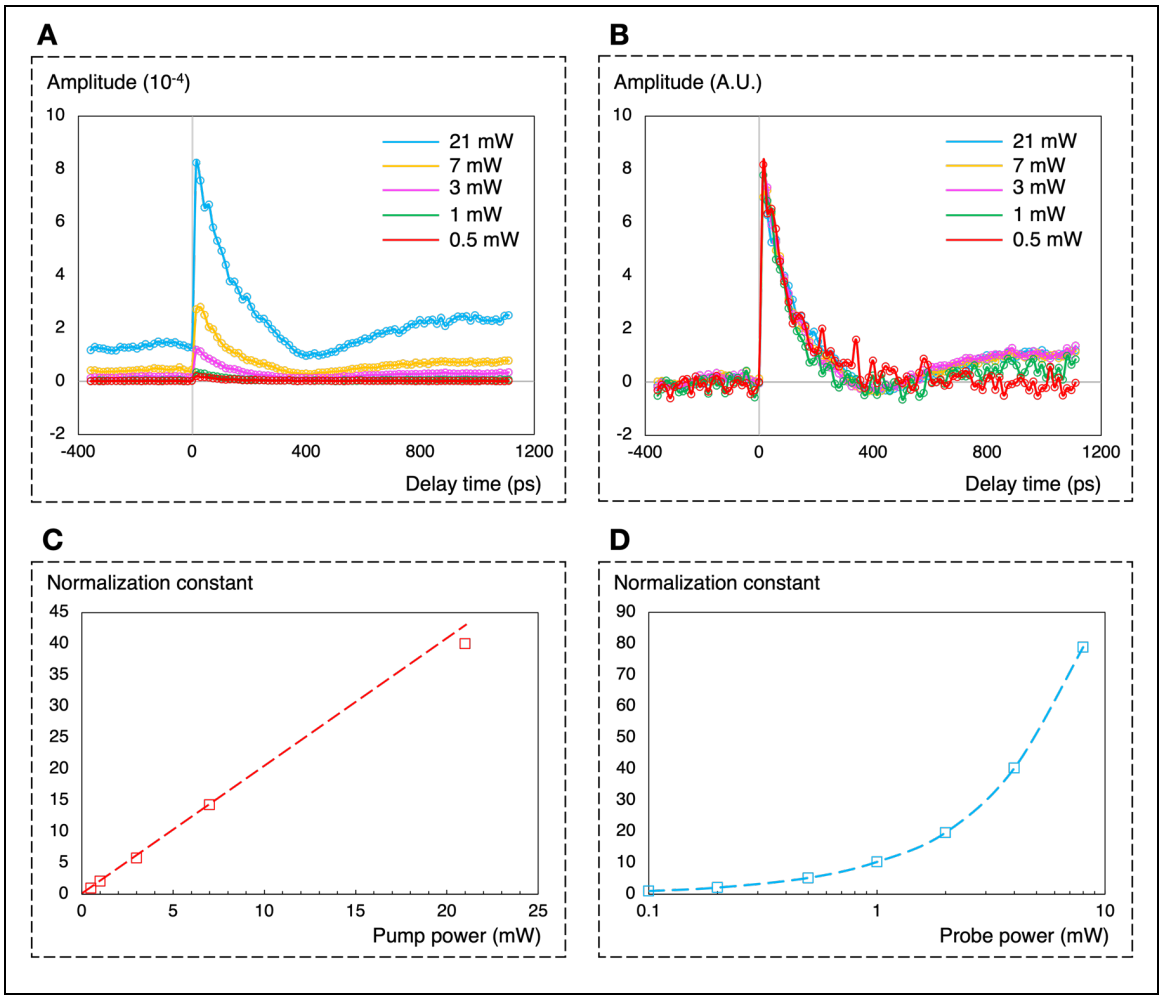

Figure 3.14 (A) Plot of the raw data of the pump-probe signal, specifically, the amplitude of the normalized change of the scattered probe light (NCS), versus delay time. (B) Plot of the linearly transformed data in (A) via Equation 3.3 regarding the maximum value of the amplitude. The data can be roughly classified into two groups based on their shape: the higher-power group, and the lower-power group. The transient signals exhibit an instantaneous intense positive going (bleach) feature near delay time 0, followed by an exponential

decay feature which returns to 0 around 400 ps. At this stage, plot structures of both of the two groups match with each other well, until the 'transition' point around 400 ps. After that, the plot structure of higher-power group shows an increase feature with a slow rate, while that of the lower-power group remains close to 0. This indicates that there are two sub-processes that may take place during the studied time-range after the pump pulse excitation, and the in the lower-power group the second sub-process does not happen, or its effect is too neglectable to be measured. (C) Plot of the normalization constant b in Equation 3.3 versus the pump power. Their relationship can be linearly fitted as indicated by the red dashed line. This indicates within the range of the pump powers used in our measurements we are not inducing non-linear effect due to high pump powers, thus the perturbation introduced by the pump pulses into the interacting system (tip-gap-sample) is weak. (D) Plot of the raw signal intensity versus the probe power, while the pump power is fixed at 1 mW and the delay time is set to 2 ps. Their relationship can also be linearly fitted as indicated by the blue (note that the x-axis is plotted in logarithm scale). As a matter of fact, the shape of the signal plot also does not depend on the probe power. Therefore, we can safely assume that the system under investigation here is a linear system with respect to the probe power. Unless explicitly clarified, all the rest of the experiments presented in this session are done with the probe power set to 0.1 mW.

The first sub-process spanning from 0 ps up to ~400 ps corresponds to the change of the local density of the free charge carriers (electrons and holes) induced by the pump excitation.[157, 167 – 180] Since the photon energy of the pump pulses (3.1 eV) is well above the band gap of silicon (1.12 eV), each pump pulse induces an instantaneous intense increase of the free carrier density in the local region of the nanowire underneath the AFM tip apex, and such change affects the transient properties that are associated to the density of free charge carriers, specifically the transient dielectric function $\epsilon(\omega)$, which determines the optical reflectance, absorptance, transmittance, and in this case the scattered light intensity.[158, 159] We monitor this dynamic change in the local density of the free charge carriers via probing the change of the scattered light intensity at wavelength at 800 nm. Fundamentally, when a photon generates a pair of free electron and hole in the semiconductor, the photon energy is transformed into the increase of potential energy and kinetic energy of the electron-hole pair (the electron and the hole have momentums along the opposite direction to satisfy conservation of momentum), and these free carriers diffuse, collide, and interact with each other through electron-electron interaction, hole-hole interaction, electron-hole interaction, electron-phonon interaction, hole-phonon interaction, and etc. Among these forms of interactions, the electron-hole interaction is the most important factor in restoring the equilibrium density of the free carriers: the electrons recombine with the holes and emit photons (or phonons) to release the extra energy (and momentum in the case of phonons). The restoring process in free carrier densities also affects the transient optical properties of the local region, which is characterized by the scattered light intensity at 800 nm. Note that at this stage, both higher-power group and the lower-power group have similar behavior as indicated in Figure 3.14B. This fact has an important indication that will be used in our later analysis: the second sub-process does not overlap with the first in higher-power cases, and signal before around the 'transition' time, 400 ps in this case, exclusively represents the first sub-process. As we will see later that the decay rate is highly dependent on the characteristic length of the nanowire, that is the width and the height.

The second sub-process after 400 ps corresponds to the thermal expansion of the silicon nanowire, which causes a decrease in the gap distance and thus an increase in the scattered light intensity. As we mentioned above, when the excessive electrons and holes

diffuse and interact with other free carriers, they also interact with the crystal lattice. Technically, a large portion of the electron-hole recombination events are phonon-assisted (indirect), where a phonon is generated rather than a photon is emitted, since the momentum mismatch of the interacting electron-hole pair needs to be carried. Therefore, part of the excessive energy in the free carrier sub-system is transferred to the phonon sub-system. The increased density of the local excited phonons, which are the quantum mechanical abstraction and quanta of the lattice vibration modes, macroscopically is represented as the thermal expansion of the crystal. Note that the thermal expansion process discussed here is fundamentally different from the picosecond acoustics studies, where a huge amount of laser power is pumped into the material and induces thermal strain wave packet to bounce back and forth along the laser incident direction in the material, causing periodic ripples on the reflectance versus delay time plot since a few tens of picoseconds.[161, 162] The thermal expansion here refers to the sluggish thermal strain release process after the ultra-fast photoexcitation. Research on the time-resolved thermal expansion of materials using ultra-fast femtosecond X-ray diffraction technique has revealed that the structural expansion due to the thermalization of photon energy in molecules starts to emerge at delay time on the order of 100 ps, and can last up to 1 μs.[163] Pudell et al also reported the observation of slow thermal equilibration in ultra-thin metallic nanostructures by ultra-fast femtosecond X-ray diffraction, where the thermal strain starts to accumulate around 10 ps and begins to release around 100 ps.[164] Measurements based on the ultra-fast optical pump-probe microscopy are also conducted to study the ultra-fast thermal expansion of materials, and the results agree well with those of ultra-fast X-ray diffraction measurements.[165] Note that the raw data for higher-power group at negative delay time have non-diminishing values, and as discussed in the previous chapter, this indicates that the system's response to the last pump pulse has not died away after 12.5 ns, due to the low heat loss through the nanowire contact area. Therefore, the thermal expansion process induced by one single pump pulse should take at least a few tens of nanoseconds to restore.

Additionally, Figure 3.14C plots the normalization constant *b* used in Equation 3.3 versus the pump power, and the relationship between them can be linearly fitted as indicated by the red dashed line. This indicates within the range of the pump powers used in our measurements we are not inducing non-linear effect due to high pump powers, thus the perturbation introduced by the pump pulses into the interacting system (tip-gap-sample) is weak. This validates our normalization processing on the raw data. Figure 3.14D plots the raw signal intensity versus the probe power, while the pump power is fixed at 1 mW and the delay time is set to 2 ps. Their relationship can also be linearly fitted (note that the x-axis is plotted in logarithm scale). As a matter of fact, the shape of the signal plot also does not depend on the probe power. Therefore, we can safely assume that the system under investigation here is a linear system with respect to the probe power. Unless explicitly clarified, all the rest of the experiments presented in this session are done with the probe power set to 0.1 mW.

Based on the two sub-processes discussed above, we fit the transformed NCS data (TNCS) plotted in Figure 3.14B by an empirical equation:

Equation 3.4 Empirical formula of amplitude of TNCS

$$A(t) = \mathbb{a}e^{-\mathbb{b}t} + \mathbb{c}\mathbb{H}(t-\mathbb{e})\left(1 - e^{-\mathbb{d}(t-\mathbb{e})}\right) + \mathbb{f}$$

Here A denotes the amplitude of the normalized change of scattered light intensity (after transformation indicated by Equation 3.3), t denotes the delay time, $\mathbb{a}$, $\mathbb{b}$, $\mathbb{c}$, $\mathbb{d}$, $\mathbb{e}$, and $\mathbb{f}$ are parameters to be fitted, and $\mathbb{H}(x)$ denotes the Heaviside function defined as:

Equation 3.5 Definition of Heaviside function

$$\mathbb{H}(x) = \begin{cases} 1, & for\ x \geq 0 \\ 0, & for\ x < 0 \end{cases}$$

In Equation 3.4, the first exponential term empirically fits the first sub-process, the recombination process of the excited free charge carriers, and the second exponential term represents the second sub-process, the thermal expansion of the crystal lattice. $\mathbb{a}$ and $\mathbb{c}$ are the amplitudes for these two terms, and $\mathbb{b}$ and $\mathbb{d}$ are the decay rates (ps-1) of the two sub-processes. The reason that we choose the exponential term to represent these the free carrier recombination process is that without going further into details the recombination rate is roughly linearly proportional to the transient density of the free carriers (n), given that the density of free electrons approximately equals that of free holes:

Equation 3.6 Kinetic equation for free carrier recombination

$$\frac{\partial n(t)}{\partial t} = -\mathbb{b}n(t)$$

Thus $\mathbb{b}$ represents the recombination rate ($\mathbb{b} > 0$), and is the same quantity as in Equation 3.4. The second exponential term comes into play in a reverse-engineering way. Phenomenologically, the restoring part of the signal can also be well fitted by an exponential term. Therefore, we empirically describe the transient thermal expansion sub-process, which results from the relaxation of the thermal strain (ϵ), with the simplified kinetic equation as:

Equation 3.6 Empirical kinetic equation for thermal strain relaxation

$$\frac{\partial \epsilon(t)}{\partial t} = -\mathbb{d}\epsilon(t)$$

Here $\mathbb{d}$ denotes the rate of thermal expansion ($\mathbb{d} > 0$). Convert the form from $e^{-\mathbb{d}t}$ to $1 - e^{-\mathbb{d}t}$ in Equation 3.4 to account for the fact that the thermal expansion decreases the gap distance thus causes the scattered light intensity to increase. Note that Equation 3.6 is oversimplified from the perspective of material mechanics, and a more precise description may involve higher order terms. However, since this requires much more complicated theoretical models which will likely introduce more parameters, we do not pursue it in this thesis. An intuitive argument for the validation of the simplification implied by Equation 3.6 is provided as following: when the sample is under high stress and has high strain, its restoring speed is high, i.e., the rate of the strain change is high, and as the strain decreases, the restoring speed decreases. Therefore, the rate of strain change is dependent on the strain.

Equation 3.6 simplifies their relationship by a linear proportionality, whereas a more accurate model may treat it differently and likely make the kinetic equation nonlinear.

The fitting parameter $\mathbb{e}$ and the Heaviside function $\mathbb{H}(t-\mathbb{e})$ come into play due to the fact that the free-electron recombination does not overlap with the thermal expansion in time domain. $\mathbb{e}$ denotes the 'transition' time mentioned above, which is the time delayed before the thermal expansion starts to take place since the pump pulse excitation. Multiplying the second term in Equation 3.4 by the Heaviside function is effectively delaying the second sub-process. $\mathbb{f}$ is a DC term for fitting purpose and has no physical interpretation. Among all the fitting parameters, we only care about the decay rates ($\mathbb{b}$ and $\mathbb{d}$) and the 'transition' time ($\mathbb{e}$).

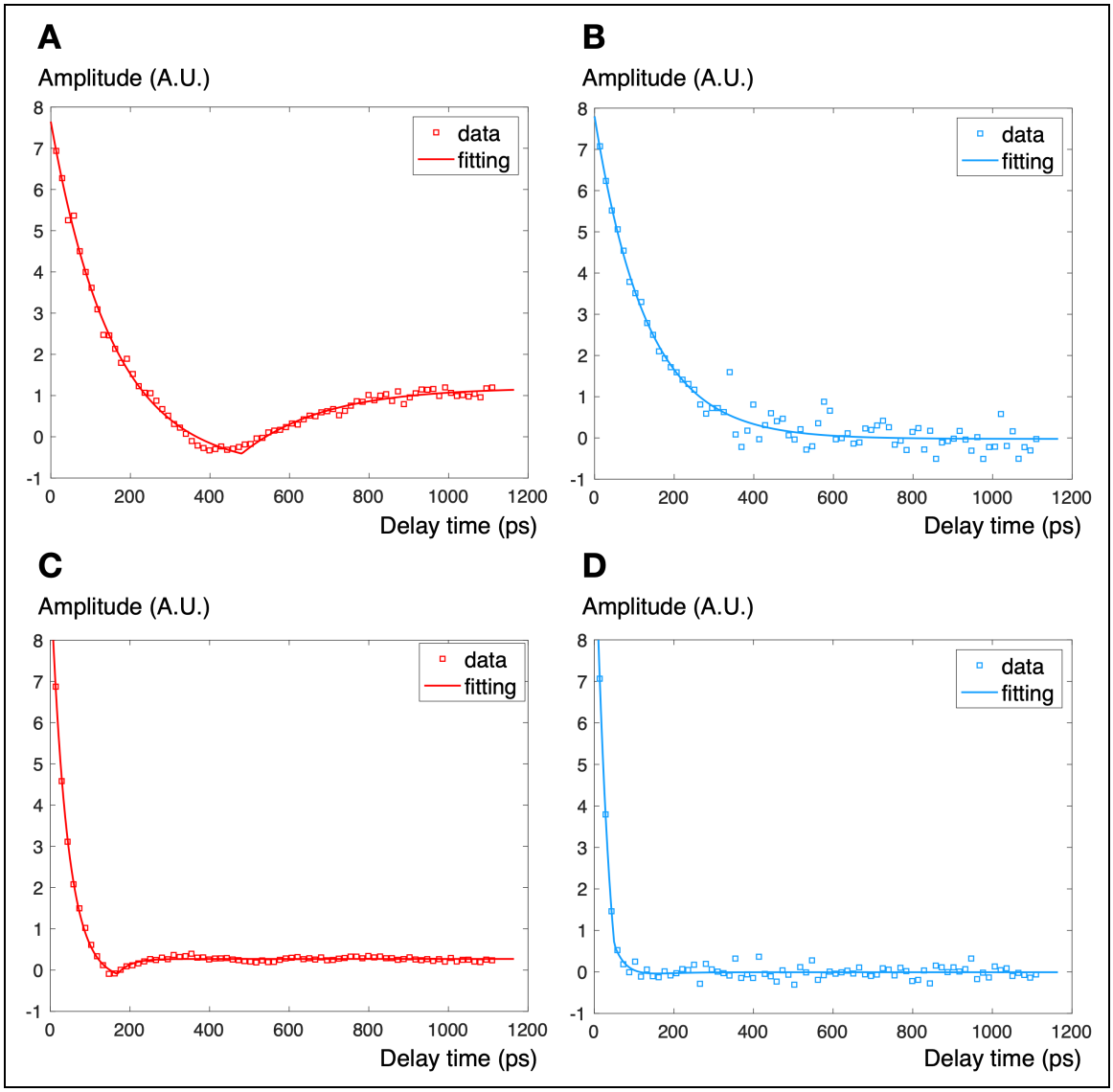

Figure 3.15 (A) and (B) plot the fittings of the linearly transformed amplitude of the normalized scattered light intensity change for the 21-mW (from the higher-power group) and the 0.5-mW (from the lower-power

group) cases, respectively, where both the width and the height of the nanowire under investigation are around 400 nm. (C) and (D) plot the fittings for the linearly transformed amplitude of the normalized scattered light intensity change of the 21-mW and the 0.5-mW cases for a silicon nanowire with both width and height of around 70 nm, respectively. In both cases, the recombination rate is independent of the power of the pump laser in the weak-perturbation regime, and the thermal expansion process will have noticeable effect only when the pump power is above certain threshold.

Figures 3.15A and B plot the fittings of the normalized (linearly transformed) data for the 21-mW (from the higher-power group) and the 0.5-mW (from the lower-power group) cases shown in Figure 3.14B. Note that both the width and the height of the nanowire under investigation here are around 400 nm. The fitting is done using the built-in curve fitting tool with the nonlinear least square (NLLS) method and the trust-region (TR) algorithm.[166] Table 3.1 and Table 3.2 summarize the relevant numerical values for the fitting parameters used in the fitting process for the higher-power case and lower-power case, respectively. Columns 'min', 'max', and 'initial' denote the minimum, maximum, and initial values set for the fitting of the corresponding parameters, respectively. Columns 'lower bound' and 'upper bound' refer to the range of the trust region with 95% confidence (The statistical possibility of the parameter lies in this range is 95%). The narrower the trust region of a parameter is, the more reliable the best fit value is. Therefore, the range of the trust region effectively characterize the sensitivity of the fitting to the corresponding parameter. For the 21-mW case, the best fit values for the parameters that we care about, the recombination rate ($\mathbb{b}$), the rate of thermal expansion ($\mathbb{d}$), and the 'transition' time ($\mathbb{e}$), are 0.006695 ps^{-1}, 0.004327 ps^{-1}, and 451.8 ps, respectively, and all of them are reliable indicated by their narrow trust regions. On the other hand, for the 0.5-mW case, the best fit value for the recombination rate is 0.007142 ps^{-1} with a narrow trust region, which is close to that of the 21-mW case, and the trust region ranges for the rate of thermal expansion and the 'transition' time are 'infinitely' large, which means that those two parameters are irrelevant in the fitting. Both fittings have small fitting errors, and the R-square values of them are 0.995 and 0.968, respectively. The fitting results validates the two conclusions that we have made earlier, and here we reformulate them: the recombination rate is independent of the power of the pump laser in the weak-perturbation regime, and the thermal expansion process will have noticeable effect only when the pump power is above certain threshold.

Table 3.1 Fitting parameters for 400-nm nanowire with 21-mW power

parameter	min	max	initial	best fit	lower bound	upper bound
$\mathbb{a}$	0	20	10	8.51	8.333	8.686
$\mathbb{b}$	0	10	1	**0.006695**	**0.00637**	**0.006911**
$\mathbb{c}$	-1	20	1	2.201	1.968	3.434
$\mathbb{d}$	0	10	1	**0.004327**	**0.003472**	**0.005181**

𝕖	300	500	400	**451.8**	**434.2**	**469.3**
𝕗	-5	5	0	-0.9344	-1.119	-0.7501

Table 3.2 Fitting parameters for 400-nm nanowire with 0.5-mW power

parameter	min	max	initial	best fit	lower bound	upper bound
𝕒	0	20	10	7.818	7.732	7.910
𝕓	0	10	1	**0.007142**	**0.006831**	**0.007359**
𝕔	-1	20	0	0	-34960	34880
𝕕	-10	10	0	**0.0000125**	**-0.01123**	**0.01126**
𝕖	300	500	400	**117.2**	**-944.3**	**1179**
𝕗	-5	5	0	-0.02503	-0.1195	-0.06946

As a comparison, Figures 3.15C and D plot the fittings for the linearly transformed amplitude of the normalized scattered light intensity change of the 21-mW and the 0.5-mW cases for a silicon nanowire with both width and height of around 70 nm, respectively. The summaries of the fitting parameters used in the two fitting processes are listed in Table 3.3 and Table 3.4, respectively. The R-square values for the two fittings are 0.9975 and 0.9795. The general structures and trends of the plots are consistent with those of the 400-nm-wide nanowire. Both the fast free carrier recombination sub-process and the sluggish lattice thermal expansion sub-process are also observed in the 21-mW case, and only the former is present in the 0.5-mW case. However, the three parameters, the recombination rate (𝕓), the rate of thermal expansion (𝕕), and the 'transition' time (𝕖), demonstrate strong dependence on the characteristic length of the sample. For the 70-nm-wide nanowire, the best fit values for the free carrier recombination rate 𝕓 are 0.02435 ps^{-1} from the 21-mW case and 0.02523 ps^{-1} from the 0.5-mW case, and rate of thermal expansion 𝕕 and the 'transition' time 𝕖 evaluate to 0.02853 ps^{-1} and 168.3 ps, respectively, from the 21-mW case. Both rates have increased a few times and the 'transition' time has reduced more than 50%, compared with the data from the 400-nm-wide nanowire case.

Table 3.3 Fitting parameters for 70-nm nanowire with 21-mW power

parameter	min	max	initial	best fit	lower bound	upper bound

𝕒	0	20	10	9.816	9.64	8.686
𝕓	0	10	1	**0.02435**	0.02339	0.02531
𝕔	-1	20	1	0.5259	0.4456	0.6061
𝕕	0	10	1	**0.02853**	0.01722	0.03984
𝕖	100	200	150	**168.3**	157.7	178.9
𝕗	-5	5	0	-0.2546	-0.3337	-0.1754

Table 3.4 Fitting parameters for 70-nm nanowire with 0.5-mW power

parameter	min	max	initial	best fit	lower bound	upper bound
𝕒	0	20	10	14.96	11.67	18.25
𝕓	0	10	1	**0.02523**	0.00987	0.04059
𝕔	-1	20	1	3.547	-0.9997	8.094
𝕕	0	10	1	**0.0002267**	**-0.01035**	**0.03499**
𝕖	100	200	150	**50.29**	**43.93**	**56.66**
𝕗	-5	5	0	-3.555	-8.097	0.9873

Figure 3.16 summarizes the dependence of the parameters on the characteristic length of the nanowire (width/thickness). Note that the results are averaged among measurements with different pump powers that are sufficient to excited corresponding sub-processes, and the error bars represent the range of the measured values. Figure 3.16A plots the free carrier recombination rate versus the nanowire width. The red dashed line is a guidance with linear proportionality to the inverse of the width, i.e., $\mathbb{b} \sim \frac{1}{d}$. We do not pursue to fit the data based on this relationship since to derive the actual dependence may require much more sophisticated theoretical models. Nevertheless, here we provide a simple argument for such dependencies. There are various mechanisms for the free carrier recombination process, such as band-to-band radiative recombination, Shockley-Read-Hall (SRH) trap-assisted recombination, Auger recombination, and surface recombination.[157, 167 – 174] Because of the high surface to volume ratio, the free carrier recombination in nanowires is expected to be dominated by surface traps.[167, 180 – 182] From Matthiessen's rule, the effective recombination rate can be expressed as:

Equation 3.7 Effective recombination rate in nanowires

$$\mathbb{b} = \mathbb{b}_0 + \mathbb{b}_s$$

Here $\mathbb{b}_0$ denotes the sum of recombination rates induced by other mechanisms, which is equal to the recombination rate in bulk silicon, and $\mathbb{b}_s$ denotes the recombination rate caused by surface recombination. The free carrier lifetime ($\mathbb{t}$), which is defined as the inverse of the recombination rate, then similarly can be formulated as:

Equation 3.8 Carrier lifetime in nanowires

$$\frac{1}{\mathbb{t}} = \frac{1}{\mathbb{t}_0} + \frac{1}{\mathbb{t}_s}$$

In nano-systems, the carrier lifetime corresponding to surface recombination ($\mathbb{t}_s$) is determined by:

Equation 3.9 Carrier lifetime dependence on sample size

$$\mathbb{t}_s = \frac{l_C}{4v_S}$$

Here v_S denotes the surface recombination velocity, which reflects the surface quality of the sample, and l_C denotes the characteristic length of the nano-system.[183 – 185] Assuming v_S does not depend on the characteristic length, the $\mathbb{t}_s$, and thus the effective carrier lifetime $\mathbb{t}$, scale linearly with l_C, the width/thickness in our case. The plot for the carrier lifetime $\mathbb{t}$ versus the width of the nanowire is presented in Figure 3.16B, and the blue dashed line is a guidance with linear relationship.

Additionally, the rate of thermal expansion ($\mathbb{d}$) and the 'transition' time ($\mathbb{e}$) also demonstrate strong dependencies on the nanowire width, as shown in Figures 3.16C and D. However, due to lack of a simple theoretical model to study the lattice dynamics, we here do not pursue to fit the data. A higher-level argument for their dependencies on the characteristic length of the nanowire is that as the size shrinks down, the accumulated thermal stress and strain can distribute themselves across the whole crystal lattice with a shorter delay (the 'transition' time is shorter), and the lattice acts to the thermal strain faster (the rate of thermal expansion is higher). Fundamentally, in contrast to the individuality and independence of the generation and recombination of electron-hole pairs, the thermal expansion process is more of a 'group' behavior that requires at least a small region of lattices to experience coherent and synchronized-in-phase motions, and thus the lack of fine granularity makes the thermal expansion process more sluggish and delayed in time domain.

From the perspective of macroscopic mechanics, since the bottom surface of the nanowire is constrained in motion by the substrate while the top surface can move freely, it can be modeled as a single-end-constrained beam, which can be further simplified as a spring-mass system, as shown in Figure 3.17. Therefore, the dynamic change of the beam height can be described by the simple harmonic oscillation of the effective spring-mass system. The natural resonant frequency of the system is:

Equation 3.10 Natural resonant frequency of simple harmonic oscillations

$$\omega_0 = \sqrt{\frac{k}{m}}$$

Here k is the spring constant of the spring, and m is the mass. The thinner nanowire has a higher k and a lower m, and thus a higher natural frequency. This perspective provides an intuitive argument for the size-dependence of the rate of thermal expansion. More advanced domain knowledge in lattice dynamics is needed to push the understanding further.

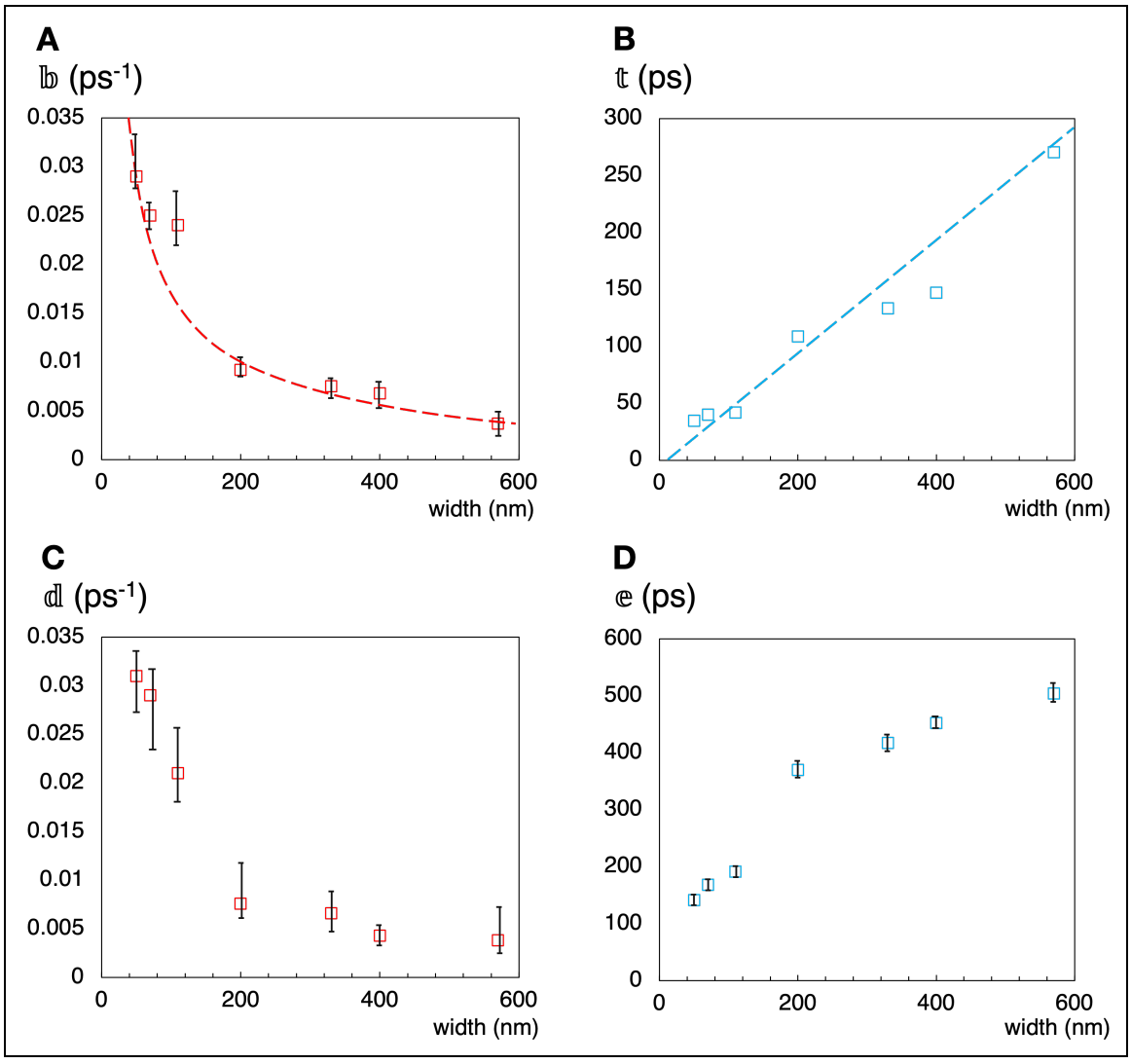

Figure 3.16 (A) Plot of the free carrier recombination rate versus the nanowire width. The red dashed line is a guidance with linear proportionality to the inverse of the width. (B) Plot of the free carrier lifetime versus the nanowire width. The blue dashed line is a guidance with linear proportionality to the width. (C) Plot of the rate of thermal expansion versus the nanowire width. (D) Plot of the 'transition' time versus the nanowire

width. Note that the results are averaged among measurements with different pump powers that are sufficient to excited corresponding sub-processes, and the error bars represent the range of the measured values.

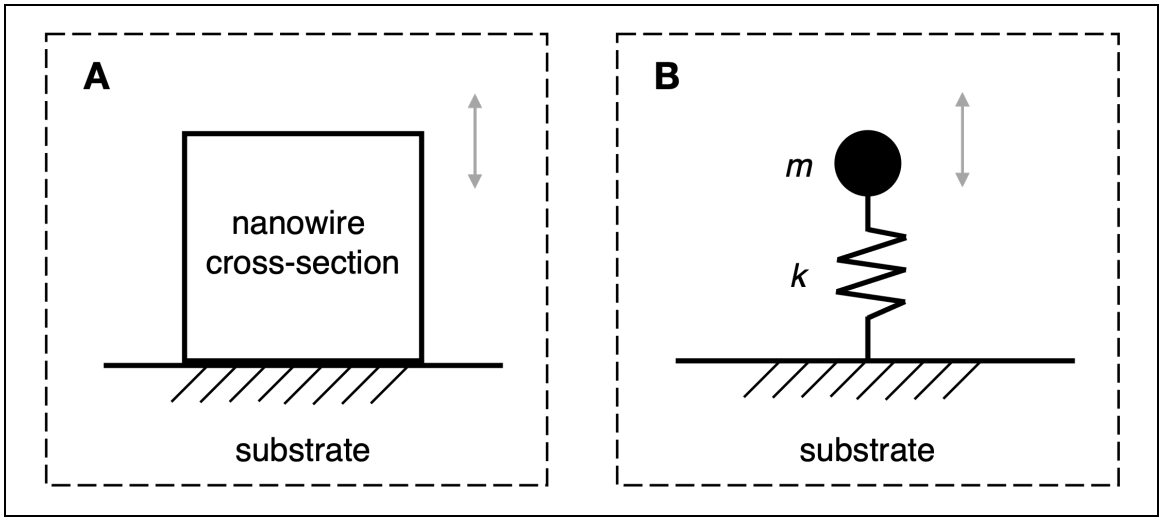

Figure 3.17 (A) Illustration of the cross-section of the nanowire-substrate system. The top surface of the nanowire can move freely, whereas the bottom surface is constrained by the substrate. (B) Illustration of the effective spring-mass system.

3.3 Summary

In this chapter, we have successfully developed the extension of the ultra-fast optical pump-probe microscopy to the near field. The integration of the far-field optical pump-probe technique with the tip-based near-field in-situ measurement brings an unprecedented and unique combination of the ultra-high temporal resolution and the ultra-high spatial resolution into the developed experimental instrumentation. With this powerful experimental technique, we have demonstrated some of the possible experimental configurations to study ultra-fast nanoscale thermal transport in non-equilibrium regime using silicon nanowires as an example. To summarize, we have listed the highlights below:

- The 'snapshot' (two-dimensional mapping) of ultra-fast photoexcitation dynamic process can be captured in two time windows, 0 ~ 1.2 ns, and 12.3 ~ 12.5 ns (negative delay time), with 300-fs temporal resolution and 20-nm spatial resolution.

- The localized time-domain response to the ultra-fast photoexcitation of a specific region on the sample surface (down to a few tens of nanometers) can be selectively recorded, and thus the dynamics of nanostructures can be reliably reconstructed. This unique capacity offers a unique way to sensitively study the dependence on the sample size of ultra-fast processes.

- The sensitive near-field detection technique makes it possible to measure processes that are not resolvable in far-field measurements, such as the thermal expansion of the sample.

- The spatial heterogeneity of the material properties or transient behaviors can be distinguished with nanometer resolution.

Besides these achievements, we have also covered some details of the exploration processes behind them, such as the 'roadmap' for extracting the near-field signal from the dominant far-field background. We hope these details will provide some general ideas and inspirations for how to 'debug' this complicated experimental instrumentation and find the optimal strategies to achieve the goals. We anticipate this powerful experimental technique will bring new avenues for exploring unveiled thermal physics in the ultra-fast non-equilibrium regime, and eventually leading to novel engineering strategies for nanoscale thermal management.

This page is left black intentionally.

4 Future Work

The discussion in the previous chapters highlights our progress in developing a novel experimental methodology that is capable of investigating nanoscale ultra-fast thermal transport and interrogating transient thermal properties of materials in the extreme non-equilibrium regime. As a summary, a novel and comprehensive optical diagnostics platform with ultra-high sensitivity and extraordinary performance is constructed to conduct thermal measurements covering a wide range of nanomaterials and nanostructures. Aiming at introducing the time-resolving capability to the instrumentation, a femtosecond laser is utilized to build ultrafast optical pump-probe microscopy, which offers access to investigating ultrafast dynamic processes that fundamental thermal carriers undergo in extreme non-equilibrium circumstances. Measurements of the transient material thermal properties across different time scales, from 100 fs to 10 ns after ultra-fast optical excitation are also made possible with the innovative time-resolved frequency-domain thermo-reflectance (Tr-FDTR) technique. Integrating the ultrafast optical pump-probe microscopy technique with near field scanning optical microscopy (NSOM) will combine both ultra-high time resolution (10 ~ 100 fs) and beyond-diffraction-limit spatial resolution (~ 10 nm). With the new technique, we have successfully demonstrated the ability to capture the 'snapshot' (two-dimensional mapping) of ultra-fast photoexcitation dynamic process with 300-fs temporal resolution and 20-nm spatial resolution. The localized time-domain response to the ultra-fast photoexcitation can be used to study the spatial heterogeneity of the material properties or transient behaviors with nanometer resolution. The sensitive near-field detection technique makes it possible to measure processes that are not resolvable in far-field measurements, such as the thermal expansion of the sample.

In this chapter, we discuss some of the potential future work based on the developed optical diagnosis platform.

4.1 Measuring Ultrafast Thermal Transport with PiFM

Upon laser illumination on the tip apex in the vicinity of the sample surface, dipole moment can be induced between the tip apex and the sample. The induced dipole moment can exert optical force, typically in the range of 1 ~ 100 pN, depending on localized electrical field, sample optical polarizability, and tip-sample distance.[186, 187] This force, although small, can alter the dynamics of the AFM tip cantilever, thus can be detected through signal demodulation of feedback from the tip. Despite being a relatively new technique, PiFM has found its applications in various research fields, such as nanoscale on-site surface chemical analysis, nanoimaging of surface plasmon/phonon polariton, and nanostructure imaging and characterization.[186 – 190] Figure 4.1 presents a comparison between the AFM topography measurement and PiFM on a Molybdenum disulfide (MoS_2) flakes sample using our NSOM system. The 'ripples' around the MoS_2 flakes are interferometric patterns of surface plasmon polaritons (SPP).

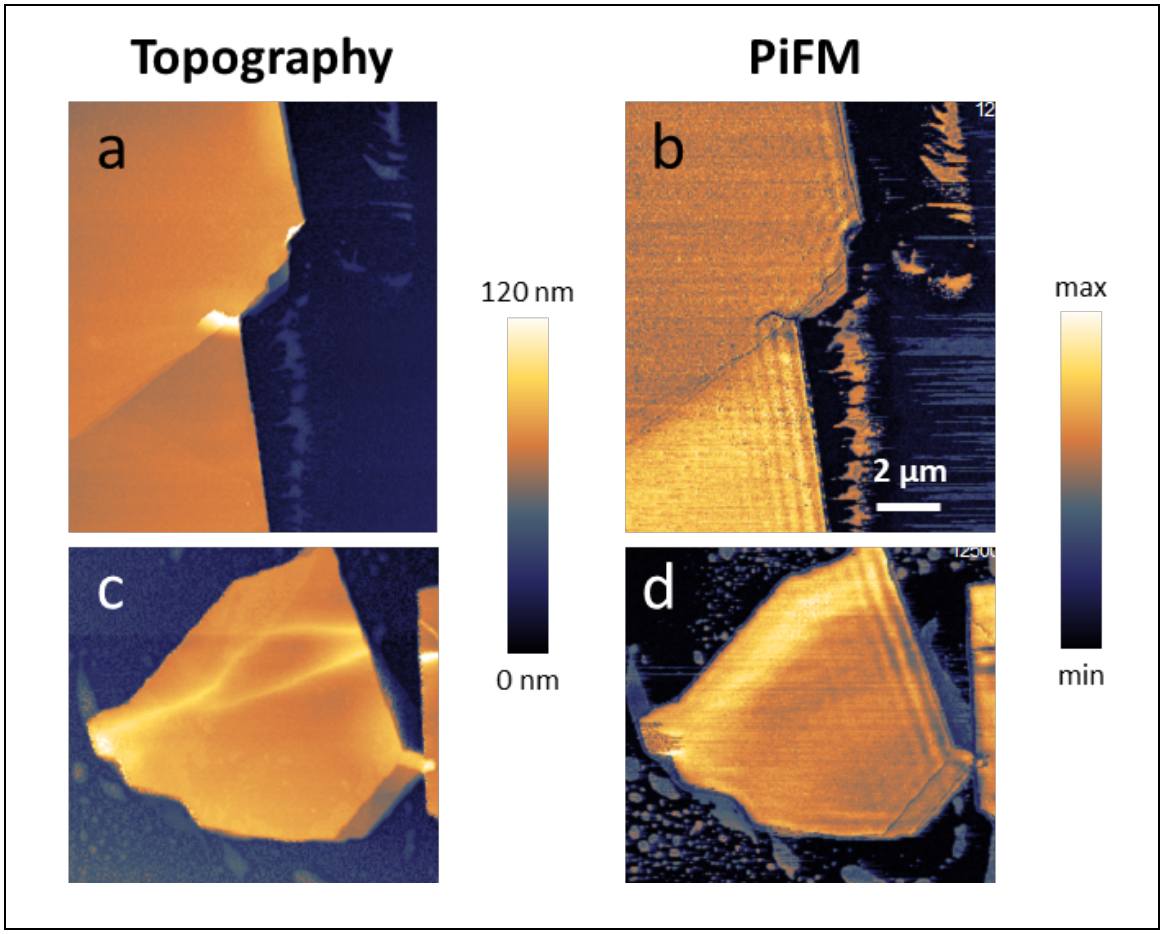

Figure 4.1 (A) and (C) show the topography of MoS2 flakes. (B) and (C) show the corresponding PiFM images.

Integrating the PiFM technique into our nanoscale ultrafast thermal transport measurement platform is straightforward. Here we illustrate one possible experimental configuration that utilizes PiFM for ultra-fast pump-probe measurement in the based on the construed NSOM instrument. The optical delivery and modulation configuration remain the same as shown in Figure 3.1, and both the pump and probe beams are coupled to the tip. On one hand, the locally confined and enhanced pump optical field induce sharp temperature rise in the sample in the vicinity of the tip, exciting local electrons and changing the temperature-dependent local optical polarizability. On the other hand, unlike the near-field Tr-FDTR, the function of probe pulses in PiFM is to induce dipole forces between the tip and sample. Since photo-induced force is sensitive to the sample polarizability, the instantaneous photo-induced force can measure the pump-induced sample polarizability change as a function of time by sweeping the delay stage. To quantitatively measure the photo-induced force, single side band modulation and demodulation method is needed: the pump laser beam is modulated at frequency difference between first (f_1) and second (f_2) mechanical resonance frequencies of the tip, i.e., the laser modulation frequency $f_m = f_2 - f_1$. In this way, the contributions from tip-sample distance change resulting from thermal expansion of sample due to both far-field and near-

field pump are excluded in the signal. Note that by utilizing different modulation and demodulation method, it is possible to distinguish different factors that contribute to the photo-induced force change in different time scale. For example, at longer delay time, the thermal expansion of the sample is the dominant contributor to the photo-induced force change since it changes the tip-sample distance. By setting the laser modulation frequency (f_m) far from both mechanical resonance frequencies of the AFM cantilever, and demodulating at $f_m - f_1$ or $f_m - f_2$, the near-field pump-induced thermal expansion of the sample can also be extracted. This feature also offers a new strategy to distinguish different degrees of freedom (electrons and phonons) in nanoscale ultrafast thermal transport.

A key advantage of PiFM over other NSOM methods lies on the fact that it does not require optical signal collection. Therefore, PiFM is intrinsically free from the large background noise problem that other optical near-field measurements face, and does not require complicated signal demodulation techniques. Since the signal that PiFM utilizes is directly from the feedback of the AFM cantilever, the photo-induced force measurement can be done simultaneously with the optical measurement described above. As a result, the integrated platform will provide comprehensive information about nanoscale ultrafast thermal transport phenomena that have not being explored.

4.2 Tracking Ultrafast Non-equilibrium Thermal Carrier Diffusion

The overarching problem of fundamental thermal physics is to decipher pathways through which microscopic interactions determine the emergent thermal properties and transport behaviors of materials. One of the major challenges is that thermal transport in materials is usually affected by multiple collaborating or competing microscopic many-body interactions, such as electron-photon, electron-electron, and electron-phonon interactions. Addressing and decoupling the roles of different active interacting degrees of freedom that underlie these phenomena has been a key target inspiring development of scientific instrumentation. Here we propose to track ultra-fast thermal carriers in the extreme nonequilibrium regime using the far-field Tr-FDTR technique described above.

Deep insights of heat transfer physics could be gained from the non-equilibrium transport proposed in this project. In electrically conducting solids, heat is carried by both electrons and phonons. Experimental determination of their relative contributions is very difficult in the equilibrium state.[191] In contrast, the distinction between phononic and electronic thermal transport would offer a unique and powerful window into the charge and phonon dynamics, as it directly probes the decoupling of heat and charge transport that would be otherwise bound together when carried by quasiparticles.

Additionally, decoupling electronic and phononic thermal conduction could potentially elucidate electron-phonon interactions. Historically, effects of electron-phonon interactions on materials' thermal conductivity are not well understood, and have been experimentally elusive.[192, 193] In electrical conductors, in addition to directly conducting heat themselves (contributing to thermal conductivity with the electronic part, κ_e), free

charge carriers also couple with and scatter phonons, hence reducing the phononic thermal conductivity (κ_L). The reduction in κ_L arising from electron-phonon coupling is typically weak as a very high density (>10^{20} cm^{-3}) of electrons is needed; hence in nonmetallic systems where carrier density is lower, it is hard to be experimentally detected. In metallic systems with very high charge carrier densities, the electron-phonon scattering could rise to levels that considerably reduce κ_L, but the measured total thermal conductivity $\kappa = \kappa_e + \kappa_L$ would then be dominated by the contribution of κ_e instead. Experimental exploration of the effects of electron-phonon scattering on thermal transport has been limited to very few metallic systems at very low temperatures, because of the difficulty in separating κ_L from κ_e. It has also been proposed that electron-phonon coupling may be responsible for unusually low values of κ observed in VN_x.[194] Yang et al. reported κ_L reduced in $NbSe_3$ nanowires beyond conventional phonon scattering mechanisms that is attributed to electron-phonon coupling.[195] Theoretical calculations done by Li et al. show that group-V transition metal carbides (VC, NbC, and TaC) host intrinsically strong electron-phonon coupling and weak phonon-phonon scattering, leading to κ_L theoretically much lower than the case when electron-phonon coupling is absent.[196] Very recently, Wu et al have discovered direct experimental evidence of κ_L dominated by electron-phonon scattering rather than the conventional phonon-phonon scattering, in a charge-density-wave material, tantalum disulfide (TaS_2).[197] Non-equilibrium thermal characterization would distinguish and record thermal relaxation via electronic and phononic processes, as well as the coupling between them.

To this end, we will perform experimental characterization of these relevant time scales and compare with theoretical calculations. For example, the electron-phonon scattering rate for the phonon mode j with wavevector $\boldsymbol{q}$ is given by:

Equation 4.1 Electron-phonon scattering rate

$$\frac{1}{\tau_{e-ph}} \propto \sum_{mn} \int d\boldsymbol{k} \left| g_{nm,j}^{e-ph}(\boldsymbol{k},\boldsymbol{q}) \right|^2 [f_{\boldsymbol{0}}(\varepsilon_{n\boldsymbol{k}}) - f_{\boldsymbol{0}}(\varepsilon_{m\boldsymbol{k}+\boldsymbol{q}})] \times \delta(\varepsilon_{m\boldsymbol{k}+\boldsymbol{q}} - \varepsilon_{n\boldsymbol{k}} - \hbar\omega_{j\boldsymbol{q}})$$

Here $\varepsilon_{n\boldsymbol{k}}$ and $\varepsilon_{m\boldsymbol{k}+\boldsymbol{q}}$ are electron energies in the initial $(n, \boldsymbol{k})$ and the final $(m, \boldsymbol{k}+\boldsymbol{q})$ states, $\hbar\omega_{j\boldsymbol{q}}$ is energy of the phonon in the state (j, q), $f_{\boldsymbol{0}}$ is Fermi distribution, $g_{nm,j}^{e-ph}(\boldsymbol{k},\boldsymbol{q})$ is e-ph scattering matrix element, and the sums are over the electron bands n and m. When the Fermi surface is nested with a wavevector $\boldsymbol{q}$, phonon modes with momentum $\hbar\boldsymbol{q}$ and energy $\hbar\omega_{j\boldsymbol{q}}$ will be strongly scattered due to the large phase space available in the integration. The thus-obtained electron-phonon scattering time scale, as well as other time scales, will be evaluated by performing first-principles calculations in the framework of density functional theory (DFT) as implemented in the Quantum Espresso (QE) package.[197]

Another major advantage of the developed Tr-FDTR over traditional TDTR is that it does not require a metallic transducer layer, allowing direct access to the electron-photon coupling in materials systems. As discussed in introduction part, measuring nonequilibrium thermal transport and characterizing transient material thermal properties is the key to understand microscopic interactions that dictate the emergent thermal transport behavior

of materials. To this end, we specifically focus on the transient thermal diffusivity of various materials, including conventional metals such as aluminum and gold, semiconductors, semimetals, and unconventional metals such as metallic Vanadium dioxide (m-VO_2). Our developed Tr-FDTR technique can characterize the transient thermal diffusivity of sample from 1 ps after ultrafast photoexcitation and up to ~10 ns, spanning 4 orders. Nonequilibrium thermal transport and its evolution to quasi-equilibrium transport will be resolved. Experimental temperature will be carefully controlled, by utilizing a cryostat (2 ~ 800 K). In general, the diffusivities of different degrees of freedom of thermal carriers, i.e., electrons and phonons, follow different characteristic temperature-dependent laws. Thus, combined with the time-dependence of the thermal diffusivity, these experiments will be able to provide a detailed overall view of these microscopic interactions and dynamics that determine the material thermal responses. Multi-layer composite materials will also be covered to investigate transport properties through interfaces of electrons and phonons. Materials with exotic phases under extreme conditions, such as high pressure, have the potential to show anomalous thermal properties, and a diamond anvil cell with up to 200 GPa pressure control could be integrated in Tr-FDTR experiments for this purpose.

4.3 Investigating Incoherent Thermal Transport above MIR Limit

The standard paradigm for transport in metals relies on the existence of quasiparticles. Electronic quasiparticles conduct electricity and heat. Phonon quasiparticles, the collective excitations of the lattice also conduct heat. Transport coefficients, such as electrical and thermal conductivities, can then be calculated using Boltzmann or Drude equations. However, the Boltzmann-Drude picture of electronic transport ceases to be valid when the electron mean-free-path becomes shorter than the Fermi wavelength. The Mott-Ioffe-Regel limit is defined where the two lengths are equal, and beyond its metallic transport becomes incoherent. To understand thermal transport in such non-quasiparticle regimes requires a new framework and has become a subject of intense efforts in recent years, triggering an urgent need for experimental results that can shed light on such regimes. Recent discoveries have shown that for cuprates, such as Yttrium barium copper oxide (YBCO), in the bad metallic regime above the MIR limit follows a unique type of transport that is dominated by diffusion of an electron – phonon 'soup', i.e., neither the phonons nor the electrons are well-defined quasiparticles, whereas their strong mutual interactions cause both to saturate at a 'Planckian' relaxation timescale $\tau_p \sim \hbar/k_B T$, which has previously been proposed to underpin transport across many families of unconventional metals.[57, 58] The incoherent electron-phonon 'soup' theory is still on the conjecture stage, and we plan to utilize the developed Tr-FDTR methodology to conduct detailed experiments for justification or disproof. The time-resolving capability of our instrument, as well as the temperature control, can directly measure in time domain the thermal carrier relaxation timescale and its dependence on temperature. The access to the early non-equilibrium thermal diffusion offered by our technique will be able to provide detailed investigations about pathways of thermalization and subsequent diffusion processes. We anticipate that the local perturbation of photo-excitation in the electron subsystem will 'scrabble' exponentially

into nonlocal degrees of freedom with a Lyapunov exponent rate $\Gamma_\chi = 1/\tau_\chi$ and spread out to affect the whole system at the butterfly velocity, vB.[198] This butterfly velocity, originally from quantum chaos theory, is used here to denote the propagation velocity of the electron-phonon 'soup', as another characteristics of incoherent thermal transport, and should fall in between phonon group velocity (v_s) and electron Fermi velocity (v_F), $v_s \leq v_B < v_F$. If these theories stand, our technique will be able to measure the timescale for photo-excited electrons to 'mix' with phonons and form the 'soup' (τ_χ), and verify that the electron and phonon subsystems are not distinguishable after the 'scrabbling' time. We will also be able to measure the new thermal diffusion velocity (v_B), and verify that it approaches v_F in the early stage after photoexcitation and decreases in the later stage. We believe that our technique will bring significant insights into this new topic, and may also be applied to study other related thermal physics.

4.4 Interrogating Anomalous Ultrafast Low-dimensional Thermal Transport

Due to the direct coupling of optical energy with sample materials without a transducer, our proposed instrumentation is much more flexible than current TDTR-based methods, thus the extension to various optical techniques is possible, and examination of intriguing material systems, such as monolayer 2D materials, can be performed. The integration of Tr-FDTR with NSOM and PiFM opens up new avenues for unveiling new fundamental thermal phenomena that originate from strong electron-phonon correlation. Some material systems that are archetypical in theoretical work but experimentally difficult to measure can be efficiently interrogated by our developed techniques, including quasi-1D nanobeam systems that support quantum phase transitions. 1D systems are of particular interest due to their simple and clean form in analytic heat transfer, allowing anomalous thermal physics effect easy to be disentangled from other thermal effects. Tantalum Disulfide (1T-TaS_2) has a well-known series of charge density wave (CDW) phase transitions. Recent studies on quasi-one-dimensional TaS_2 nanoribbon have shown that above the Debye temperature, its phonon-mediated thermal conductivity (κ_L) is limited by electron-phonon scattering in the high temperature range, resulting in a temperature-independent κ_L, whereas for usual materials κ_L is typically limited by mutual scattering of phonons, resulting in κ_L decreasing with inverse temperature.[193] Researchers believe that in this system the conventional phonon–phonon scattering is alleviated by its uniquely structured phonon dispersions, while unusually strong electron-phonon coupling arises from its Fermi surface strongly nested at wavevectors in which phonons exhibit Kohn anomalies. Since the near-field Tr-FDTR technique is an ideal tool to investigate the effect of electron-phonon interaction on thermal properties of nanoscale materials, we propose to utilize the time-resolving capability to measure the ultra-fast thermal transport in material systems with strong electron-phonon correlation. Other material options may include VO_2, doped and cuprates. These fundamental studies will reveal new physics of nanoscale thermal transport, offering a unique platform to probe electron-phonon interactions, and provide potential ways to control heat flow in materials with free charge carriers.

The developed framework of near-field Tr-FDTR allows easy adjustment to study anisotropic or inhomogeneous materials or systems, like superlattices. One of the hottest topics in physics recently is the study of twisted Van de Waals materials, such as bi-layer graphene, and transition metal dichalcogenide heterostructures, due to the fact that the formed Moiré pattern totally changes the material electronic properties.[194] Anticipating that such fundamental structural changes will also redefine the electron-phonon interactions in these systems, we therefore propose to characterize those changes with the near-filed Tr-FDTR work. Since the spatial resolution of our technique can reach ~10 nm, which is smaller or equivalent to the Moiré superlattice constant, local property fluctuations due to electron or phonon densities and their coupling can be directly accessed and characterized.

The integration of PiFM to the ultrafast pump-probe technique is also a powerful tool in these research fields. We propose to use this technique to study unusual forms of nanoscale heat transfer. Light-matter coupled surface waves, such as surface plasmon/phonon polariton, can lead to breakdown of the Planck's blackbody radiation law in the near field. We will experimentally demonstrate such surface waves can mediate energy transfer between two objects (sample and tip) at small gaps. Besides, nanoscale mechanical resonators such as pinned nanobeams or 2D material monolayer suspended on grid, will also be investigated to understand the coupling of mechanical vibrations with thermal transport and associated energy conversion. Engineering strategies will be drawn to facilitate new nanoscale cooling and thermal management technologies.

4.5 Summary

In this chapter, we have discussed several possible applications based on our instrumentation. As a closing comment, we hope these applications may extend the capacities of our developed methodologies, and offer inspirations for new ideas in the research area of nanoscale thermal physics, and in a broader scope, even the condensed matter physics.

This page is left black intentionally.

References

[1] https://www.anandtech.com/show/14231/samsung-completes-development-of-5-nm-euv-process-technology

[2] https://en.wikipedia.org/wiki/3_nm_process

[3] https://en.wikipedia.org/wiki/Moore%27s_law

[4] https://semiengineering.com/transistor-options-beyond-3nm/

[5] Cahill, D. G., Ford, W. K., Goodson, K. E., Mahan, G. D., Majumdar, A., Maris, H. J., ... & Phillpot, S. R. (2003). Nanoscale thermal transport. Journal of applied physics, 93(2), 793-818.

[6] Cahill, D. G., Braun, P. V., Chen, G., Clarke, D. R., Fan, S., Goodson, K. E., ... & Shi, L. (2014). Nanoscale thermal transport. II. 2003–2012. Applied physics reviews, 1(1), 011305.

[7] Chen, G. (2005). Nanoscale energy transport and conversion: a parallel treatment of electrons, molecules, phonons, and photons. Oxford university press.

[8] Udayabhaskararao, T., Kazes, M., Houben, L., Lin, H., & Oron, D. (2017). Nucleation, growth, and structural transformations of perovskite nanocrystals. Chemistry of Materials, 29(3), 1302-1308.

[9] Dumestre, F., Chaudret, B., Amiens, C., Renaud, P., & Fejes, P. (2004). Superlattices of iron nanocubes synthesized from Fe [N (SiMe3) 2] 2. Science, 303(5659), 821-823.

[10] Armstrong, G. (2015). An introduction to polymer nanocomposites. European Journal of Physics, 36(6), 063001.

[11] Desai, S. B., Madhvapathy, S. R., Sachid, A. B., Llinas, J. P., Wang, Q., Ahn, G. H., ... & Javey, A. (2016). MoS2 transistors with 1-nanometer gate lengths. Science, 354(6308), 99-102.

[12] Schmidt, A. J. (2008). Optical characterization of thermal transport from the nanoscale to the macroscale (Doctoral dissertation, Massachusetts Institute of Technology).

[13] Kang, J. S., Li, M., Wu, H., Nguyen, H., & Hu, Y. (2018). Experimental observation of high thermal conductivity in boron arsenide. Science, 361(6402), 575-578.

[14] Li, S., Zheng, Q., Lv, Y., Liu, X., Wang, X., Huang, P. Y., ... & Lv, B. (2018). High thermal conductivity in cubic boron arsenide crystals. Science, 361(6402), 579-581.

[15] Tian, F., Song, B., Chen, X., Ravichandran, N. K., Lv, Y., Chen, K., ... & Ren, Z. (2018). Unusual high thermal conductivity in boron arsenide bulk crystals. Science, 361(6402), 582-585.

[16] Dames, C. (2018). Ultrahigh thermal conductivity confirmed in boron arsenide. Science, 361(6402), 549-550.

[17] Chen, K., Song, B., Ravichandran, N. K., Zheng, Q., Chen, X., Lee, H., ... & Chen, G. (2020). Ultrahigh thermal conductivity in isotope-enriched cubic boron nitride. Science, 367(6477), 555-559.

[18] Slack, G. A., Tanzill, R. A., Pohl, R. O., & Vander Sande, J. W. (1973). J. Phys. Chem. Solids.

[19] Broido, D. A., Malorny, M., Birner, G., Mingo, N., & Stewart, D. A. (2007). Intrinsic lattice thermal conductivity of semiconductors from first principles. Applied Physics Letters, 91(23), 231922.

[20] Lindsay, L., Broido, D. A., & Reinecke, T. L. (2013). First-principles determination of ultrahigh thermal conductivity of boron arsenide: A competitor for diamond. Physical review letters, 111(2), 025901.

[21] Feng, T., Lindsay, L., & Ruan, X. (2017). Four-phonon scattering significantly reduces intrinsic thermal conductivity of solids. Physical Review B, 96(16), 161201.

[22] Cai, Q., Scullion, D., Gan, W., Falin, A., Zhang, S., Watanabe, K., ... & Li, L. H. (2019). High thermal conductivity of high-quality monolayer boron nitride and its thermal expansion. Science advances, 5(6), eaav0129.

[23] Chen, K., Song, B., Ravichandran, N. K., Zheng, Q., Chen, X., Lee, H., ... & Chen, G. (2020). Ultrahigh thermal conductivity in isotope-enriched cubic boron nitride. Science, 367(6477), 555-559.

[24] Goldsmid, H. (2013). Thermoelectric refrigeration. Springer.

[25] Lee, S., Hippalgaonkar, K., Yang, F., Hong, J., Ko, C., Suh, J., ... & Wu, J. (2017). Anomalously low electronic thermal conductivity in metallic vanadium dioxide. Science, 355(6323), 371-374.

[26] Chen, G. (1998). Thermal conductivity and ballistic-phonon transport in the cross-plane direction of superlattices. Physical Review B, 57(23), 14958.

[27] Harman, T. C., Taylor, P. J., Walsh, M. P., & LaForge, B. E. (2002). Quantum dot superlattice thermoelectric materials and devices. science, 297(5590), 2229-2232.

[28] Yang, R., & Chen, G. (2004). Thermal conductivity modeling of periodic two-dimensional nanocomposites. Physical Review B, 69(19), 195316.

[29] Ottens, R. S., Quetschke, V., Wise, S., Alemi, A. A., Lundock, R., Mueller, G., ... & Whiting, B. F. (2011). Near-field radiative heat transfer between macroscopic planar surfaces. Physical Review Letters, 107(1), 014301.

[30] Song, B., Thompson, D., Fiorino, A., Ganjeh, Y., Reddy, P., & Meyhofer, E. (2016). Radiative heat conductances between dielectric and metallic parallel plates with nanoscale gaps. Nature nanotechnology, 11(6), 509-514.

[31] Watjen, J. I., Zhao, B., & Zhang, Z. M. (2016). Near-field radiative heat transfer between doped-Si parallel plates separated by a spacing down to 200 nm. Applied Physics Letters, 109(20), 203112.

[32] Ghashami, M., Geng, H., Kim, T., Iacopino, N., Cho, S. K., & Park, K. (2018). Precision measurement of phonon-polaritonic near-field energy transfer between macroscale planar structures under large thermal gradients. Physical review letters, 120(17), 175901.

[33] Fiorino, A., Thompson, D., Zhu, L., Song, B., Reddy, P., & Meyhofer, E. (2018). Giant enhancement in radiative heat transfer in sub-30 nm gaps of plane parallel surfaces. Nano letters, 18(6), 3711-3715.

[34] Ezzahri, Y., & Joulain, K. (2014). Vacuum-induced phonon transfer between two solid dielectric materials: illustrating the case of Casimir force coupling. Physical Review B, 90(11), 115433.

[35] Fong, K. Y., Li, H. K., Zhao, R., Yang, S., Wang, Y., & Zhang, X. (2019). Phonon heat transfer across a vacuum through quantum fluctuations. Nature, 576(7786), 243-247.

[36] Christofferson, J., Maize, K., Ezzahri, Y., Shabani, J., Wang, X., & Shakouri, A. (2008). Microscale and nanoscale thermal characterization techniques.

[37] Yue, Y., & Wang, X. (2012). Nanoscale thermal probing. Nano reviews, 3(1), 11586.

[38] Kucsko, G., Maurer, P. C., Yao, N. Y., Kubo, M. I. C. H. A. E. L., Noh, H. J., Lo, P. K., ... & Lukin, M. D. (2013). Nanometer-scale thermometry in a living cell. Nature, 500(7460), 54-58.

[39] Lucchetta, E. M., Lee, J. H., Fu, L. A., Patel, N. H., & Ismagilov, R. F. (2005). Dynamics of Drosophila embryonic patterning network perturbed in space and time using microfluidics. Nature, 434(7037), 1134-1138.

[40] Kumar, S. V., & Wigge, P. A. (2010). H2A. Z-containing nucleosomes mediate the thermosensory response in Arabidopsis. Cell, 140(1), 136-147.

[41] Lauschke, V. M., Tsiairis, C. D., François, P., & Aulehla, A. (2013). Scaling of embryonic patterning based on phase-gradient encoding. Nature, 493(7430), 101-105.

[42] Kamei, Y., Suzuki, M., Watanabe, K., Fujimori, K., Kawasaki, T., Deguchi, T., ... & Yuba, S. (2009). Infrared laser–mediated gene induction in targeted single cells in vivo. Nature methods, 6(1), 79-81.

[43] Vreugdenburg, T. D., Willis, C. D., Mundy, L., & Hiller, J. E. (2013). A systematic review of elastography, electrical impedance scanning, and digital infrared thermography for breast cancer screening and diagnosis. Breast cancer research and treatment, 137(3), 665-676.

[44] Schroeder, A., Heller, D. A., Winslow, M. M., Dahlman, J. E., Pratt, G. W., Langer, R., ... & Anderson, D. G. (2012). Treating metastatic cancer with nanotechnology. Nature Reviews Cancer, 12(1), 39-50.

[45] O'Neal, D. P., Hirsch, L. R., Halas, N. J., Payne, J. D., & West, J. L. (2004). Photo-thermal tumor ablation in mice using near infrared-absorbing nanoparticles. Cancer letters, 209(2), 171-176.

[46] Gomès, S., Assy, A., & Chapuis, P. O. (2015). Scanning thermal microscopy: A review. physica status solidi (a), 212(3), 477-494.

[47] Zhang, Y., Zhu, W., Hui, F., Lanza, M., Borca-Tasciuc, T., & Muñoz Rojo, M. (2020). A review on principles and applications of scanning thermal microscopy (SThM). Advanced functional materials, 30(18), 1900892.

[48] Menges, F., Riel, H., Stemmer, A., & Gotsmann, B. (2016). Nanoscale thermometry by scanning thermal microscopy. Review of Scientific Instruments, 87(7), 074902.

[49] Hillenbrand, R., Knoll, B., & Keilmann, F. (2001). Pure optical contrast in scattering-type scanning near-field microscopy. Journal of microscopy, 202(1), 77-83.

[50] Zhang, D., Zheng, X., & Di Ventra, M. (2019). Local temperatures out of equilibrium. Physics Reports, 830, 1-66.

[51] Christofferson, J., Maize, K., Ezzahri, Y., Shabani, J., Wang, X., & Shakouri, A. (2008). Microscale and nanoscale thermal characterization techniques.

[52] Lahrech, A., Bachelot, R., Gleyzes, P., & Boccara, A. C. (1996). Infrared-reflection-mode near-field microscopy using an apertureless probe with a resolution of λ/600. Optics letters, 21(17), 1315-1317.

[53] Yue, Y., Chen, X., & Wang, X. (2011). Noncontact sub-10 nm temperature measurement in near-field laser heating. ACS Nano, 5(6), 4466-4475.

[54] Govenius, J., Lake, R. E., Tan, K. Y., & Möttönen, M. (2016). Detection of zeptojoule microwave pulses using electrothermal feedback in proximity-induced Josephson junctions. Physical review letters, 117(3), 030802.

[55] Liu, K., Lee, S., Yang, S., Delaire, O., & Wu, J. (2018). Recent progresses on physics and applications of vanadium dioxide. Materials Today, 21(8), 875-896.

[56] Zhao, D., Qian, X., Gu, X., Jajja, S. A., & Yang, R. (2016). Measurement techniques for thermal conductivity and interfacial thermal conductance of bulk and thin film materials. Journal of Electronic Packaging, 138(4), 040802.

[57] Luckyanova, Maria N., Jivtesh Garg, Keivan Esfarjani, Adam Jandl, Mayank T. Bulsara, Aaron J. Schmidt, Austin J. Minnich et al. "Coherent phonon heat conduction in superlattices." Science 338, no. 6109 (2012): 936-939.

[58] Schmidt, A. J., Cheaito, R., & Chiesa, M. (2009). A frequency-domain thermoreflectance method for the characterization of thermal properties. Review of scientific instruments, 80(9), 094901.

[59] Cahill, D. G. (2004). Analysis of heat flow in layered structures for time-domain thermoreflectance. Review of scientific instruments, 75(12), 5119-5122.

[60] Kang, K., Koh, Y. K., Chiritescu, C., Zheng, X., & Cahill, D. G. (2008). Two-tint pump-probe measurements using a femtosecond laser oscillator and sharp-edged optical filters. Review of Scientific Instruments, 79(11), 114901.

[61] Schmidt, A. J., Chen, X., & Chen, G. (2008). Pulse accumulation, radial heat conduction, and anisotropic thermal conductivity in pump-probe transient thermoreflectance. Review of Scientific Instruments, 79(11), 114902.

[62] Zhu, J., Tang, D., Wang, W., Liu, J., Holub, K. W., & Yang, R. (2010). Ultrafast thermoreflectance techniques for measuring thermal conductivity and interface thermal conductance of thin films. Journal of Applied Physics, 108(9), 094315.

[63] Chiritescu, C., Cahill, D. G., Nguyen, N., Johnson, D., Bodapati, A., Keblinski, P., & Zschack, P. (2007). Ultralow thermal conductivity in disordered, layered WSe2 crystals. Science, 315(5810), 351-353.

[64] Oh, D. W., Ko, C., Ramanathan, S., & Cahill, D. G. (2010). Thermal conductivity and dynamic heat capacity across the metal-insulator transition in thin film VO 2. Applied Physics Letters, 96(15), 151906.

[65] Cheaito, R., Duda, J. C., Beechem, T. E., Hattar, K., Ihlefeld, J. F., Medlin, D. L., ... & Hopkins, P. E. (2012). Experimental investigation of size effects on the thermal

conductivity of silicon-germanium alloy thin films. Physical review letters, 109(19), 195901.

[66] Zheng, Q., Braun, P. V., & Cahill, D. G. (2016). Thermal conductivity of graphite thin films grown by low temperature chemical vapor deposition on Ni (111). Advanced Materials Interfaces, 3(16), 1600234.

[67] Zhang, H., Chen, X., Jho, Y. D., & Minnich, A. J. (2016). Temperature-dependent mean free path spectra of thermal phonons along the c-axis of graphite. Nano letters, 16(3), 1643-1649.

[68] Guo, Z., Verma, A., Wu, X., Sun, F., Hickman, A., Masui, T., ... & Luo, T. (2015). Anisotropic thermal conductivity in single crystal β-gallium oxide. Applied Physics Letters, 106(11), 111909.

[69] Qian, X., Jiang, P., & Yang, R. (2017). Anisotropic thermal conductivity of 4H and 6H silicon carbide measured using time-domain thermoreflectance. Materials Today Physics, 3, 70-75.

[70] Liu, J., Choi, G. M., & Cahill, D. G. (2014). Measurement of the anisotropic thermal conductivity of molybdenum disulfide by the time-resolved magneto-optic Kerr effect. Journal of Applied Physics, 116(23), 233107.

[71] Jiang, P., Qian, X., Gu, X., & Yang, R. (2017). Probing anisotropic thermal conductivity of transition metal dichalcogenides MX2 (M= Mo, W and X= S, Se) using time-domain thermoreflectance. Advanced Materials, 29(36), 1701068.

[72] Jiang, P., Qian, X., & Yang, R. (2018). Tutorial: Time-domain thermoreflectance (TDTR) for thermal property characterization of bulk and thin film materials. Journal of Applied Physics, 124(16), 161103.

[73] Cheng, Z., Bougher, T., Bai, T., Wang, S. Y., Li, C., Yates, L., ... & Graham, S. (2018). Probing growth-induced anisotropic thermal transport in high-quality CVD diamond membranes by multifrequency and multiple-spot-size time-domain thermoreflectance. ACS applied materials & interfaces, 10(5), 4808-4815.

[74] Liu, J., Zhu, J., Tian, M., Gu, X., Schmidt, A., & Yang, R. (2013). Simultaneous measurement of thermal conductivity and heat capacity of bulk and thin film materials using frequency-dependent transient thermoreflectance method. Review of Scientific Instruments, 84(3), 034902.

[75] Wei, C., Zheng, X., Cahill, D. G., & Zhao, J. C. (2013). Invited Article: Micron resolution spatially resolved measurement of heat capacity using dual-frequency time-domain thermoreflectance. Review of Scientific Instruments, 84(7), 071301.

[76] Gundrum, B. C., Cahill, D. G., & Averback, R. S. (2005). Thermal conductance of metal-metal interfaces. Physical Review B, 72(24), 245426.

[77] Lyeo, H. K., & Cahill, D. G. (2006). Thermal conductance of interfaces between highly dissimilar materials. Physical Review B, 73(14), 144301.

[78] Donovan, B. F., Szwejkowski, C. J., Duda, J. C., Cheaito, R., Gaskins, J. T., Peter Yang, C. Y., ... & Hopkins, P. E. (2014). Thermal boundary conductance across metal-gallium nitride interfaces from 80 to 450 K. Applied Physics Letters, 105(20), 203502.

[79] Hohensee, G. T., Wilson, R. B., & Cahill, D. G. (2015). Thermal conductance of metal–diamond interfaces at high pressure. Nature communications, 6(1), 1-9.

[80] Wilson, R. B., Apgar, B. A., Hsieh, W. P., Martin, L. W., & Cahill, D. G. (2015). Thermal conductance of strongly bonded metal-oxide interfaces. Physical Review B, 91(11), 115414.

[81] Larkin, L. S., Redding, M. R., Le, N. Q., & Norris, P. M. (2017). Temperature-dependent thermal boundary conductance at metal/indium-based III–V semiconductor interfaces. Journal of Heat Transfer, 139(3).

[82] Costescu, R. M., Wall, M. A., & Cahill, D. G. (2003). Thermal conductance of epitaxial interfaces. Physical Review B, 67(5), 054302.

[83] Losego, M. D., Grady, M. E., Sottos, N. R., Cahill, D. G., & Braun, P. V. (2012). Effects of chemical bonding on heat transport across interfaces. Nature materials, 11(6), 502-506.

[84] Ziade, E., Yang, J., Brummer, G., Nothern, D., Moustakas, T., & Schmidt, A. J. (2015). Thermal transport through GaN–SiC interfaces from 300 to 600 K. Applied Physics Letters, 107(9), 091605.

[85] Schmidt, A. J. (2013). Pump-probe thermoreflectance. Annual Review of Heat Transfer, 16.

[86] Hecht, E. (1998). Hecht optics. Addison Wesley, 997, 213-214.

[87] Capinski, W. S., & Maris, H. J. (1996). Improved apparatus for picosecond pump-and-probe optical measurements. Review of Scientific Instruments, 67(8), 2720-2726.

[88] Sun, B., & Koh, Y. K. (2016). Understanding and eliminating artifact signals from diffusely scattered pump beam in measurements of rough samples by time-domain thermoreflectance (TDTR). Review of Scientific Instruments, 87(6), 064901.

[89] Stanford Research Systems (2016) User's Manual: Model SR844 RF Lock-In Amplifier, revision 2.9 edition.

[90] Carslaw, H. S., & Jaeger, J. C. (1959). Conduction of heat in solids (No. 536.23). Clarendon Press.

[91] Hamby, D. M. (1994). A review of techniques for parameter sensitivity analysis of environmental models. Environmental monitoring and assessment, 32(2), 135-154.

[92] Yang, J., Maragliano, C., & Schmidt, A. J. (2013). Thermal property microscopy with frequency domain thermoreflectance. Review of Scientific Instruments, 84(10), 104904.

[93] Schmidt, A. J., Cheaito, R., & Chiesa, M. (2009). A frequency-domain thermoreflectance method for the characterization of thermal properties. Review of scientific instruments, 80(9), 094901.

[94] Regner, K. T., Sellan, D. P., Su, Z., Amon, C. H., McGaughey, A. J., & Malen, J. A. (2013). Broadband phonon mean free path contributions to thermal conductivity measured using frequency domain thermoreflectance. Nature communications, 4(1), 1-7.

[95] Malen, J. A., Baheti, K., Tong, T., Zhao, Y., Hudgings, J. A., & Majumdar, A. (2011). Optical measurement of thermal conductivity using fiber aligned frequency domain thermoreflectance.

[96] Regner, K. T., Majumdar, S., & Malen, J. A. (2013). Instrumentation of broadband frequency domain thermoreflectance for measuring thermal conductivity accumulation functions. Review of Scientific Instruments, 84(6), 064901.

[97] Beardo, A., Hennessy, M. G., Sendra, L., Camacho, J., Myers, T. G., Bafaluy, J., & Alvarez, F. X. (2020). Phonon hydrodynamics in frequency-domain thermoreflectance experiments. Physical Review B, 101(7), 075303.

[98] Rahman, M., Shahzadeh, M., Braeuninger-Weimer, P., Hofmann, S., Hellwig, O., & Pisana, S. (2018). Measuring the thermal properties of anisotropic materials using beam-offset frequency domain thermoreflectance. Journal of Applied Physics, 123(24), 245110.

[99] Collins, K. C., Maznev, A. A., Cuffe, J., Nelson, K. A., & Chen, G. (2014). Examining thermal transport through a frequency-domain representation of time-domain thermoreflectance data. Review of Scientific Instruments, 85(12), 124903.

[100] Rodin, D., & Yee, S. K. (2017). Simultaneous measurement of in-plane and through-plane thermal conductivity using beam-offset frequency domain thermoreflectance. Review of Scientific Instruments, 88(1), 014902.

[101] Wang, L., Cheaito, R., Braun, J. L., Giri, A., & Hopkins, P. E. (2016). Thermal conductivity measurements of non-metals via combined time-and frequency-domain thermoreflectance without a metal film transducer. Review of Scientific Instruments, 87(9), 094902.

[102] Qian, X., Ding, Z., Shin, J., Schmidt, A. J., & Chen, G. (2020). Accurate measurement of in-plane thermal conductivity of layered materials without metal film transducer using frequency domain thermoreflectance. Review of Scientific Instruments, 91(6), 064903.

[103] Xing, C., Jensen, C., Hua, Z., Ban, H., Hurley, D. H., Khafizov, M., & Kennedy, J. R. (2012). Parametric study of the frequency-domain thermoreflectance technique. Journal of Applied Physics, 112(10), 103105.

[104] Ramu, A. T., & Bowers, J. E. (2015). A compact heat transfer model based on an enhanced Fourier law for analysis of frequency-domain thermoreflectance experiments. Applied Physics Letters, 106(26), 263102.

[105] Ziade, E. (2020). Wide bandwidth frequency-domain thermoreflectance: Volumetric heat capacity, anisotropic thermal conductivity, and thickness measurements. Review of Scientific Instruments, 91(12), 124901.

[106] Shen, W., Vaca, D., & Kumar, S. (2020). Reconsidering uncertainty from frequency domain thermoreflectance measurement and novel data analysis by deep learning. Nanoscale and Microscale Thermophysical Engineering, 24(3-4), 138-149.

[107] Gao, Y., Marconnet, A. M., Xiang, R., Maruyama, S., & Goodson, K. E. (2013). Heat capacity, thermal conductivity, and interface resistance extraction for single-walled carbon nanotube films using frequency-domain thermoreflectance. IEEE Transactions on Components, Packaging and Manufacturing Technology, 3(9), 1524-1532.

[108] Myers, K. B., Gaddam, P. R., Ding, X., Kochergin, V., Huxtable, S. T., & Robinson, H. D. (2018). Measuring Thermal Conductivity with Magnitude-Dependent Frequency–Domain Thermoreflectance Using Modulated CW Lasers. International Journal of Thermophysics, 39(12), 1-15.

[109] Tang, L., & Dames, C. (2021). Anisotropic thermal conductivity tensor measurements using beam-offset frequency domain thermoreflectance (BO-FDTR) for materials lacking in-plane symmetry. International Journal of Heat and Mass Transfer, 164, 120600.

[110] Shahzadeh, M., Rahman, M., Hellwig, O., & Pisana, S. (2018). High-frequency measurements of thermophysical properties of thin films using a modified broad-band frequency domain thermoreflectance approach. Review of Scientific Instruments, 89(8), 084905.

[111] Yang, J., Ziade, E., & Schmidt, A. J. (2016). Uncertainty analysis of thermoreflectance measurements. Review of Scientific Instruments, 87(1), 014901.

[112] Goni, M., Patelka, M., Ikeda, S., Sato, T., & Schmidt, A. J. (2018). Frequency domain thermoreflectance technique for measuring the thermal conductivity of individual micro-particles. Review of Scientific Instruments, 89(7), 074901.

[113] Feser, J. P., & Cahill, D. G. (2012). Probing anisotropic heat transport using time-domain thermoreflectance with offset laser spots. Review of Scientific Instruments, 83(10), 104901.

[114] Wei, C., Zheng, X., Cahill, D. G., & Zhao, J. C. (2013). Invited Article: Micron resolution spatially resolved measurement of heat capacity using dual-frequency time-domain thermoreflectance. Review of Scientific Instruments, 84(7), 071301.

[115] Liu, J., Choi, G. M., & Cahill, D. G. (2014). Measurement of the anisotropic thermal conductivity of molybdenum disulfide by the time-resolved magneto-optic Kerr effect. Journal of Applied Physics, 116(23), 233107.

[116] Feser, J. P., Liu, J., & Cahill, D. G. (2014). Pump-probe measurements of the thermal conductivity tensor for materials lacking in-plane symmetry. Review of Scientific Instruments, 85(10), 104903.

[117] Jiang, P., Qian, X., & Yang, R. (2018). Tutorial: Time-domain thermoreflectance (TDTR) for thermal property characterization of bulk and thin film materials. Journal of Applied Physics, 124(16), 161103.

[118] Kimling, J., Philippi-Kobs, A., Jacobsohn, J., Oepen, H. P., & Cahill, D. G. (2017). Thermal conductance of interfaces with amorphous SiO 2 measured by time-resolved magneto-optic Kerr-effect thermometry. Physical Review B, 95(18), 184305.

[119] Zhu, J., Park, H., Chen, J. Y., Gu, X., Zhang, H., Karthikeyan, S., ... & Wang, X. (2016). Revealing the origins of 3D anisotropic thermal conductivities of black phosphorus. Advanced Electronic Materials, 2(5), 1600040.

[120] O'Hara, K. E., Hu, X., & Cahill, D. G. (2001). Characterization of nanostructured metal films by picosecond acoustics and interferometry. Journal of applied physics, 90(9), 4852-4858.

[121] Florez, O., Jarschel, P. F., Espinel, Y. A., Cordeiro, C. M. B., Alegre, T. M., Wiederhecker, G. S., & Dainese, P. (2016). Brillouin scattering self-cancellation. Nature communications, 7(1), 1-8.

[122] Cinchetti, M., Albaneda, M. S., Hoffmann, D., Roth, T., Wüstenberg, J. P., Krauß, M., ... & Aeschlimann, M. (2006). Spin-flip processes and ultrafast magnetization dynamics in Co: Unifying the microscopic and macroscopic view of femtosecond magnetism. Physical review letters, 97(17), 177201.

[123] Carpene, E., Mancini, E., Dallera, C., Brenna, M., Puppin, E., & De Silvestri, S. (2008). Dynamics of electron-magnon interaction and ultrafast demagnetization in thin iron films. Physical Review B, 78(17), 174422.

[124] Hofherr, M., Häuser, S., Dewhurst, J. K., Tengdin, P., Sakshath, S., Nembach, H. T., ... & Mathias, S. (2020). Ultrafast optically induced spin transfer in ferromagnetic alloys. Science advances, 6(3), eaay8717.

[125] Qi, J., Xu, Y., Steigerwald, A., Liu, X., Furdyna, J. K., Perakis, I. E., & Tolk, N. H. (2009). Ultrafast laser-induced coherent spin dynamics in ferromagnetic Ga 1− x Mn x As/GaAs structures. Physical Review B, 79(8), 085304.

[126] Weber, A., Pressacco, F., Guenther, S., Mancini, E., Oppeneer, P. M., & Back, C. H. (2011). Ultrafast demagnetization dynamics of thin Fe/W (110) films: Comparison of time- and spin-resolved photoemission with time-resolved magneto-optic experiments. Physical Review B, 84(13), 132412.

[127] Choi, G. M., Min, B. C., Lee, K. J., & Cahill, D. G. (2014). Spin current generated by thermally driven ultrafast demagnetization. Nature communications, 5(1), 1-8.

[128] Krauß, M., Roth, T., Alebrand, S., Steil, D., Cinchetti, M., Aeschlimann, M., & Schneider, H. C. (2009). Ultrafast demagnetization of ferromagnetic transition metals: The role of the Coulomb interaction. Physical Review B, 80(18), 180407.

[129] Kimling, J., Kimling, J., Wilson, R. B., Hebler, B., Albrecht, M., & Cahill, D. G. (2014). Ultrafast demagnetization of FePt: Cu thin films and the role of magnetic heat capacity. Physical Review B, 90(22), 224408.

[130] Choi, G. M., Moon, C. H., Min, B. C., Lee, K. J., & Cahill, D. G. (2015). Thermal spin-transfer torque driven by the spin-dependent Seebeck effect in metallic spin-valves. Nature physics, 11(7), 576-581.

[131] Gebs, R., Klatt, G., Janke, C., Dekorsy, T., & Bartels, A. (2010). High-speed asynchronous optical sampling with sub-50fs time resolution. Optics express, 18(6), 5974-5983.

[132] Klatt, G., Gebs, R., Schäfer, H., Nagel, M., Janke, C., Bartels, A., & Dekorsy, T. (2010). High-resolution terahertz spectrometer. IEEE journal of selected topics in quantum electronics, 17(1), 159-168.

[133] Elzinga, P. A., Lytle, F. E., Jian, Y., King, G. B., & Laurendeau, N. M. (1987). Pump/probe spectroscopy by asynchronous optical sampling. Applied spectroscopy, 41(1), 2-4.

[134] Kafka, J. D., Pieterse, J. W., & Watts, M. L. (1992). Two-color subpicosecond optical sampling technique. Optics letters, 17(18), 1286-1288.

[135] Yasui, T., Kawamoto, K., Hsieh, Y. D., Sakaguchi, Y., Jewariya, M., Inaba, H., ... & Araki, T. (2012). Enhancement of spectral resolution and accuracy in asynchronous-optical-sampling terahertz time-domain spectroscopy for low-pressure gas-phase analysis. Optics express, 20(14), 15071-15078.

[136] Bartels, A., Cerna, R., Kistner, C., Thoma, A., Hudert, F., Janke, C., & Dekorsy, T. (2007). Ultrafast time-domain spectroscopy based on high-speed asynchronous optical sampling. Review of Scientific Instruments, 78(3), 035107.

[137] Klatt, G., Gebs, R., Janke, C., Dekorsy, T., & Bartels, A. (2009). Rapid-scanning terahertz precision spectrometer with more than 6 THz spectral coverage. Optics Express, 17(25), 22847-22854.

[138] Yasui, T., Kawamoto, K., Hsieh, Y. D., Sakaguchi, Y., Jewariya, M., Inaba, H., ... & Araki, T. (2012). Enhancement of spectral resolution and accuracy in asynchronous-optical-sampling terahertz time-domain spectroscopy for low-pressure gas-phase analysis. Optics express, 20(14), 15071-15078.

[139] Cuffe, J., Ristow, O., Chávez, E., Shchepetov, A., Chapuis, P. O., Alzina, F., ... & Torres, C. S. (2013). Lifetimes of confined acoustic phonons in ultrathin silicon membranes. Physical review letters, 110(9), 095503.

[140] Dilhaire, S., Pernot, G., Calbris, G., Rampnoux, J. M., & Grauby, S. (2011). Heterodyne picosecond thermoreflectance applied to nanoscale thermal metrology. Journal of Applied Physics, 110(11), 114314.

[141] d'Acremont, Q., Pernot, G., Rampnoux, J. M., Furlan, A., Lacroix, D., Ludwig, A., & Dilhaire, S. (2017). High-throughput heterodyne thermoreflectance: Application to thermal conductivity measurements of a Fe–Si–Ge thin film alloy library. Review of Scientific Instruments, 88(7), 074902.

[142] Pernot, G., Stoffel, M., Savic, I., Pezzoli, F., Chen, P., Savelli, G., ... & Mingo, N. (2010). Precise control of thermal conductivity at the nanoscale through individual phonon-scattering barriers. Nature materials, 9(6), 491-495.

[143] Pradère, C., Clerjaud, L., Batsale, J. C., & Dilhaire, S. (2011). High speed heterodyne infrared thermography applied to thermal diffusivity identification. Review of scientific instruments, 82(5), 054901.

[144] Salazar, A. (2003). On thermal diffusivity. European journal of physics, 24(4), 351.

[145] Parker, W. J., Jenkins, R. J., Butler, C. P., & Abbott, G. L. (1961). Flash method of determining thermal diffusivity, heat capacity, and thermal conductivity. Journal of applied physics, 32(9), 1679-1684.

[146] King, J. (1988). Materials handbook for hybrid microelectronics. Artech House Inc, 685 Canton Street, Norwood, Massachusetts 02062, USA, 1988.

[147] Chen, J. K., Tzou, D. Y., & Beraun, J. E. (2006). A semiclassical two-temperature model for ultrafast laser heating. International journal of heat and mass transfer, 49(1-2), 307-316.

[148] Carpene, E. (2006). Ultrafast laser irradiation of metals: Beyond the two-temperature model. Physical Review B, 74(2), 024301.

[149] Wilson, R. B., Feser, J. P., Hohensee, G. T., & Cahill, D. G. (2013). Two-channel model for nonequilibrium thermal transport in pump-probe experiments. Physical Review B, 88(14), 144305.

[150] Jang, H., Kimling, J., & Cahill, D. G. (2020). Nonequilibrium heat transport in Pt and Ru probed by an ultrathin Co thermometer. Physical Review B, 101(6), 064304.

[151] Kimling, J., & Cahill, D. G. (2017). Spin diffusion induced by pulsed-laser heating and the role of spin heat accumulation. Physical Review B, 95(1), 014402.

[152] Sobolev, S. L. (2016). Nonlocal two-temperature model: Application to heat transport in metals irradiated by ultrashort laser pulses. International Journal of Heat and Mass Transfer, 94, 138-144.

[153] Chen, J. K., Latham, W. P., & Beraun, J. E. (2005). The role of electron–phonon coupling in ultrafast laser heating. Journal of laser applications, 17(1), 63-68.

[154] Block, A., Liebel, M., Yu, R., Spector, M., Sivan, Y., De Abajo, F. G., & van Hulst, N. F. (2019). Tracking ultrafast hot-electron diffusion in space and time by ultrafast thermomodulation microscopy. Science advances, 5(5), eaav8965.

[155] Bonn, M., Denzler, D. N., Funk, S., Wolf, M., Wellershoff, S. S., & Hohlfeld, J. (2000). Ultrafast electron dynamics at metal surfaces: Competition between electron-phonon coupling and hot-electron transport. Physical Review B, 61(2), 1101.

[156] Jackson, J. D. (1999). Classical electrodynamics.

[157] Gabriel, M. M., Kirschbrown, J. R., Christesen, J. D., Pinion, C. W., Zigler, D. F., Grumstrup, E. M., ... & Papanikolas, J. M. (2013). Direct imaging of free carrier and trap carrier motion in silicon nanowires by spatially-separated femtosecond pump–probe microscopy. Nano letters, 13(3), 1336-1340.

[158] Zheng, F., Tao, J., & Rappe, A. M. (2017). Frequency-dependent dielectric function of semiconductors with application to physisorption. Physical Review B, 95(3), 035203.

[159] Cohen, M. L., & Louie, S. G. (2016). Fundamentals of condensed matter physics. Cambridge University Press.

[160] Shin, T., Teitelbaum, S. W., Wolfson, J., Kandyla, M., & Nelson, K. A. (2015). Extended two-temperature model for ultrafast thermal response of band gap materials upon impulsive optical excitation. The Journal of chemical physics, 143(19), 194705.

[161] Antonelli, G. A., Perrin, B., Daly, B. C., & Cahill, D. G. (2006). Characterization of mechanical and thermal properties using ultrafast optical metrology. MRS bulletin, 31(8), 607-613.

[162] Zheng, X., Cahill, D. G., Weaver, R., & Zhao, J. C. (2008). Micron-scale measurements of the coefficient of thermal expansion by time-domain probe beam deflection. Journal of Applied Physics, 104(7), 073509.

[163] Ihee, H., Lorenc, M., Kim, T. K., Kong, Q. Y., Cammarata, M., Lee, J. H., ... & Wulff, M. (2005). Ultrafast x-ray diffraction of transient molecular structures in solution. Science, 309(5738), 1223-1227.

[164] Pudell, J., Maznev, A. A., Herzog, M., Kronseder, M., Back, C. H., Malinowski, G., ... & Bargheer, M. (2018). Layer specific observation of slow thermal equilibration in ultrathin metallic nanostructures by femtosecond X-ray diffraction. Nature communications, 9(1), 1-7.

[165] Sotrop, J., Kersch, A., Domke, M., Heise, G., & Huber, H. P. (2013). Numerical simulation of ultrafast expansion as the driving mechanism for confined laser ablation with ultra-short laser pulses. Applied Physics A, 113(2), 397-411.

[166] Yuan, Y. X. (1994). Trust region algorithms for nonlinear equations. Hong Kong Baptist University, Department of Mathematics.

[167] Grumstrup, E. M., Gabriel, M. M., Cating, E. M., Pinion, C. W., Christesen, J. D., Kirschbrown, J. R., ... & Papanikolas, J. M. (2014). Ultrafast carrier dynamics in individual silicon nanowires: characterization of diameter-dependent carrier lifetime and surface recombination with pump–probe microscopy. The Journal of Physical Chemistry C, 118(16), 8634-8640.

[168] Vietmeyer, F., Frantsuzov, P. A., Janko, B., & Kuno, M. (2011). Carrier recombination dynamics in individual CdSe nanowires. Physical Review B, 83(11), 115319.

[169] Zhang, W., Lehmann, S., Mergenthaler, K., Wallentin, J., Borgström, M. T., Pistol, M. E., & Yartsev, A. (2015). Carrier recombination dynamics in sulfur-doped InP nanowires. Nano letters, 15(11), 7238-7244.

[170] Zhang, W., Yang, F., Messing, M. E., Mergenthaler, K., Pistol, M. E., Deppert, K., ... & Yartsev, A. (2016). Recombination dynamics in aerotaxy-grown Zn-doped GaAs nanowires. Nanotechnology, 27(45), 455704.

[171] Guichard, A. R., Kekatpure, R. D., Brongersma, M. L., & Kamins, T. I. (2008). Temperature-dependent Auger recombination dynamics in luminescent silicon nanowires. Physical Review B, 78(23), 235422.

[172] Zhang, W., Zeng, X., Su, X., Zou, X., Mante, P. A., Borgstrom, M. T., & Yartsev, A. (2017). Carrier recombination processes in gallium indium phosphide nanowires. Nano letters, 17(7), 4248-4254.

[173] Demichel, O., Calvo, V., Pauc, N., Besson, A., Noé, P., Oehler, F., ... & Magnea, N. (2009). Recombination dynamics of spatially confined electron−hole system in luminescent gold catalyzed silicon nanowires. Nano letters, 9(7), 2575-2578.

[174] Cardin, V., Dion-Bertrand, L. I., Grégoire, P., Nguyen, H. P. T., Sakowicz, M., Mi, Z., ... & Leonelli, R. (2013). Recombination dynamics in InGaN/GaN nanowire heterostructures on Si (111). Nanotechnology, 24(4), 045702.

[175] Crankshaw, S., Reitzenstein, S., Chuang, L. C., Moewe, M., Münch, S., Böckler, C., ... & Chang-Hasnain, C. (2008). Recombination dynamics in wurtzite InP nanowires. Physical Review B, 77(23), 235409.

[176] Gabriel, M. M., Grumstrup, E. M., Kirschbrown, J. R., Pinion, C. W., Christesen, J. D., Zigler, D. F., ... & Papanikolas, J. M. (2014). Imaging charge separation and carrier recombination in nanowire pin junctions using ultrafast microscopy. Nano letters, 14(6), 3079-3087.

[177] Grumstrup, E. M., Gabriel, M. M., Pinion, C. W., Parker, J. K., Cahoon, J. F., & Papanikolas, J. M. (2014). Reversible strain-induced electron–hole recombination in silicon nanowires observed with femtosecond pump–probe microscopy. Nano letters, 14(11), 6287-6292.

[178] Reparaz, J. S., Güell, F., Wagner, M. R., Hoffmann, A., Cornet, A., & Morante, J. R. (2010). Size-dependent recombination dynamics in ZnO nanowires. Applied Physics Letters, 96(5), 053105.

[179] Prasankumar, R. P., Upadhya, P. C., & Taylor, A. J. (2009). Ultrafast carrier dynamics in semiconductor nanowires. physica status solidi (b), 246(9), 1973-1995.

[180] Grumstrup, E. M., Cating, E. M., Gabriel, M. M., Pinion, C. W., Christesen, J. D., Kirschbrown, J. R., ... & Papanikolas, J. M. (2014). Ultrafast carrier dynamics of silicon nanowire ensembles: the impact of geometrical heterogeneity on charge carrier lifetime. The Journal of Physical Chemistry C, 118(16), 8626-8633.

[181] Mohite, A. D., Perea, D. E., Singh, S., Dayeh, S. A., Campbell, I. H., Picraux, S. T., & Htoon, H. (2012). Highly efficient charge separation and collection across in situ doped axial VLS-grown Si nanowire p–n junctions. Nano letters, 12(4), 1965-1971.

[182] Allen, J. E., Hemesath, E. R., Perea, D. E., Lensch-Falk, J. L., Li, Z. Y., Yin, F., ... & Lauhon, L. J. (2008). High-resolution detection of Au catalyst atoms in Si nanowires. Nature nanotechnology, 3(3), 168-173.

[183] Fitzgerald, D. J., & Grove, A. S. (1968). Surface recombination in semiconductors. Surface Science, 9(2), 347-369.

[184] Lannoo, M. (1987). Electron states and recombination velocities at semiconductor surfaces and interfaces. Revue de Physique Appliquée, 22(8), 789-795.

[185] Aspnes, D. E. (1983). Recombination at semiconductor surfaces and interfaces. Surface Science, 132(1-3), 406-421.

[186] Nowak, D., Morrison, W., Wickramasinghe, H. K., Jahng, J., Potma, E., Wan, L., ... & Park, S. (2016). Nanoscale chemical imaging by photoinduced force microscopy. Science advances, 2(3), e1501571.

[187] Jahng, J., Brocious, J., Fishman, D. A., Huang, F., Li, X., Tamma, V. A., ... & Potma, E. O. (2014). Gradient and scattering forces in photoinduced force microscopy. Physical Review B, 90(15), 155417.

[188] Tumkur, T. U., Yang, X., Cerjan, B., Halas, N. J., Nordlander, P., & Thomann, I. (2016). Photoinduced force mapping of plasmonic nanostructures. Nano letters, 16(12), 7942-7949.

[189] Ambrosio, A. Selective Excitation and Imaging of Ultraslow Phonon Polaritons in Thin Hexagonal Boron Nitride Crystals. 2018, 9.

[190] Zeng, J.; Darvishzadeh-Varcheie, M.; Albooyeh, M.; Rajaei, M.; Kamandi, M.; Veysi, M.; Potma, E. O.; Capolino, F.; Wickramasinghe, H. K. Exclusive Magnetic Excitation Enabled by Structured Light Illumination in a Nanoscale Mie Resonator. ACS Nano 2018, 10.

[191] Lee, S.; Hippalgaonkar, K.; Yang, F.; Hong, J.; Ko, C.; Suh, J.; Liu, K.; Wang, K.; Urban, J. J.; Zhang, X.; Dames, C.; Hartnoll, S. A.; Delaire, O.; Wu, J. Anomalously Low Electronic Thermal Conductivity in Metallic Vanadium Dioxide. 2017, 5.

[192] Giustino, F. Electron-Phonon Interactions from First Principles. Rev. Mod. Phys. 2017, 89 (1), 015003.

[193] Liao, B.; Qiu, B.; Zhou, J.; Huberman, S.; Esfarjani, K.; Chen, G. Significant Reduction of Lattice Thermal Conductivity by the Electron-Phonon Interaction in Silicon with High Carrier Concentrations: A First-Principles Study. PHYSICAL REVIEW LETTERS 2015, 6.

[194] Zheng, Q.; Mei, A.; Tuteja, M.; Sangiovanni, D.; Hultman, L.; Petrov, I.; Greene, J.; Cahill, D. Phonon and Electron Contributions to the Thermal Conductivity of V N x Epitaxial Layers. Physical Review Materials 2017, 1.

[195] Yang, L.; Tao, Y.; Liu, J.; Liu, C.; Zhang, Q.; Akter, M.; Zhao, Y.; Xu, T. T.; Xu, Y.; Mao, Z.; Chen, Y.; Li, D. Distinct Signatures of Electron–Phonon Coupling Observed in the Lattice Thermal Conductivity of NbSe3 Nanowires. Nano Lett. 2019, 7.

[196] Li, C.; Ravichandran, N. K.; Lindsay, L.; Broido, D. Fermi Surface Nesting and Phonon Frequency Gap Drive Anomalous Thermal Transport. Phys. Rev. Lett. 2018, 121 (17), 175901.

[197] Liu, H.; Yang, C.; Wei, B.; Jin, L.; Alatas, A.; Said, A.; Tongay, S.; Yang, F.; Javey, A.; Hong, J.; Wu, J. Anomalously Suppressed Thermal Conduction by Electron-Phonon Coupling in Charge-Density-Wave Tantalum Disulfide. Advanced Science 2020, 7 (11), 1902071.

[198] Zhang, J.; Levenson-Falk, E. M.; Ramshaw, B. J.; Bonn, D. A.; Liang, R.; Hardy, W. N.; Hartnoll, S. A.; Kapitulnik, A. Anomalous Thermal Diffusivity in Underdoped YBa2Cu3O6+x. PNAS 2017, 114 (21), 5378–5383.

[199] Hayazawa, N., Yano, T., Watanabe, H., Inouye, Y., & Kawata, S. (2003). Detection of an individual single-wall carbon nanotube by tip-enhanced near-field Raman spectroscopy. Chemical Physics Letters, 376(1-2), 174-180.

[200] Bouhelier, A., Renger, J. B., Beversluis, M. R., & Novotny, L. (2003). Plasmon-coupled tip-enhanced near-field optical microscopy. Journal of microscopy, 210(3), 220-224.

[201] Hartschuh, A. (2008). Tip-enhanced near-field optical microscopy. Angewandte Chemie International Edition, 47(43), 8178-8191.